**Aalborg Universitet**

**AALBORG UNIVERSITY**

**Macroscopic Modeling of Transport Phenomena in Direct Methanol Fuel Cells**

Olesen, Anders Christian

*Publication date:*
2013

*Document Version*
Publisher's PDF, also known as Version of record

[Link to publication from Aalborg University](#)

*Citation for published version (APA):*
Olesen, A. C. (2013). *Macroscopic Modeling of Transport Phenomena in Direct Methanol Fuel Cells.* Department of Energy Technology, Aalborg University.

# Macroscopic Modeling of Transport Phenomena in Direct Methanol Fuel Cells

Anders Christian Olesen

Dissertation submitted to the Faculty of Engineering and Science
at Aalborg University in partial fulfillment of the
requirements for the degree of

DOCTOR OF PHILOSOPHY

Aalborg University
Department of Energy Technology
Aalborg, Denmark

Macroscopic Modeling of Transport Phenomena in Direct Methanol Fuel Cells

Anders Christian Olesen ©

Printed in Denmark by UniPrint

**Title:** Macroscopic Modeling of Transport Phenomena in Direct Methanol Fuel Cells

**PhD student:** Anders Christian Olesen

**Supervisor:** Søren Knudsen Kær, Professor

**Co-supervisor:** Torsten Berning, Associate Professor

**Paper 1:** Olesen, Anders Christian; Berning, Torsten; Kær, Søren Knudsen: "The Effect of Inhomogeneous Compression on Water Transport in the Cathode of a Proton Exchange Membrane Fuel Cell". In: Journal of Fuel Cell Science and Technology, Vol. 9, No. 3, 06.2012, p. Article No. 031010

**Paper 2:** Olesen, Anders Christian; Berning, Torsten; Kær, Søren Knudsen: "A Two-Fluid Model for Water and Methanol Transport in a liquid-fed DMFC". Submitted to: The International Journal of Hydrogen Energy, 2013

**Paper 3:** Olesen, Anders Christian; Berning, Torsten; Kær, Søren Knudsen: "On the Diffusion Coefficient of Water in Polymer Electrolyte Membranes". In: E C S Transactions, Vol. 50, No. 2, 2012, p. 979-991.

**Paper 4:** Olesen, Anders Christian; Berning, Torsten; Kær, Søren Knudsen: "Experimental Validation of Methanol Crossover in a Three-dimensional, Two-Fluid Model of a Direct Methanol Fuel Cell". Proceedings of ASME 2012 6th International Conference on Energy Sustainability & 10th Fuel Cell Science, Engineering and Technology Conference: ESFuelCell2012. American Society of Mechanical Engineers, 2012.

# Abstract

An increasing need for energy efficiency and high energy density has sparked a growing interest in direct methanol fuel cells for portable power applications. This type of fuel cell directly generates electricity from a fuel mixture consisting of methanol and water. Although this technology surpasses batteries in important areas, fundamental research is still required to improve durability and performance. Particularly the transport of methanol and water within the cell structure is difficult to study *in-situ*. A demand therefore exist for the fundamental development of mathematical models for studying their transport.

In this PhD dissertation the macroscopic transport phenomena governing direct methanol fuel cell operation are analyzed, discussed and modeled using the two-fluid approach in the computational fluid dynamics framework of CFX 14. The overall objective of this work is to extend the present fundamental understanding of direct methanol fuel cell operation by developing a three-dimensional, two-phase, multi-component, non-isotherm mathematical model including detailed non-ideal thermodynamics, non-equilibrium phase change and non-equilibrium sorption-desorption of methanol and water between fluid phases and the polymer electrolyte membrane. In addition to the performed modeling work, experiments are devised and constructed in order to provide data for a parameter assessment and modeling validation.

Throughout this work different studies have been carried out, addressing various issues of importance for direct methanol fuel cell operation and its modeling. In one study, the effect of inhomogeneous gas diffusion layer compression on cell performance was investigated. This was done to elucidate modeling capabilities with regard to liquid phase flooding of porous media assemblies and its effect on oxygen transport towards the catalyst layer. It was demonstrated that inhomogeneous compression enhances the extent of flooding under the land area, hereby significantly decreasing oxygen transport towards the catalyst layer. Moreover, it was shown that gas diffusion

layer compression also affects liquid water transport in the catalyst layer inhomogeneously.

In another study the effect of membrane hydration on the diffusivity of water in Nafion was examined to discuss the alleged existence of a local maximum. Based on state-of-the-art knowledge on water sorption isotherms and self-diffusivities of water, a new relation for the Fickian diffusivity of water was derived. This diffusivity model did not exhibit a characteristic spike as reported in other studies. Furthermore, it was shown that the existence of a local maximum cannot be validated by merely comparing water flux measurements, unless the exact sorption/desorption kinetics are known even for fairly thick membranes. Similarly, it was shown that permeation experiments falsely can predict a local maximum if care is not put on the formulation of the sorption isotherm used in its conversion.

In a final study, a complete direct methanol fuel cell was partially validated and used for investigating the coupling between the volume porosity of the gas diffusion layer and the capillary pressure boundary condition and its impact on electrochemical performance. In this study, it was shown how a pressure based boundary condition predicts considerable differences in the phase distribution of the GDL when changing its volume porosity, as opposed to a constant liquid volume fraction boundary condition, commonly found in the literature. Moreover, it was shown how this imposed difference in phase distribution causes substantial differences in the predicted limiting current density.

# Dansk resumé

Et stigende behov for øget energi effektivitet og højere energitæthed har igangsat en stigende interesse i metanol brændselsceller til bærbare energi applikationer. Denne type af brændselsceller kan direkte omdanne den kemiske energi af en brændstofs blanding bestående af vand og metanol til elektricitet. Til trods for at denne teknologi overgår batterier på afgørende punkter, er fundamental forskning stadig påkrævet for at forbedre stabiliteten og virkningsgraden. I denne sammenhæng er specielt transporten af metanol og vand svær at undersøge eksperimentelt under drift. Der eksisterer derfor et behov for fundamentale matematiske modeller, der kan simulere deres transport under drift lignende betingelser.

I denne afhandling bliver makroskopiske transport fænomener, som er gældende for metanolbrændselsceller i drift, analyseret, diskuteret og modeleret ved hjælp af to-væske modellen og det kommercielle fluid dynamisk program CFX 14. Det overordnede mål med det arbejde er, at udvide den nuværende fundamentale forståelse af metanolbrændselscellers drift ved, at udvikle en tredimensionel, to-fase, multispecie, ikke-isoterm matematisk model, der inkludere detaljeret ikke-ideel termodynamik, ikke-ligevægts faseskift og ikke-ligevægt sorption/desorption af metanol og vand i mellem væskefaserne og den polymere elektrolyt membran. Ud over dette er eksperimenter blevet udviklet og foretaget for at skaffe data til en parametervurdering samt modelvalidering.

Igennem dette arbejde er forskellige studier blevet foretaget med henblik på at behandle problemstillinger af interesse for metanolbrændselsceller og deres modellering. I et studie blev effekten af inhomogen gas-diffusions-lag-komprimering på virkningsgraden undersøgt. Dette blev gjort for at belyse den udviklede models styrke i beskrivelsen af mætningen og oversvømmelsen af porøse medier og effekten af dette på ilt transporten frem til det katalytiske lag. Igennem studiet blev det påvist, at inhomogen komprimering forstærker graden af oversvømmelse under landområder, hvorved graden af

ilttransport betragteligt falder i det katalytiske lag. Dertil blev det påvist at gas-diffusions-lags-komprimering ligeledes påvirker transporten af vand i det katalytiske lag.

I et andet studie blev effekten af diffusionen af vand i Nafion som funktion a vandindholdet undersøgt for at diskutere den angivelige eksistens af et lokalt maksimum i dens diffusivitet. Baseret på den nyeste viden inden for vand absorptions isotermer og selv-diffusiviteten af vand i Nafion, blev et nyt udtryk for diffusiviteten af vand i Nafion udledt. I modsætning til tidligere viste dette diffusivitetsudtryk ingen tegn på en karakteristisk spids. Foruden dette, blev det vist at eksistensen af et lokalt maksimum ikke kan valideres baseret på målinger af vand fluxen igennem en Nafion membran, med mindre man nøjagtig kender absorptionskarakteristikken for det anvendte materiale. Ligeledes blev det vist, at målinger af vandfluxen igennem en Nafion membran på et falsk grundlag kan forudse et lokalt maksimum i diffusiviteten af vand, hvis absorptionsisotermet der benyttes er forkert.

I det sidste studie blev en komplet metanolbrændselscelle delvist valideret samt brugt til at undersøge effekten af koblingen mellem volumen porøsiteten af gas-diffusions-laget og grænsebetingelsen for kapilarkrafterne ved overgangen mellem gas-diffusions-laget og kanalen på virkningsgraden af cellen. I dette studie blev det vist, hvorledes at en trykbaseret grænsebetingelse forudsiger signifikante forskelle i fasedistribueringen i gas-diffusionslaget når volumen porøsiteten bliver ændret. Dette er i modsætning til den gængse grænsebetingelse baseret på en konstant fase-volumen-fraktion. Ydermere blev det vist at denne forskel i fasedistribueringen forårsagede tilsvarende store forskelle i den forudsagte strømtæthed.

# Acknowledgment

# Nomenclature

**Latin Symbols**

| | | |
|---|---|---|
| Ca | Capillary number | - |
| CA | Complete capillary number | - |
| $c$ | Concentration | mol m$^{-3}$ |
| $D$ | Diffusion coefficient | m$^2$/s |
| Eo | Eötvös number | - |
| $n_d$ | Electro-osmotic drag coefficient | S/m |
| $H$ | Enthalpy | J |
| $EW$ | Equivalent weight of Nafion | kg/mole |
| $f$ | Fraction | |
| $\dot{m}$ | Mass rate | kg/s |
| Fr | Froude number | - |
| g | Gravity | m/s$^2$ |
| $\overline{\mathbf{K}}$ | Hydraulic permeability matrix | m$^2$ |
| $a$ | Interfacial area density | m$^2$/m$^3$ |
| Kn | Knudsen number | |
| $J$ | Leverett J function | |
| $J$ | Mass flux | kg/m$^2$ |

| $Y$ | Mass fraction | - |
|---|---|---|
| $X$ | Mole fraction | - |
| $n$ | Number of moles | mole |
| OR | Open ratio | - |
| Pe | Peclet number | - |
| $s$ | Phase volume fraction / Saturation | |
| $p$ | Pressure | Pa |
| Re | Reynolds number | - |
| $S$ | Source term | - |
| $a$ | Species activity | - |
| $k$ | Kinetic sorption/desorption coefficient | m s$^{-1}$ |
| $N$ | Species flux | mol/s |
| $A$ | Specific surface area of Nafion | - |
| $U$ | Superficial velocity | m s$^{-1}$ |
| $T$ | Temperature | K |
| $t$ | Time | s |
| M | Viscosity number | - |
| We | Weber number | - |

**Abbreviations**

| CCS | Carbon capture and storage |
|---|---|
| CL | Catalyst layer |
| CFD | Computational fluid dynamics |
| EOD | Electro-osmotic drag |

| | | |
|---|---|---|
| AR4 | Fourth Assessment Report | |
| GDL | Gas diffusion layer | |
| GHG | Green house gasses | |
| IPCC | Intergovernmental Panel on Climate Change | |
| ICE | Internal combustion engine | |
| IEA | International Energy Agency | |
| MPL | Microporous layer | |
| MOR | Methanol oxydation reaction | |
| NPS | New Policy Scenario | |
| OCV | Open circuit voltage | |
| ORR | Oxygen reduction reaction | |
| PDE | Partial differential equations | |
| PEMFC | Polymer electrolyte membrane fuel cells | |
| PTFE | Polytetrafluoroethylene | |
| TPB | Triple point boundary | |
| DMFC | Direct Methanol Fuel Cell | |

**Greek Symbols**

| | | |
|---|---|---|
| $\psi$ | Any scalar, vector or tensor valued property function | |
| $\mu$ | Chemical potential | mol m$^{-3}$ |
| $\theta$ | Contact angle | rad |
| $\phi$ | Electrical potential | V |
| $K$ | Hydraulic permeability | m$^2$ |
| $\sigma$ | Ion conductivity | S/m |

x

| | | |
|---|---|---|
| $\lambda$ | Species content in polymer electrolyte membranes | - |
| $\rho$ | Density | kg m$^{-3}$ |
| $\sigma$ | Surface tension | N m$^{-1}$ |
| $\mu$ | Viscosity | Pa s |
| $\varepsilon$ | Volume porosity | - |

**Subscripts**

| | |
|---|---|
| $c$ | Capillary |
| $g$ | Gas |
| $Hi$ | Hydrophilic |
| $l$ | Liquid |

# List of Figures

# List of Tables

# Contents

# Chapter 1

# Introduction

*In order to establish the research framework for the PhD dissertation the following topics are covered in the introduction: project motivation, background, direct methanol fuel cells (DMFC), project objective, methodology and dissertation outline. While the section on project motivation gives an explicit reason for carrying out this work, the background section outlines more generalized causes for investigating methanol based fuel cells. In the section on DMFC, its working principles and general modeling are described, followed by a detailed literature review on mathematical modeling of macroscopic phenomena governing water and methanol transport. Based on this literature review, project objectives are defined. Subsequently, the methodology used for achieving the project objectives is outlined and finally, the introduction is completed by a dissertation outline.*

## 1.1   Project Motivation

During the last decade DMFC for portable power applications have been subject to intensive research both on component and system level. To evolve DMFC and bring them to a commercial level, not only a cost reduction is necessary, a better understanding of fundamental behavior is needed to improve durability and performance. Since it is difficult to carry out *in-situ* measurements on fuel cells during operation, research in recent years has focused on developing mathematical representations of the macroscopic transport phenomena and electrochemistry governing their operation. A popular approach for mathematically modeling DMFC is computational fluid dynamics (CFD). The development of explicit CFD models for DMFC can shed light on the impact of key parameters on performance. Particularly

the transport of water and methanol is of great importance, as it is directly related to performance. However, modeling of these species is a complicated matter as they are subject to non-ideal thermodynamics, non-equilibrium conditions and two-phase flow. Recent advances in experimental techniques have given rise to new detailed knowledge on individual physio-chemical and electrochemical properties and mechanisms. Introduction of this state-of-the-art knowledge into current CFD models can improve predictability and make CFD a better tool for industrial optimization.

## 1.2   Background

The growing interest in fuel cells and in particular DMFC can be traced back to numerous motives. Of these, two should be emphasized: climate change mitigation, and the thereby following need for higher energy efficiency, and the evolving technological requirement of portable power applications for high energy density sources.

### 1.2.1   Climate Change Mitigation and Energy Efficiency

In order to assess the state of scientific, technical and social-economic knowledge on climate change, the (IPCC) was founded by the United Nations Environmental Program (UNEP) and the World Meteorological Organization (WMO) in 1988. According to the IPCC climate change is defined as:

> "... a change in the state of the climate that can be identified (e.g. using statistical test) by change in the mean and/or the variability of its properties, and that persists for an extended period, typically decades or longer. It refers to any change in climate over time, whether due to natural variability or as result of human activity." - IPCC

In the IPCC's (AR4) from 2007 the physical science basis of climate change was presented. It included progress in our understanding of human and natural drivers of climate change, observed climate change, climate processes and attribution, and estimates of projected future climate change. In summary the AR4 reported that the global atmospheric concentration of carbon dioxide, methane and nitrous oxide had increased significantly since the pre-industrial age as a result of human activity. Moreover, it was found with high confidence that this increase in greenhouse gas (GHG) emissions were the cause of global warming. The likelihood of an anthropogenic imposed

climate change was confirmed as being quantitatively consistent with the expected response to external forcing. Direct observation of a global climate change included an increase in the total global surface temperature of 0.76°C from 1850 to 2006, where the last twelve years from 1995 to 2006 ranked among the hottest, an increase in global average sea level by 1.8 mm over 1961 to 2003, and an increased widespread melting of polar ice. Furthermore, it was concluded that continued GHG emissions at or above current rates will cause increased global warming.[39]

With this bleak outlook on climate change the question arises: What can potentially be done about this? It is here where the concept of climate change mitigation emerges. According to the United Nations Framework Convention on Climate Change it can be defined as the human intervention to reduce the sources or enhance the sinks of greenhouse gases. In other words, climate change mitigation means the human action of reducing the use of fossil fuels by substituting them by alternative energy sources, increasing energy efficiency, enhancing foresting or introducing carbon capture and storage (CCS) technologies. Meanwhile, the challenge in climate change mitigation lies in establishing a global consensus on a specific set of targets for GHG emissions and the technological requirements to meet them. The impact of these targets are therefore investigated using climate change mitigation scenarios. In these an assessment is made about the effect of political action, either current or potential future agreements, the direction of global economic activity, demography, energy prices and energy technologies. This information is then processed and fed into a global climate change model that is used for casting predictions of the resulting weather patterns and temperature rise. These predictions are accompanied by probabilities that these projections are reached. As a tool these scenarios are extremely helpful when they are used for comparison. By setting up several scenarios and comparing their outcome, recommendation can be given to policy makers on legislation and where to invest in research and development for the best suitable outcome.

In the recent World Energy Outlook 2012 by the (IEA), the importance of increasing energy efficiency was underlined as a means of effectively decreasing the extent of climate change. This was done by comparing two climate change scenarios; the (NPS) which provides a benchmark to assess the potential achievements of recent developments in energy and climate policy, and the 450 Scenario (450S) which demonstrates a plausible path to achieving a climate change target of an average temperature increase of 2°K in the long term, with a 50 % probability of succeeding. In contrast,

the NPS would lead to a temperature rise of 3.5°K with a 50 % probability of occurring. In the IEAs comparison it was shown that a large share of the emission reductions needed to lower the temperature rise from 3.5 to 2°K has to originate from enhancing energy efficiency, including electricity savings, end-use efficiency and power plant efficiency. This has to be seen as in addition to increasing the extent of renewable energy sources and introducing CCS on a large scale. Moreover, it should be pointed out that the required increase in energy efficiency is concentrated around appliances, buildings and the transport sector.

In light of these requirements the possible technologies for achieving this efficiency increase should be assessed. Here one has to distinguish between stationary, portable and transport power application, since they set different requirements for weight, volume and response time. As shown in table 1.1, when only comparing the electrical efficiency for stationary electricity production a significant improvement can be obtained by switching from internal combustion engines (ICE) or Sterling engines to fuel cells. On the other hand doing so comes with a sacrifice in thermal efficiency. For transportation the electrical efficiency gain of switching to fuel cell systems is more modest compared with hybrid solutions based on ICE and batteries. This is one of the reasons why it is often argued as being more feasible in the short- and mid-term to invest in hybrid solutions rather than fuel cells [17, 95, 79]. For portable power applications the highest possible energy efficiency can be obtained from batteries. However, in contrast to micro ICE and fuel cells they need to be charged from an external source. This means that the overall electrical efficiency from fuel to discharge is significantly lower. Accounting for this pushes the actual efficiency closer to that of fuel cells. Hence, according to efficiencies it could seem that fuel cells do not have a competitive gain on batteries for portable power application, however there are other properties that make them more competing, and this will be discussed in the following section.

### 1.2.2   Portable Power Applications and High Energy Density

The electricity consumption of portable electronics such as laptops and smart phones has significantly increased in recent years due to the technological advances within electronics and an increased demand for high-bandwidth and advanced micro processing applications. Consequently, run-time of these devices is deemed to decrease if Lithium-ion batteries are used, as their low energy density else would make them too bulky.[22] However, not only portable electronics require high energy density sources, similar require-

| Application | Technology | Efficiency | | | Ref. |
| --- | --- | --- | --- | --- | --- |
| | | Electrical | Thermal | Total | |
| Stationary | ICE | 20-30 % | 50-70 % | 80-100 % | [18][4] |
| | Stirling engines | 10-30 % | 40-80 % | 70-90 % | [18][4] |
| | Fuel cells | 35-60 % | 35-60 % | 80-100 % | [18][89] |
| Transport | ICE | 10-22 % | | | [17] |
| | Hybrid ICE | 20-30 % | | | [17] |
| | Hybrid fuel cell | 20-36 % | | | [17][95] |
| Portable | Micro ICE | 8-15 % | | | |
| | Fuel cell | 25-50 % | | | |
| | Batteries | 82-93 % | | | [93] |

**Table 1.1:** Efficiencies of different technologies for energy supply for various applications

ments are found for extending run-time of materials handling equipment indoor, military applications, meeting on-board power needs in recreational vehicles, and powering remote electronic equipment, to name a few.[65] As illustrated in the gravimetric Ragone plot depicted in figure 1.1, an obvious alternative to batteries as a portable power source are fuel cells. Although the power density they can supply is much lower, a significant increase in run-time of several hours can be obtained. Moreover, an important advantage of fuel cells is the simplicity of scaling their energy density. For a fixed fuel cell size scaling is simply a matter of sizing the fuel reservoir. The most common fuel cell technologies considered for portable power applications are DMFC and indirect methanol fuel cell based on a high temperature polymer electrolyte membrane [65]. Here the term indirect covers the use of an external micro-reactor that converts methanol into hydrogen. Both of these types offer a high energy density, fast start-up characteristics, and nearly zero recharge time. Whereas a DMFC can be quite compact as it directly oxidizes methanol, a HT PEMFC system needs additional components which increases system size and complexity.

The use of methanol for energy storage and distribution has been discussed for a while. This has even given rise to the notion of the Methanol Economy, as proposed and advocated by Prof. Dr. G.A. Olah. In his essay "Beyond Oil and Gas: The Methanol Economy" [69], he discusses the advantages of methanol at the present moment and in the future. In conclusion, he points out that methanol surpasses hydrogen as the future energy
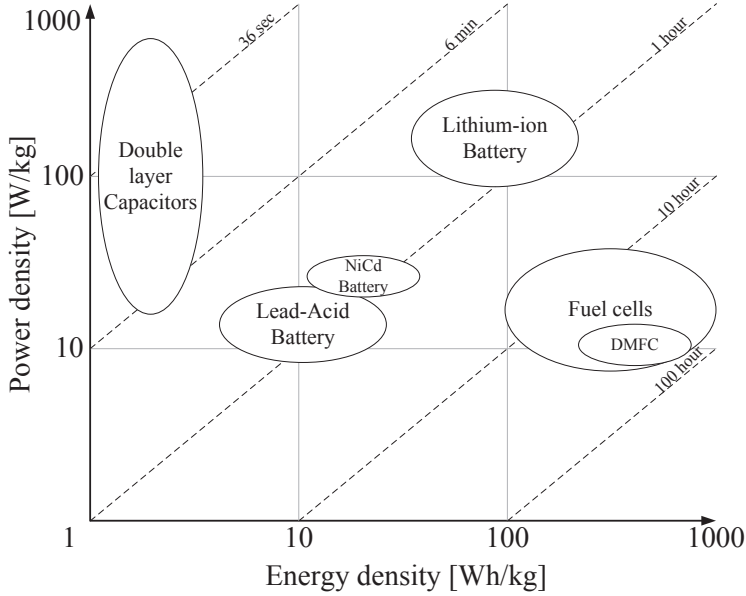
**Figure 1.1:** Gravimetric Ragone plot depicting the relationship between power density and energy density for various power sources

carrier and distributor, mainly since it offers an even higher energy density than liquefied hydrogen, it is much less volatile and in general is subject to the same restrictions as gasoline. Moreover, he points out that methanol already today is available, since it is produced commercially on a large scale from fossil-fuel-based syn-gas and direct oxidation of natural gas according to the following reactions:

$$CO + 2H_2 \rightleftharpoons CH_3OH \tag{1.1}$$

$$\frac{1}{2}O_2 + CH_4 \rightleftharpoons CH_3OH \tag{1.2}$$

However, more interestingly, in the future it could potentially be produced from reductive conversion of atmospheric carbon dioxide or carbon dioxide captured from combustion of biomass or other bio-fuels. This would then create a carbon neutral cycle, hence making methanol a bridge to a renewable energy future.

## 1.3 Direct Methanol Fuel Cells

In the following the discussion will focus on the working principle of a DMFC, its individual components and highlight the importance of water and methanol transport. This is followed by an introduction to DMFC modeling and a literature review on detailed macroscopic modeling of DMFC.
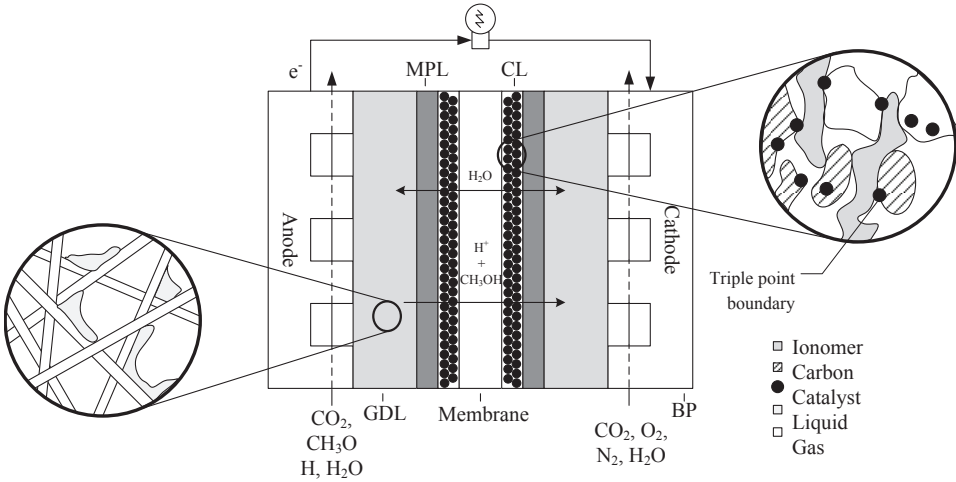


**Figure 1.2:** Schematics of a liquid fed direct methanol fuel cell driven on air

### 1.3.1 Working Principle

A DMFC is essentially an electrochemical device that can convert the internally stored chemical energy of methanol into electricity directly without the requirement of any mechanical moving parts. In its basic configuration it consists of two electrodes, one electrolyte membrane, bipolar plates and an external electrical circuit.

A fuel mixture consisting of a liquid methanol and water is supplied to the anode, where it is reduced by a electro-catalyst to form gaseous carbon dioxide, protons and electrons through the methanol oxidation reaction (MOR). Meanwhile, air is supplied to the cathode, where it is oxidized by an electro-catalyst to form water via the oxygen reduction reaction (ORR). Each half-cell reaction is depicted in equation 1.3 and 1.4, respectively, and the overall electrochemical reaction in equation 1.5:

$$CH_3OH + H_2O \rightleftharpoons CO_2 + 6H^+ + 6e^- \qquad (1.3)$$

$$\frac{3}{2}O_2 + 6H^+ + 6e^- \rightleftharpoons 3H_2O \tag{1.4}$$

$$CH_3OH + \frac{3}{2}O_2 \rightarrow 2H_2O + CO_2 \tag{1.5}$$
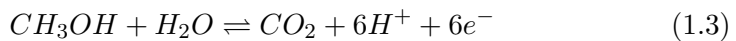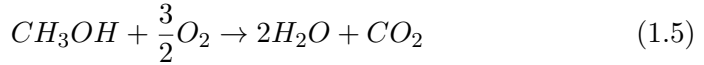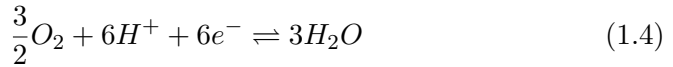
Hence, electrons and ions are produced at the anode, and consumed at the cathode. Each half cell reaction is spatially separated via a polymer electrolyte membrane, which in theory is impermeable to electrons and gasses. While protons then are allowed to pass through, electrons are forced around through an external circuit, constituting the electric current that can be converted into work. The flow of electrons and ions occurs in the direction of decreasing voltage potential, i.e. from anode to cathode.

Thermodynamically, a DMFC has a maximum open circuit voltage (OCV) of 1.21 V at room temperature. However, in practice this value is much lower since methanol can cross over the electrolyte membrane and become catalytically burned and cause a mixed potential at the cathode. The resulting OCV is more likely to be between 0.6 - 0.7 V. In any case, the resulting power output of such a cell is fairly low; hence individual cells need to be put in series, in a so-called stack, to increase cell output. For this purpose bipolar plates are used. They transfer electrons between two adjacent cells; from the anode to the cathode. These polar plates also contain the flow channels that distribute fuel and air over the electrode surface. Although waste heat is produced during operation, there is no need for additional cooling channels, because sufficient cooling is obtained from the liquid stream of the anode due to its high heat capacity.

Since DMFC normally are operated below 100°C, the various species form a two-phase flow. At the anode the liquid phase primarily consists of methanol and water, whereas the gas phase of carbon dioxide, methanol vapor and water vapor. At the cathode the liquid phase only consists of water, while the gas phase contains oxygen, nitrogen, carbon dioxide and water vapor.

For further details on electrochemistry and thermodynamics of fuel cells the reader is referenced to the books by O'Hayre et al. [68] and Barbir [3].

### 1.3.2   Component Description

Offhand, a DMFC from its working principle might seem simple in its make-up. It is often considered one of the primary reasons why fuel cells are seen as a promising technology for mass production. However, the individual

parts serve multiple purposes and hence are selected based on several key properties. In order to get a better grasp of DMFCs make-up let us take a closer look at its individual parts; the electrodes, electrolyte membrane and bipolar plates.

**Electrolyte Membrane**

The electrolyte membranes used in DMFC have different requirements than those conventionally used in PEMFC. In PEMFC the electrolyte membrane is most often made from Nafion, a sulfonated tetrafluoroethylene based fluoropolymer-copolymer. Its backbone structure is similar to (PTFE or teflon), providing it with good mechanical strength. Its ability to transport ions originates from its sulfonic acid functional groups, which provide fixed charge sites. This property, in addition to the presence of free volume, enables ion transport across the polymer membrane. This can happen via two mechanisms: the vehicle mechanism or the Grotthuss mechanism. In the vehicle mechanism water and protons form complexes such as hydronium $(H_3O^+)$. These complexes then function as vehicles that provide protons with a way of transportation between charged sites.[68] Alternatively, protons can be transported via the Grotthuss mechanism, or better known as "proton hopping". Here excess protons hop between water molecules, where they form hydrogen bonds.

Unfortunately, Nafion has one major drawback; it cannot fully prevent methanol from crossing from the anode to cathode, and in consequence being directly oxidized according to equation 1.5. Methanol crossover, in other words, is equivalent to short-circuiting the DMFC. This lowers fuel efficiency and reduces cathode electrode potential. Moreover, it poisons the cathode electro-catalyst. Often these issues are circumvented by increasing membrane thickness, diluting methanol concentration or lower operation temperature. However, these approaches also reduce power output.[66]

As discussed by Neburchilov et al. [66] alternative electrolyte membrane materials exist. These are either based on composite fluorinated or non-fluorinated (hydrocarbon). Especially hydrocarbon membranes are considered the main candidate for the replacement of Nafion; this is due to their lower manufacturing cost and reduced methanol crossover, higher conductivity and stability. It should be noted that a reduced methanol crossover can be obtained by adding inorganic composites, however this does not reduce cost.

**Electrodes**

A state-of-the-art DMFC electrode comprises of a catalyst layer (CL), a micro porous layer (MPL) and macro porous layer [48]. The latter is often referred to as a gas diffusion layer (GDL). As illustrated in figure 1.2, the CL is placed in-between the electrolyte membrane and the MPL. Its main purpose is to create a large active catalytic surface area, where electrochemical reactions can occur. This is achieved by forming a highly porous structure. This not only increases surface area, but enables gas and liquid transport towards reaction sites. However, a catalytic surface area is only useful if it simultaneously is in contact with the electron and proton conducting phases; the so-called triple-point-boundary (TPB). Else, there is no link between reactions sites at the anode and cathode. The electron conducting phase is normally fabricated from carbon and the ion conducting phase from Nafion.

Current electro-catalysts for the ORR are either based on pure Platinum (Pt) or a Pt-alloy. Especially, Pt-alloys have shown improved catalytic activity over pure Pt in recent years. Meanwhile, the challenge not only lies in increasing catalyst activity, but in maintaining durability compared to pure Pt. It has long been a target to reduce the amount of Pt below 0.4 mg/cm$^2$ for the commercialization of DMFC, and PEMFC in general. Merely reducing the Pt particle size below 2-3 nm has shown problematic as it leads to deactivation of the active surface when used in the ORR. [68]

The requirements to the electro-catalyst used in the MOR are different. In the MOR carbon monoxide (CO) is formed as an intermediate. Unfortunately, CO easily adsorbs onto Pt-surfaces, deactivating active sites and decreasing reaction kinetics. It was found that adding Ruthenium (Ru) significantly increases the CO tolerance of a Pt-catalyst by promoting the oxidation of CO into carbon dioxide (CO2). This can be seen from the following detailed reaction mechanism: [49]

$$CH_3OH + Pt \rightarrow PtCH_3OH_{ad} \tag{1.6}$$

$$PtCH_3OH_{ad} \rightleftarrows PtCO_{ad} + 4H^+ + 4e^- \tag{1.7}$$

$$H_2O + Ru \rightleftarrows RuOH_{ad} + H^+ + e^- \tag{1.8}$$

$$PtCO_{ad} + RuOH_{ad} \rightarrow CO_2 + H^+ + e^- + Pt + Ru \tag{1.9}$$
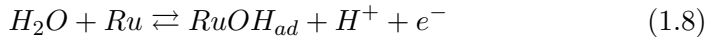
The distribution of reactants and removal of products are done by means of the GDL and MPL. The macro pores of the GDL are typically obtained

by using a graphite carbon fiber substrate coated with polytetrafluoroethylene (PTFE), whereas the micro pores of the MPL are made by binding carbon powder particles using PTFE. The difference in pore size gives rise to significant differences in mechanical strength and transport properties of fluids, heat and electrons. In both cases PTFE is used to obtain a certain fraction of hydrophobicity and pore morphology. The hydrophobic pores effectively improve fluid transport.

At the cathode the hydrophobic pores of the GDL assist in preventing excessive liquid water under the land area, where it has a tendency to condensate due to hydrophilic pores and thermal gradients. Excessive accumulation of liquid water is a severe problem, since it can lead to pore flooding. This, in turn, blocks the transport of air towards the CL and decreases cell performance. The function of the MPL, on the other hand, is quite different and not always well-understood. As has been shown experimentally, adding a MPL significantly improves performance at higher current densities. The extent of this is found to depend on the fraction of PTFE, the type of carbon powder and the hydrophobic pore fraction [74, 98]. Mathematical modeling studies suggest that the MPL in part improves oxygen transport in the GDL by altering the direction of water flow towards the membrane rather then flooding the GDL and in part improves electron transport by increasing conductivity and minimizing contact resistances [72, 102].

However, at the anode the role of GDL and MPL is quite different. Here, the fuel is in liquid state and the product in gaseous state, in direct contrast to the cathode. In this environment the GDL does not remove the liquid phase as it did before, it rather helps it transport towards the CL, while simultaneously removing the gas phase. At the same time, the MPL rather than keeping the GDL less flooded, hinders the liquid phase from being transported towards the CL. This is an advantage, since it limits excessive methanol and water crossover. It should be noted that the exact role of the MPL is still intensively discussed.

**Bipolar Plates and Flow Channels**

Even though the main purpose of bipolar plates is to distribute fuel and air evenly over the entire fuel cell and simultaneously transport electrons between neighboring cells, they are constrained by a number of criteria; high electrical conductivity, corrosion resistant, high chemical compatibility, high thermal conductivity, high mechanical strength etc.[68] Bipolar plates are typically manufactured from graphite or corrosion resistant materials such as stainless steel. Graphite plates meet most of the desired criteria, however

their complexity in being manufactured, cost and low mechanical strength, have made metallic plates more attractive. On the other hand, these introduce new challenges such as corrosion failure due to pinhole formation, electro-catalyst poisoning and passivisation formation.[90]



**(a)** Parallel          **(b)** Serpentine          **(c)** Interdigitated
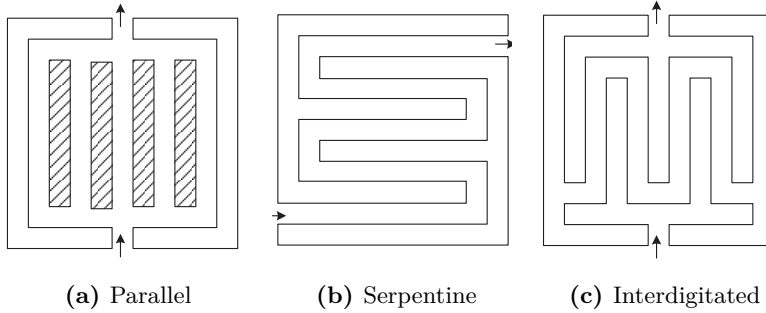
**Figure 1.3:** Major flow channel configurations used for evenly distributing reactants across the electrode surface

In order to achieve the best possible distribution of reactants and best cell performance, different channel shapes, sizes and patterns can be selected from, as depicted in figure 1.3. The archetype patterns are straight channel, serpentine and interdigitated. For DMFC cell performance selecting a proper design is highly critical, since two-phase flow can cause maldistribution of air and fuel and hence starvation. In the cathode some channels might become completely flooded by liquid, whereas gas might block anode channels. A parallel flow channel pattern offers a low pressure loss, but is prone to fuel and air maldistribution. A serpentine flow field typically offers less maldistribution at the expense of a higher pressure loss. Moreover, increased convection under the land area is observed. An often used compromise between maldistribution and low pressure loss is obtained by combining a parallel and serpentine flow field. Finally, the highest pressure loss is obtained with an interdigitated flow field, since the flow is forced underneath the land area through the GDL. This type has shown clear advantages in obtaining a better water management in PEMFC.[68, 3]

For all these patterns the challenge still remains in selecting the appropriate ratio between land and channel area along with channel length. The ratio between land and channel area is often referenced to as the open ratio and is defined as follows:

$$\text{OR} = \frac{w_{chan}}{w_{chan} + w_{land}} \tag{1.10}$$

where $w$ is width. The open ratio affects contact resistance, ohmic losses altered electron transport path-lenght, two-phase flow, mass transport losses in the GDL, methanol crossover and consequently performance, as has been shown experimentally [106].

### 1.3.3 Mathematical Modeling

A mathematical model of a DMFC in its simplest form is a matter of accounting for three dominating voltage loss mechanisms: Activation overpotential, ohmic and mass transport. The activation overpotential, $\eta_{act}$, is the difference between the electric potential field and the ionic potential field, and it is what drives the electrochemical reactions in the CL. The higher the potential difference, the higher the resulting current density. While activation losses are associated with the production and consumption of charges, the ohmic loss, $\eta_{ohmic}$, is associated with the transport of them; ions through the electrolyte and electrons through the carbon phase. What is often referred to as a mass transport losses, $\eta_{conc}$, is in fact an increase in the activation overpotential due to a significant decrease in reactant concentration. Reactant depletion occurs in the CL when the rate of reactant consumption approaches the maximum transport rate towards it. For fuel cells, where two-phase flow occurs, this phenomenon is more pronounced. As schematically shown in figure 1.4 and in the following, the individual potential loss contributions can be superpositioned to give the resulting cell voltage:

$$V = E_{OCV} - \eta_{act} - \eta_{ohmic} - \eta_{conc} \tag{1.11}$$

For DMFC another factor plays a role in the current density and voltage ($i$-V) relation, namely methanol crossover, which leads to a parasitic current density $i_p$. Moreover, methanol crossover causes a mixed potential at the cathode which effectively shifts the $i$-V curve to the left, as depicted in figure 1.4.

Although, a mathematical representation of DMFC can be given by merely accounting for these losses many important phenomena and their interaction are neglected. These include two-phase flow, thermodynamics, thermal gradients, to name a few. As mathematical models move from one towards two or three-dimensional representations more and more of these
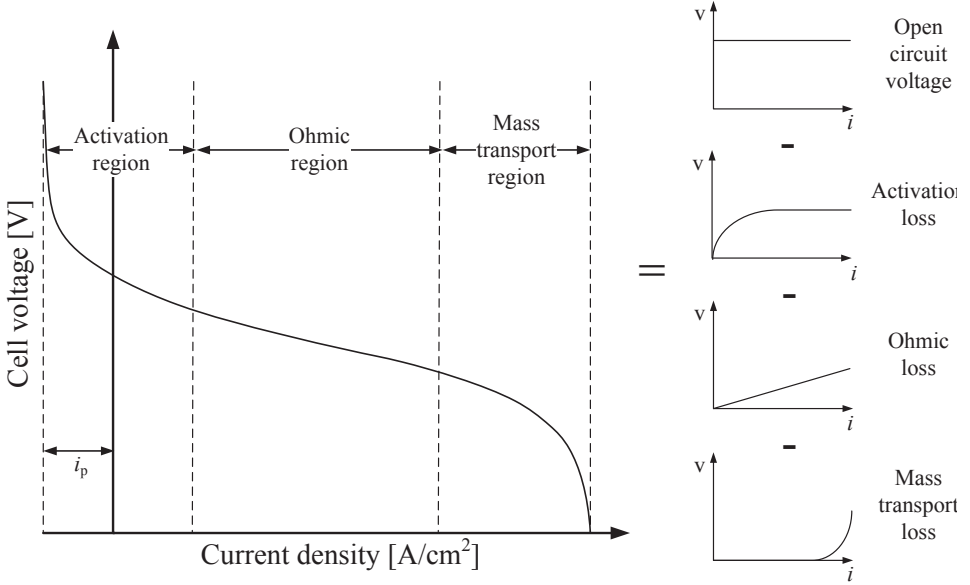
**Figure 1.4:** A schematic representation of DMFC current density and voltage curve including potential loss regions

phenomena can to a greater extent be accounted for. Moreover, as computational power increases likewise does the possibility for more fundamental mechanistic models describing macroscopic phenomena. In continuation hereof it was recommended in a keynote paper by Djilali [20] that research within fuel cells, should be aimed towards solving the following two problems: (1) lack of sufficiently general models for ionic and water transport in polymer membranes, and (2) deficiencies in models for two-phase transport in porous GDL and gas flow channels. In the following a detailed literature review on macroscopic modeling of DMFC and PEMFC is presented with emphasize on exactly these topics. Both types are considered since they only differ in some aspects related to two-phase morphology, electrochemical reactions and thermodynamics of the anode and membrane. Thus, from a modeling point of view, they are similar with respect to porous media structure, cathode catalyst layer and membrane properties. In the initial part of the literature review the focus is put on general model development, whereas the end focuses on more detailed issues of fuel cell modeling.

**Literature Review**

Because PEMFC and DMFC both are governed by numerous multi-physical phenomena, some simplifications are typically implemented. Early studies conducted by Bernardi and Verbrugge [9] and Springer et al. [88] on PEMFC consisted of isothermal, steady-state, one-dimensional numerical models of the electrode-membrane. These studies provided the fundamental framework for analyzing species transport, water addition and removal, cathode flooding and the effect of gas humidification. Attempts to account for more detailed water transport phenomena in PEMFC emerged a decade later. These models took two-phase flow and three-dimensional phenomena into account. Representative progress was seen in the models by Mazunder and Cole [57] and Meng et al. 2005. Their models were developed for predicting macroscopic water transport effects on cell performance. Both accounted for two-phase flow by a multiphase mixture formulation ($M^2$ model) and phase change by assuming equilibrium phase transformation, i.e. that phases are completely saturated. Their studies underlined the enhanced predictability of including two-phase transport. An alternative approach to multiphase modeling of water transport was taken in Berning and Djilali [10]. Two-phase flow was accounted for by the two-fluid model. Essentially, the two-fluid model is computational more demanding than the commonly used model; however it surpasses this model in its predictability of wet-to-dry and dry-to-wet interfaces and is capable of accounting for a hydrophilic pore fraction and irreducible saturation [12]. It does so by solving the governing equations for each phase separately, and hereby explicitly taking interfacial momentum and mass transfer into account. The two-fluid model moreover has the advantage, that it can be used for solving channel flow by using appropriate constitutive relations for interfacial surface area, buoyancy forces, lift and drag forces as well as surface tension forces over a large range of flow morphologies [40].

Meanwhile, only a few DMFC studies have focused on two-phase flow and three-dimensional modeling, since the importance of two-phase flow was addressed much later. Main focus had therefore been on one- or two-dimensional models of transport phenomena, concentration effects, fuel crossover and catalyst modeling as pointed out in the comparative study by Oliveira et al. [70]. In an early attempt Wang and Wang [99] investigated the coupling between two-phase flow, fuel crossover and the resulting mixed potential at the electrodes. Their two-dimensional model was based on the $M^2$ model and took detailed electrochemical reactions into account. Their results underlined the importance of keeping the methanol concentration

below 2 M, in order to avoid excessive methanol crossover and performance loss. In their model capillary pressure in the two-phase model was described using a Leverett type function, which assumes either a hydrophilic or hydrophobic porous medium, but not a combination of these two. Around the same time Divisek et al. [19] published a two-dimensional, two-phase and multi-component model. In their paper they proposed an alternative capillary pressure model, enabling them to account for hydrophilic as well as hydrophobic pores. Moreover, a comprehensive electrochemistry model was implemented. It accounted for multistep reaction mechanisms and coverage for the ORR and MOR. Unfortunately, experimental validation of the model lacked. Later, Ge and Liu [28] developed a three-dimensional, two-phase, multi-component liquid-fed DMFC model. The model included anode and cathode channel, however neglected the presence of MPL. Their study underlined the improved model predictability of switching from a single to a two-phase flow model. Especially the predictability of methanol crossover was improved.

In the paper by Yang and Zhao [108] the importance of accounting for non-equilibrium phase change in DMFC modeling was shown. Moreover, it was concluded that the assumption of equilibrium phase change in the $\text{M}^2$ model overestimates the mass-transport of water and methanol. Later, Xu et al. [105] developed a one-dimensional, isothermal, two-phase model that accounted for dissolved species transport in the electrolyte phase and non-equilibrium sorption/desorption as well as non-equilibrium phase change. Two-phase flow was solved using the two-fluid approach, and accounted for the saturation jump-condition that arises between adjacent porous layers due to capillary pressure. Their model was used for studying the effect of the MPL on performance, among others.

Several detailed membrane transport models based on concentrated-solution theory have been proposed within the last decade for PEMFC by Janssen [41], Weber and Newman [101] and Fimrite et al. [24] and for DMFC by Meyers and Newman [59] and Schultz and Sundmacher [81]. All these models take multi-component transport and component-component interaction into account by a Generalized Maxwell-Stefan model, also known as the Binary Friction Model. Their difference is mainly due to specified driving forces, and the degree of need for experimentally determined properties. As pointed out by Carnes and Djilali [15], the advantage of such a model is that it surpasses empirical models based on dilute-solution theory in their predictability at lower water content as well as higher water contents. Further, Meyers and Newman [59] underlined that component-component

interaction cannot be neglected in DMFC modeling. Meanwhile, most models published within DMFC modeling are based on dilute-solution theory [99, 109, 111, 61, 60, 51, 36, 28]. This is often assumed acceptable since state-of-the-art DMFC run on a methanol concentration only at around 1 M.

In addition to the many modeling attempts, a lot of research has focused on experimentally quantifying individual transport phenomena governing water and methanol and their dependencies. These transport phenomena cover diffusion [62, 116, 118, 119], electro-osmotic drag (EOD) [80, 75, 34, 115] and sorption/desorption kinetics [119, 78, 54, 53, 29]. Likewise a lot of research has been aimed at developing detailed models describing non-ideal thermodynamics of Nafion membranes and conducting validation experiments [27, 59, 85, 35].

More detailed models on two-phase models for fractional wetted porous media, have been proposed in recent years. These models can be split up into two categories; the ones using a type of modified Leverett function to account for fractional wettability [64, 31, 32, 12, 14, 13, 11, 46], and the ones basing their models on information on the pore size distribution using a type of a bundle-of-capillary model [103, 26, 100, 55]. The former models can be distinguished in whether liquid phase transport can occur in both hydrophilic and hydrophobic pores, or only the hydrophobic. For the latter models the main difference lies in how wettability and the pore size distribution are coupled. An introduction to the modified Leverett J function is given in section 2.3.4.

Another important challenge in the modeling of porous media is the steady-state description of the two-phase boundary condition at GDL-channel interface due to its inherent transient nature. Essentially, the movement of gas and liquid through this interface can be reduced to pressure build-up and break-through of droplets at the cathode and bubbles at the anode. Hence, it is rather difficult to formulate a mechanistic steady-state condition. In the literature various approaches have been proposed. The most often used types are: constant liquid volume fraction (i.e. liquid saturation) or a constant capillary pressure. The importance of this interface condition was studied by Liu and Wang [50] using a three-dimensional and two-phase flow model of a single channel DMFC based on the $M^2$ model. It was shown that the extent of saturation condition at the cathode had a large impact on the net transport of water through the membrane and performance. This was likewise shown by Weber [100], not as function of saturation, but capillary pressure. Different boundary conditions have since been proposed;

Miao et al. [60] based it on an average channel liquid volume fraction, Gu-
rau et al. [33] on a balance between surface tension forces and drag forces,
Berning et al. [12] on a Hagen–Poiseuille pressure resistance and Yang et al.
[110] by fixing the CL liquid volume fraction.

Although progress on the development of methanol and water transport
models is evident, improvements are still needed. Recent research has fo-
cused mainly on improving sub-models of the membrane, catalyst layer, gas
diffusion layer and water transport in the channels, but not on the cou-
pling. Moreover, some of the proposed models in the literature need to be
adapted for CFD purposes. Most two-phase models in the literature are
based on the $M^2$ model, which inherently overestimates mass transport by
assuming equilibrium and momentum transfer by not accounting for irre-
ducible saturation and hydrophilic pore fraction. Computational advances
along with modeling theory developments, enables the syntheses of more
fundamental and complete fuel cell models based on the two-fluid approach,
and affords more detailed accounting for water an methanol transport. By
using a commercial CFD tool, as opposed to many models in the literature,
parallel processing can be utilized to simulate complex and large geome-
tries. As such it is feasible to model complete cells, with alternative channel
configurations, and focus on macro-scale property variations and maldistri-
bution phenomena. These models can then be aimed at facilitating higher
predictability and better qualitative understanding of real size DMFC, as
opposed to only two-dimensional or single channel phenomena.

## 1.4  Project Objective

The primary objective of this PhD study is to advance fundamental knowl-
edge on water and methanol transport in DMFC, and thus to extend the
understanding of the phenomena governing DMFC design. In particular,
emphasis of this research project is on developing a three-dimensional, two-
phase, multi-component, non-isothermal DMFC model and its validation.
The applied modeling framework for the description of two-phase phenom-
ena is based on the two-fluid approach. In addition to the before mentioned
tasks, the present study comprises of answering the following series of sci-
entific questions:

1. How can a cathode and anode model be developed so it reflects current
   state-of-the-art knowledge on porous media structures?

2. How can a better treatment of the channel-GDL interface, with respect

   to two-phase flow, be developed?

3. Can a dilute-solution theory model adequately describe species transport in the membrane of a DMFC?

4. How do membrane properties such as sorption/desorption, water diffusivity, methanol diffusivity and ion conductivity depend upon water content?

5. Which material parameters, defining the pore structure, catalyst layer and membrane, affect the following?

   (a) Phase distribution in cathode and anode

   (b) Methanol crossover and distribution

6. How do material properties and flow plates affect cell performance of a single cell DMFC?

Answering the initial four questions will contribute the main improvement to current state-of-the-art models, by expanding the possibilities of which physical phenomena are taken into account. The latter two questions will contribute to an improved understanding of fundamental and practical problems governing DMFC design.

   To ensure validity of the mathematical predictions, experimental verification is required. Experimental validation of a fuel cell model cannot entirely be based on a polarization curve, therefore simple experiments that can confirm model predictions are devised and constructed. Experimental verification is accomplished through collaboration with IRD Fuel Cells A/S, Denmark.

## 1.5   Methodology

The research methodology consists of three parts: mathematical modeling, parameter assessment and experimental validation through performance characteristics. Each part is necessary in order to obtain a functional and state-of-the-art model of a DMFC. A schematic representation of the research methodology is given in figure 1.5. Each part in the methodology is explained in the following sections.
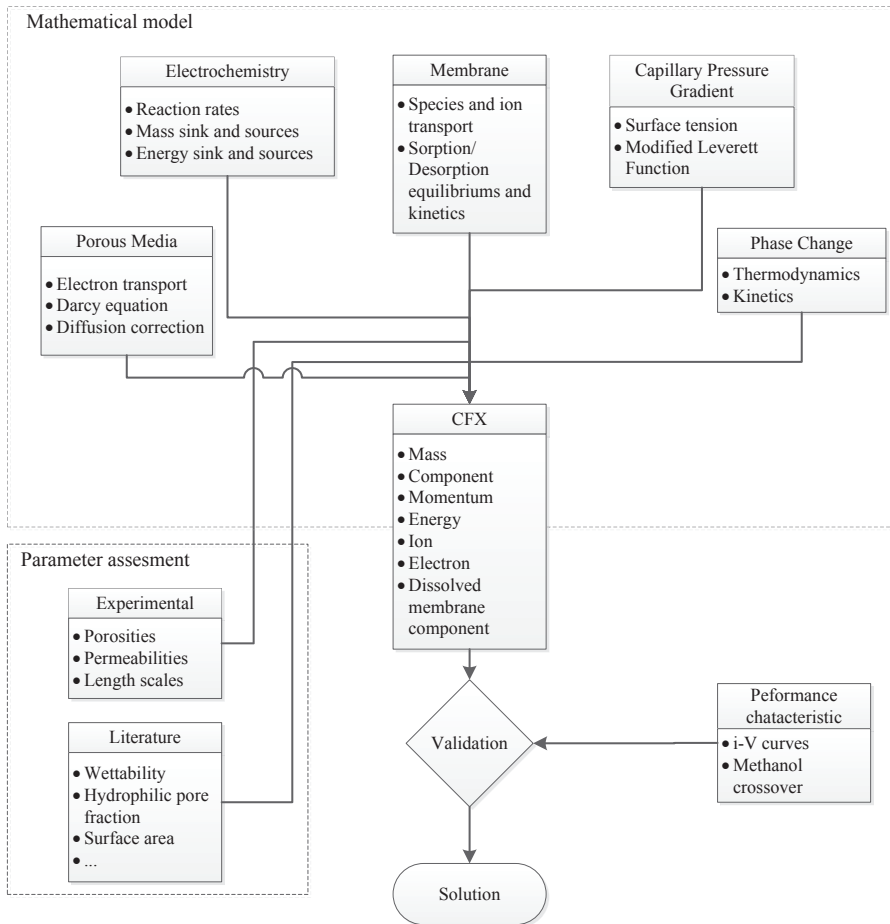
**Figure 1.5:** Schematic representation of research methodology

## 1.5.1   Mathematical Modeling

The mathematical model was developed in the commercial CFD package CFX 14 by ANSYS Inc. This software has the advantage that it is optimized for solving three-dimensional, two-phase, multi-component and non-isothermal flow. Hence, the task of developing a DMFC model is primarily limited to developing sub-models and constitutive relations describing the specific thermodynamics, electrochemistry, membrane transport and two-phase transport in porous media and channels, as shown in figure 1.5. These relations and specific parameters are obtained through an in-depth literature study of physics and chemistry.

A problem with solving the flow field of a complete fuel cell with the intended complexity is the mere size of the computational grid and hence computational time required to solve it. Thus, to reduce computational time the solution domain is limited to a mirrored single channel domain.

### 1.5.2 Parameter Assessment

A challenge in the model development is that not all parameters are accessible through a literature study. Often in simplified zero-, one- or even two-dimensional models this can be circumvented by fitting the model to experimental data. However, this is a time consuming challenge for larger three-dimensional models. Moreover, fitting a large number of parameters simultaneously carries the risk of reaching a local minimum, and not physically correct parameters. Thus, it is important to limit the number of unknown parameters experimentally, in order to increase the reliability of the mathematical model. Hence, the following material properties have been measured directly in experiments as a part of this study:

- Length scales

- Porosities

- Nafion volume fraction in the CL

- Permeabilities

Moreover, the following electrochemical properties are assessed by fitting a simplified zero-dimensional DMFC model to a polarization curve:

- Catalytic surface area

- Exchange current density

- Transfer coefficients

### 1.5.3 Experimental Validation

Another concern in the development of a mathematical model is its validation under specific operational conditions. Typically, experimental validation is achieved by comparing the relationship between cell current and cell voltage. If a difference is observed between experimental measurements and model predictions model parameters can be adapted until a satisfactory agreement is obtained. However, this approach suffers from the risk that one

merely fits a given model to a specific set of data points, rather then mechanistically describing the phenomenon. To minimize this risk a two-folded validation is carried out by simultaneously considering the current-voltage relation and methanol crossover. Moreover, the current-voltage relation is carried out under different operation conditions, i.e. methanol concentration, average cell temperature, methanol concentration and OR.

## 1.6   Dissertation Outline

The main body of this dissertation is split up into six chapters which serve the purpose of theoretically interconnecting the research work depicted in the collection of scientific papers.

**Chapter 1** establishes the research framework of the PhD dissertation by contextualizing the need for DMFC in todays society as well as discussing DMFC operation, its mathematical modeling and progress within the field mathematical modeling of DMFC.

**Chapter 2** gives a general description the two-phase flow phenomena occurring within a DMFC. Moreover, the mathematical framework of the two-fluid model is introduced and discussed in regard to assumptions and closure equations.

**Chapter 3** assesses the macroscopic phenomena governing PEM based on Nafion. Focus is on non-equilibrium sorption-desorption and mathematical models used for describing transport processes in Nafion subject to dilute methanol-water solutions.

**Chapter 4** discusses the solution strategy applied in order to solve mathematical model. In particular, the importance of source term linearization and relaxation is discussed in the context of two-phase flow.

**Chapter 5** presents results from the experimental measurements, a partial validation of developed DMFC model and finally summarizes and discusses the modeling results presented in each publication.

**Chapter 6** concludes the dissertation by assessing research contributions, research objectives and discussing future work.

# Chapter 2

# Fundamentals and Modeling of Two-Phase Flow

*The aim of this chapter is to create an overview of the fundamental two-phase flow phenomena governing DMFC operation and their modeling concepts. The emphasis is particularly on the modeling framework of the two-fluid model.*

*The initial part is covered by dimensionless analysis and a literature study on gas-liquid flow patterns. This is followed by a short overview of the two-phase modeling concepts used for macroscopic modeling of DMFC and their conceptual differences. Hereafter the theoretical basis of the two-fluid method is introduced. Basic assumptions and derivation tools are discussed and the full set of governing equations covering mass, component, momentum and energy transport are depicted. Finally, closure equations are discussed along with a discussion of the validity of the two-fluid model in DMFC modeling.*

## 2.1 Gas-Liquid flow in DMFC

For DMFC an initial distinction can be made between gas-liquid flow in porous media and in channels. Flows in these two regions are subject to forces of different orders of magnitude. This can probably best be demonstrated by comparing the dimensionless groups depicted in table 2.1. In order to relate the individual dimensionless groups to each, a short definition is given. The dimensionless Eötvös number is the ratio between density driven buoyancy and the surface tension acting across an interface between a liquid and a gas or between two immiscible liquids. For channels the variable $D$ represents the hydraulic diameter, whereas for porous media the

**(a)** Nonwetting fluid                    **(b)** Wetting fluid
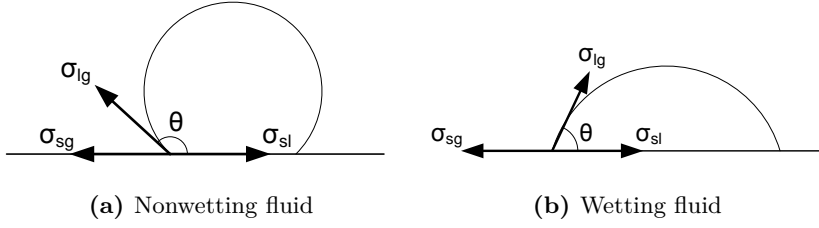
**Figure 2.1:** An overview of the difference between a wetting and non-wetting fluid

characteristic pore diameter. The effect of viscous forces in relation to sur-
face tension forces is either accounted for using the capillary number or the
complete capillary number. The difference lies in whether length scales and
wettability information are accounted for or not. The variable $R$ accounts
for the hydraulic channel radius or the characteristic pore radius, and $\theta$ de-
notes the contact angle between the liquid-solid boundary and the tangent
to the gas-liquid boundary at the three-phase point, as seen in figure 2.1.
The Reynolds number is the ratio between viscous and advective inertial
forces. It is often encountered in fluid dynamical problems, as it identifies
the transition between laminar and turbulent flow. The Froude number rep-
resents the ratio between inertial and gravitational forces. It is often used
for describing free surface flow. The Weber number is the ratio between iner-
tial forces due movement and surface tension forces. The last dimensionless
group is the Peclet number is the ratio between the rate of advection and
rate of diffusion. The length $L$ used in Péclet number can either be the
hydraulic diameter for the channel or the characteristic pore diameter.

In general, for both regions it can be stated that the surface tension force
dominate over buoyancy, viscous and inertial forces, as seen from the Eötvös,
Capillary and Weber numbers, respectively. However, there is a significant
difference in the extent depending on whether the flow occurs in a channel
or a porous medium. To assess the importance of viscous forces it is often
recommended to use the complete capillary number instead of the ordinary
capillary number [21]. From the complete capillary number, it is apparent
that viscous forces play a more important role then the capillary number
indicates. This is especially obvious for the channel. From the Reynolds
number it is further seen that viscous and inertial forces balance each other
in the channel, whereas viscous forces significantly dominate in the GDL
due to small length-scales and large viscosities. When $Re \ll 1$ the motion
of a fluid is often referred to as Stokes flow or creeping flow. Moreover, as
seen from the Froude number, buoyancy forces are considerably larger than

| Name | Symbol | Definition | Order of magnitude | | | |
| --- | --- | --- | --- | --- | --- | --- |
| | | | Channel | | GDL | |
| | | | Liquid | Gas | Liquid | Gas |
| Average superficial velocity | $U$ | $v\varepsilon s$ | $10^{-3}$m/s | 1m/s | $10^{-5}$m/s | $10^{-3}$m/s |
| Bond/Eötvös | Bo/Eo | $\frac{(\rho_l-\rho_g)gD^2}{\sigma}$ | $10^{-3}$ | - | $10^{-5}$ | - |
| Viscosity ratio | M | $\frac{\mu_{nw}}{\mu_w}$ | $10^{-1}$ | 10 | $10^{-1}$ | 10 |
| Capillary | Ca | $\frac{\mu_{nw}|U_{nw}|}{\sigma}$ | $10^{-6}$ | $10^{-4}$ | $10^{-8}$ | $10^{-7}$ |
| Complete capillary | CA | $\frac{4\mu_{nw}|U_{nw}|L}{\sigma\cos\theta R}$ | $10^{-2}$ | 1 | $10^{-5}$ | $10^{-5}$ |
| Reynolds | Re | $\frac{\rho U L}{\mu}$ | 1 | 1 | $10^{-4}$ | $10^{-4}$ |
| Froude | Fr | $\frac{U^2}{gD}$ | $10^2$ | $10^{-4}$ | $10^{-2}$ | $10^{-6}$ |
| Weber | We | $\frac{\rho l U^2}{\sigma}$ | $10^{-5}$ | $10^{-2}$ | $10^{-11}$ | $10^{-10}$ |
| Péclet | Pe | $\frac{LU}{D}$ | $10^2$ | $10^2$ | $10^{-1}$ | $10^{-2}$ |

**Table 2.1:** List of dimensionless numbers for two-phase flow in channel and porous media. For the GDL a pore diameter and channel hydraulic diameter a value of $10\mu$m and 0.8mm is specified, respectively.

inertial forces for the gas phase inside the channel.

Another significant difference between the channel and the GDL is observed from the Péclet number, symbolizing the importance of inertia to mass diffusion. Interestingly, it appears that component flow in the channel is dominated by inertia, whereas diffusion dominates inside the GDL. This picture may change if an interdigitated flow field is used as opposed to a serpentine. In this case all flow is forced underneath the land and through the GDL hereby increasing the superficial velocity and the Peclet number inside the GDL.

In the following, a description is given of the gas-liquid flow patterns observed for channel flow and porous media.

### 2.1.1 Channel

The phenomena governing gas-liquid flow in a channel are highly dependent on the channel characteristic. Channels of a fuel cell typically fall into the

category of micro-channels and hence are subject to the forces discussed in section 2.1. In the literature several definitions exist of what constitutes a micro-channel, as discussed by Shao et al. [83] and Serizawa et al. [82]. Such definition are typically based on dimensionless numbers or geometrical length scales fulfilling certain criteria. An example of such a criteria is the following inequality:

$$\frac{\lambda}{D} \geq 3.3 \tag{2.1}$$

where $\lambda$ denotes the Laplace constant defined as

$$\lambda = \sqrt{\frac{\sigma}{g\left(\rho_L - \rho_g\right)}} \tag{2.2}$$

If the ratio between the Laplace constant and the hydraulic diameter is equal or larger than 3.3 the channel can be defined as a micro-channel. For the typical operational conditions of a DMFC the Laplace constant is $\lambda = 2.67e^{-3}$. This implies for the criterion to be fulfilled, the diameter has to be below 0.81mm. An alternative proposal based on a Eötvös criteria of $Eo < 0.88$ would instead lead to a larger diameter criteria of 2.6mm. Clearly, these criteria are simplified, and neglect keye-phenomena. It is not only the channel size that matters, gas-liquid flow in channels of DMFC is further complicated by the presence of the GDL, which has a high surface roughness and intrudes into the channel, effectively decreasing the cross-sectional area. Furthermore, bubbles and droplets tend to stick to the fibrous surface due to adhesion effects, which further cause flow hysteresis.

In general, for micro-channels the gas-liquid flow patterns shown in figure 2.2 are found [82]. However, these text-book examples do not necessarily occur for DMFC. As discussed by Anderson et al. [1], flow regimes for fuel cells depend not only on gas-liquid superficial velocities and the volume fraction of each fluid, but on the specific material use and system set-up. Hence, it is difficult to make generic flow pattern maps. This issue is further complicated by the fact that a distinction has to be made between the anode and cathode flow field due to a difference in two-phase morphology. In the following a short description is given based on experimental observation found in the literature, rather than specific flow pattern maps.

**Anode**

The gas-liquid flow of the anode is characterized by a liquid phase entering the channel, while a gas phase is continuously added from the GDL along

**(a)** Bubbly flow

**(b)** Slug flow

**(c)** Annular flow

**(d)** Droplet flow
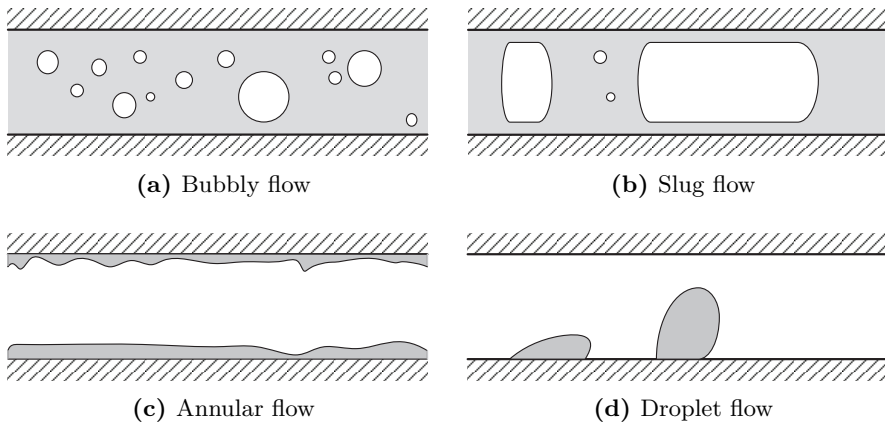
**Figure 2.2:** Liquid-gas flow patterns for micro-channels

the channel length. Inherently, this implies that the gas volume fraction increases from inlet to outlet. As was shown by Yang et al. [107] this similarly influences the flow patterns along the channel length depending on the orientation, i.e. vertical or horizontal. The gas-liquid flow patterns that were observed for the anode can be split into the following categories depending on mass quality along with liquid and gas volumetric fluxes:

- Bubbly flow

- Plug flow

- Slug flow

- Annular flow

For a vertical channel orientation and at low amounts of gas, two-phase flow is characterized as being bubbly. Hereafter, as the mass quality increases, slugs begin to appear. A further increase gradually turns slugs into an annular flow. The flow regimes observed for horizontal flow are similar to the ones encountered for vertical flow, with the exception of some extent of plug flow development a low mass quality. Interestingly, for both a bubbly flow layer forms attached to the GDL surface throughout the length of the channel. The detachment diameter of these bubbles can be estimated by balancing buoyancy and surface tension forces:

$$d_p = \left( \frac{4 d_c \sigma \sin \theta}{g \left( \rho_l - \rho_g \right)} \right)^{\frac{1}{3}} \tag{2.3}$$

where $d_c$ denotes the characteristic pore diameter of the GDL. Assuming that the gas bubbles leaving the GDL are through hydrophobic pores with a contact angle of $\theta = 120°$ and methanol solution 1 M is used, this leads to detachment particle size of $d_p = 0.525$mm. However, often smaller bubbles are observed [107].

**Cathode**

The liquid-gas flow regimes encountered at the cathode are inherently different then at the anode. At the cathode gas enters the channel, while droplets emerge from the GDL surface randomly along the channel length.

Hussaini and Wang [38] investigated liquid-gas flow patterns *in situ* and encountered the following four regimes depending on the gas and liquid superficial velocity:

- Single phase flow (i.e. mist flow)

- Droplet flow

- Film flow

- Slug flow

At high gas superficial velocities single phase flow is observed. Emerging liquid droplets quickly evaporate and only few sporadic droplets are observed. As the gas superficial velocity decreases more liquid droplets begin to emerge at the hydrophobic GDL surface. This regime is called droplet flow, since droplets stick to the GDL surface and slowly become pushed forward by the surrounding gas flow. When the current density increases the liquid superficial velocity increases and a film flow begins to form as droplets begin to coalesce and are wicked into the channel walls. With an additional increase in current density and liquid superficial velocity, film growth and consequently the formation of slug flow is observed. This tendency to generate slug flow is additionally enhanced at low superficial gas velocities for parallel channels, as shown by Zhang et al. [117]. This causes a significant increase in gas maldistribution and consequently results in increased performance loss.

## 2.1.2 Porous media

Two-phase flow pattern for porous media can quite well be classified by the relationship between the viscosity ratio and the capillary number. Moreover, a common way to describe the two-phase flow in porous media is in terms of imbibition and drainage. Imbibition is the displacement of one immiscible fluid by another caused by capillary pressure, whereas drainage is the process where the non-wetting phase displaces the wetting phase [21]. Lenormand et al. [47] found for drainage-type displacement that two-phase flow in porous media can be characterized by three different types of displacement:

- Viscous fingering

- Capillary fingering

- Stable displacement

When the viscosity ratio M < 1 and the capillary pressure ratio Ca $\gg$ 1 viscous forces control, causing viscous fingering, while capillary fingering prevail when M < 1 and Ca $\ll$ 1. However, if M $\gg$ 1 for Ca $\ll$ 1 viscous fingering becomes gradually more dense until a stable displacement is reached and a saturation jump profile is seen, whereas for Ca $\gg$ 1 no change is observed. From the dimensionless numbers describing the porous media of DMFC it is obvious that displacement is controlled by capillary fingering, since M = 0.1 and Ca = $10^{-8}$, as was concluded by Sinha and Wang [84].

## 2.2 Modeling Concepts

The modeling of gas-liquid flow is a challenging endeavor as their movement is governed by complex phenomena arising at the molecular level. For a two-phase model to be applicable to modeling of a fuel cell a trade-off between accuracy and computational efforts has to be made. Thus, some simplifications need to be made when describing flow on a macroscopic level.

The first step in fluid mechanics consists in describing a fluid as a continuum. In a fluid continuum the presence of individual molecules is ignored. Instead, the fluid is viewed as a continuous matter on which forces can be applied according to Newtons second law. Hence, fluid variables such as density velocity and pressure are merely a representations of an local instantaneous averaged molecular motion. This average is performed over a control volume containing a large number of molecules. Indeed, it is this control volume, associated with a single point which defines a fluid particle

in fluid mechanics, rather then a specific set of molecules.[63] The validity
of the fluid continuum assumption breaks down when length and time scales
approach those of molecules. The extent of this can be assessed by the mag-
nitude of the Knudsen number, $Kn$, which defines the ratio between the
mean free path of a molecule to the particle diameter. If $Kn \gg 10^{-3}$ the
assumption does not hold any longer.[40]

The motion of a fluid particle in single-phase flow can either be described
in a *Eulerian* or *Lagrangian* frame of reference. The *Eulerian* frame of ref-
erence describes motion of a fluid particle using an velocity field, which is a
function of space and time, and hence does not require tracking of individual
particles. Such a field is described in the form of partial differential equa-
tion (PDE). Alternatively, in the *Lagrangian* frame of reference, individual
particles are tracked, and their motion is described using Newtons second
Law, hereby describing their position in space as a function of time.[63]

However, this clear distinction between a Eulerian and Lagrangian frame
of reference breaks down in the case of several immiscible fluids, where a dis-
tinct and discontinuous interface forms between each fluid phase. Now fluid
transport has to be described as a combination of either types depending on
whether the flow morphology can be described as being dispersed or sepa-
rated. For liquid-gas flow in DMFC only two types are typically considered:

- The *Eulerian-Eulerian* method, or two-fluid method, models each fluid
  phase as a continuum, even though one fluid might be dispersed and
  the other continuous. Hence, conceptually we are dealing with inter-
  penetrating continua. This concept arises from its derivation, which
  is based on averaging the discontinuous interface that arises between
  phases in variables. The advantage of the two-fluid method is that it
  principally can compute any gas-liquid regime, provided that the inter-
  facial coupling terms are given through closure equations. Moreover,
  it is computationally quick, as opposed to tracking individual particles
  or resolving particles.[40] A subclass of the two-fluid approach is the
  mixture model.

    - The *Mixture* method does not distinguish between phases, it mod-
      els all phases as a single macroscopic continuum in an Eulerian
      frame of reference. In the literature several mixture models exist.
      In DMFC modeling two approaches dominate: the homogeneous
      and the multiphase mixture model.

        * The *Homogeneous* model is typically derived by summing the
          two-fluid equations or performing a macroscopic balancing

over all phases simultaneously.

* The *Multiphase Mixture* model takes a different approach. It solves for one velocity field, and in post-processing step reconstructs two separate velocity fields. However, this approach is only valid for porous media and hence in theory not applicable for channel flow modeling, though attempts have been made.

- The *Volume-of-fluid* (VOF) method is a so-called *high-resolution* method that resolves individual particles or free surfaces using small control and averaging volumes. The VOF method defines the location and orientation of the interface through a volume fraction function. The propagation of this volume fraction function can then be modeled by a single advection scheme or in a two-fluid formulation.

## 2.3 Two-Fluid Model

In the derivation of the two-fluid model the local instantaneous transport equation for quantity $\psi$ in phase $\alpha$ and the jump condition that arises at interface between phase $\alpha$ and $\beta$ are taken as starting point, respectively:

$$\underbrace{\frac{\partial \left(\rho_\alpha \psi_\alpha\right)}{\partial t}}_{\text{Transient}} + \underbrace{\nabla \cdot \left(\rho_\alpha \mathbf{V}_\alpha \psi_\alpha\right)}_{\text{Convective}} + \underbrace{\nabla \cdot \left(\mathbf{J}_\alpha\right)}_{\text{Diffusive}} = \underbrace{\sum_c \rho_{\alpha,c}\phi_{\alpha,c}}_{\text{Source}} \qquad (2.4)$$

$$\dot{m}_{I,\alpha\beta}\psi_\alpha + \dot{m}_{I,\beta\alpha}\psi_\beta + \mathbf{J}_\alpha \cdot n_{\alpha\beta} + \mathbf{J}_\beta \cdot n_{\beta\alpha} \quad = \quad \varphi_I + \sum_c \rho_{I,\alpha\beta,c}\phi_{I,\alpha\beta,c} \quad (2.5)$$

where $\mathbf{J}_\alpha$ and $\phi_c$ denote flux and source of the quantity $\psi$ in phase $\alpha$, and $\varphi_I$ denote interface transport phenomena. These local instantaneous variations described on a microscopic scale are then averaged out over a macroscopic scale. For a Eulerian description this can be accomplished using three different averaging procedures: *temporal-*, *spatial-* and ensemble averaging. The most common of these is volume averaging. This is due to its simplicity of realization and implementation. However, it is constrained by the characteristic size of the phases and flow. Temporal averaging is likewise easy to implement, however it requires a long averaging time, which might not be realizable for practical application. Ensembling averaging, on the other hand, avoids the shortcomings of time- or volume averaging by

averaging over an infinite number of realizations of the flow. It is therefore viewed as the more fundamental approach. Nevertheless, only a few publication exist in the literature.[40]

In following section the theoretical basis of deriving the two-fluid model is given. For the sake of simplicity, only equations derived using the volume averaging procedure are covered.

### 2.3.1   Volume Averaging

The volume averaging procedure essentially averages out local instantaneous variations ascribed to a volume in time. For this approach to be valid some constraints have to apply to the averaging volume:

$$
\left\{ \begin{array}{c} \text{Characteristic} \\ \text{length scale of} \\ \text{phases}, d_p \end{array} \right\} \ll \left\{ \begin{array}{c} \text{Characteristic} \\ \text{length scale of} \\ \text{averaging volume}, l \end{array} \right\} \ll \left\{ \begin{array}{c} \text{Characteristic} \\ \text{length scale of} \\ \text{physical system}, L \end{array} \right\}
\tag{2.6}
$$

In order to capture a stable average, the characteristic length scale of the averaging volume has to be much larger than the characteristic length scale of the phase volume. On the other hand, in order to obtain a local value of the flow the characteristic length scale of the averaging volume has to be much less than the characteristic length scale in the physical system due spatial changes. In regard to fuel cell modeling this can be illustrated for an electrode as seen in figure 2.3.

With the constraints of an averaging volume established, superficial and phase volume averages of the quantity $\psi$ in phase $\alpha$ can be defined, respectively:

$$
\langle \psi_\alpha \rangle_V = \frac{1}{V} \int_V \chi \psi_\alpha dV = \frac{1}{V} \int_{V_\alpha} \psi_\alpha dV
\tag{2.7}
$$

$$
\langle \psi_\alpha \rangle_{V_\alpha} = \langle \psi_\alpha \rangle_{V_\alpha}^{\chi_\alpha} = \frac{1}{V_\alpha} \int_{V_\alpha} \psi_\alpha dV
\tag{2.8}
$$

where $V$ is volume, $\chi_\alpha$ is a phase function that is 1 for phase $\alpha$ at time $t$, else it is zero. This generalized function assists in forming averages of local instantaneous variables across interfaces. This essentially ensures a valid mathematical treatment [40].

The two volume averaging operators are related to each other as follows:

$$
\langle \psi_\alpha \rangle_V = \frac{V_\alpha}{V} = \varepsilon s_\alpha \langle \psi_\alpha \rangle_{V_\alpha}
\tag{2.9}
$$
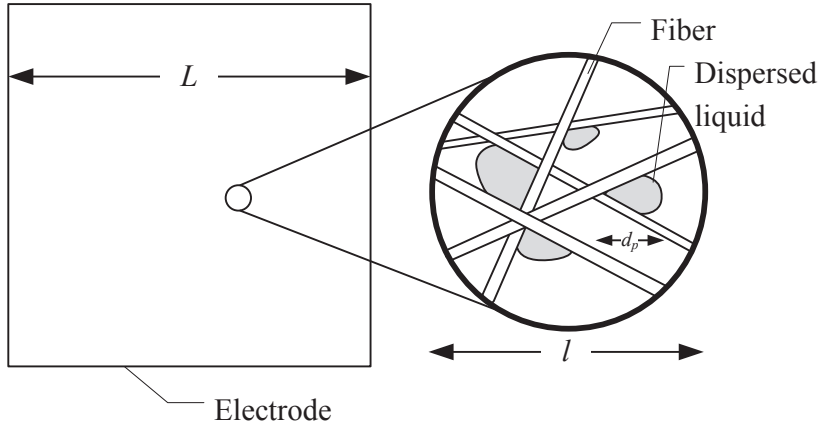
**Figure 2.3:** A schematic representation of the characteristic dimensions governing the two-fluid model in a DMFC

where $s_\alpha$ is the volume fraction of phase $\alpha$ and $\varepsilon$ is the volume porosity. For the volume fraction the following constraint applies:

$$\sum_{i=\alpha}^{N} s_i = 1 \tag{2.10}$$

A volume average of equation 2.4 can now be obtained by integrating the entire phase volume and dividing it by the average volume:

$$\left\langle \frac{\partial \rho_\alpha \psi_\alpha}{\partial t} \right\rangle_V + \langle \nabla \cdot (\rho_\alpha \mathbf{V}_\alpha \psi_\alpha + \mathbf{J}_\alpha) \rangle_V = \left\langle \sum_c \rho_c \phi_c \right\rangle_V \tag{2.11}$$

In order to rewrite the different terms of equation 2.11 into differentials of averages, two theorems are needed; one for the temporal and another for the spatial derivative. These theorems are sometimes referred to as Leibniz's and Gauss' rule of volume averaging, respectively [86, 104]:

$$\left\langle \frac{\partial \psi_\alpha}{\partial t} \right\rangle_V = \frac{\partial}{\partial t} \langle \psi_\alpha \rangle_V - \frac{1}{V} \int_{A_\alpha} \psi_\alpha u_I \cdot \mathbf{n} dA \tag{2.12}$$

$$\langle \nabla \psi_\alpha \rangle = \nabla \langle \psi_\alpha \rangle + \frac{1}{V} \int_{A_\alpha} \psi_\alpha \mathbf{n} dA \tag{2.13}$$

Applying these to the general instantaneous transport equation results in the following form:

$$
\frac{\partial \left( \varepsilon s_\alpha \left\langle \rho_\alpha \psi_\alpha \right\rangle_{V_\alpha} \right)}{\partial t} + \nabla \cdot \left( \varepsilon s_\alpha \left\langle \rho_\alpha \mathbf{V}_\alpha \psi_\alpha \right\rangle_{V_\alpha} \right) + \nabla \cdot \left( \varepsilon s_\alpha \left\langle \mathbf{J}_\alpha \right\rangle_{V_\alpha} \right) = \tag{2.14}
$$

$$
- \frac{1}{V} \int_{A_\alpha} \left( \dot{m}_\alpha \psi_\alpha + \mathbf{J}_\alpha \cdot \mathbf{n}_\alpha \right) dA + \varepsilon s_\alpha \left\langle \sum_c \rho_c \phi_c \right\rangle_{V_\alpha} \tag{2.15}
$$

The resulted transport equation is not yet suitable for modeling. One more step is needed where averages of products are related to products of averages instead. This is accomplished by introducing mass-weighted volume averages and the concept of spatial decomposition. The latter is an analog to the temporal decomposition used in the derivation of Reynolds Averaged Navier Stokes (RANS) equations.

The mass-weighted volume average of the quantity $\psi_\alpha$ is defined as:

$$
\left\langle \psi_\alpha \right\rangle_V^{\chi_\alpha \rho_\alpha} = \frac{\frac{1}{V} \int_V \rho_\alpha \chi_\alpha \psi_\alpha dV}{\frac{1}{V} \int_V \rho_\alpha \chi_\alpha dV} = \frac{\left\langle \rho_\alpha \psi_\alpha \right\rangle_V}{\left\langle \rho_\alpha \right\rangle_V} = \frac{\left\langle \rho_\alpha \psi_\alpha \right\rangle_{V_\alpha}}{\left\langle \rho_\alpha \right\rangle_{V_\alpha}} \tag{2.16}
$$

The spatial decomposition of the quantity $\psi_\alpha$ is defined as:

$$
\hat{\hat{\psi}}_\alpha = \psi_\alpha - \left\langle \psi_\alpha \right\rangle_V^{\chi_\alpha \rho_\alpha} \tag{2.17}
$$

where the double hat quatity $\hat{\hat{\psi}}$ denotes fluctuation due to both density and phase.

When applying the spatial decomposition to the convective term of the general transport equation an additional term due to microscopic spatial fluctuations appears:

$$
\left\langle \rho_\alpha \mathbf{V}_\alpha \psi_\alpha \right\rangle_{V_\alpha} = \left\langle \rho_\alpha \right\rangle_{V_\alpha} \left\langle \mathbf{V}_\alpha \right\rangle_V^{\chi_\alpha \rho_\alpha} \left\langle \psi_\alpha \right\rangle_V^{\chi_\alpha \rho_\alpha} + \left\langle \rho_\alpha \hat{\hat{\mathbf{V}}}_\alpha \hat{\hat{\psi}}_\alpha \right\rangle_{V_\alpha} \tag{2.18}
$$

By applying the spatial decomposition now to the remaining terms in the general transport equation one ends up with the following form:

$$
\frac{\partial \left( \varepsilon s_\alpha \left\langle \rho_\alpha \right\rangle_{V_\alpha} \left\langle \psi_\alpha \right\rangle_V^{\chi_\alpha \rho_\alpha} \right)}{\partial t} + \nabla \cdot \left( \varepsilon s_\alpha \left\langle \rho_\alpha \right\rangle_{V_\alpha} \left\langle \mathbf{V}_\alpha \right\rangle_V^{\chi_\alpha \rho_\alpha} \left\langle \psi_\alpha \right\rangle_V^{\chi_\alpha \rho_\alpha} \right) =
$$

$$
\nabla \cdot \left( \varepsilon s_\alpha \left\langle \mathbf{J}_\alpha \right\rangle_{V_\alpha} \right) - \frac{1}{V} \int_{A_\alpha} \left( \dot{m}_\alpha \psi_\alpha + \mathbf{J}_\alpha \cdot \mathbf{n}_\alpha \right) dA + \varepsilon s_\alpha \left\langle \sum_c \rho_c \phi_c \right\rangle_{V_\alpha} - \dots
$$

$$
\nabla \cdot \left( \varepsilon s_\alpha \left\langle \rho_\alpha \hat{\hat{\mathbf{V}}}_\alpha \hat{\hat{\psi}}_\alpha \right\rangle_{V_\alpha} \right) \tag{2.19}
$$

In addition to the before mentioned microscopic deviation term two more terms have appeared, when comparing equation 2.4 and 2.19. The first term accounts for interfacial stress, heat and species mass transfer:

$$\frac{1}{V} \int_{A_\alpha} \mathbf{J}_\alpha \cdot \mathbf{n}_\alpha dA$$

The second term accounts for interfacial transfer due to phase change across interface surface area:

$$\frac{1}{V} \int_{A_\alpha} \dot{m}_\alpha \psi_\alpha dA$$

The interfacial transfer term is typically generalized in the following form:

$$\frac{1}{V} \int_{A_\alpha} \dot{m}_\alpha \psi_\alpha dA, = \sum_{\beta=1}^{N_p} \left( \langle \dot{m}_{\alpha\beta} \rangle_V \langle \psi_\alpha \rangle_V^{\chi_\alpha \rho_\alpha} - \langle \dot{m}_{\alpha\beta} \rangle_V \langle \psi_\alpha \rangle_V^{\chi_\alpha \rho_\alpha} \right) \quad (2.20)$$

where $\dot{m}_{\alpha\beta}$ denotes the interfacial mass transfer term on a volumetric basis and which related to the interfacial area averaged mass transfer term as follows:

$$\langle \dot{m}_{\alpha\beta} \rangle_V = a \langle \dot{m}_{\alpha\beta} \rangle_{A_I} \quad (2.21)$$

where $a = A_I/V$ is the interfacial area density.

Often the notation in equation 2.19 is simplified by removing all averaging brackets and by combining some terms into a general source term $S$, which yields the following form:

$$\frac{\partial (\varepsilon s_\alpha \rho_\alpha \psi_\alpha)}{\partial t} + \nabla \cdot (\varepsilon s_\alpha \rho_\alpha \mathbf{V}_\alpha \psi_\alpha) = S_\alpha - \nabla \cdot \left( \varepsilon s_\alpha \rho_\alpha \hat{\mathbf{V}}_\alpha \hat{\tilde{\psi}}_\alpha \right)$$

$$+ \sum_{\beta=1}^{N_p} \left( \dot{m}_{\alpha\beta} \psi_\beta - \dot{m}_{\beta\alpha} \psi_\alpha \right) (2.22)$$

where $\psi_\alpha$ and $\mathbf{V}_\alpha$ now denote the mass-weighted and phase volume averaged of quantities.

Finally, applying the before mentioned averaging procedure to the jump condition leads to the following form:

$$\frac{1}{V} \int_{A_I} \left( \sum_\alpha [\dot{m}_\alpha \psi_\alpha + \mathbf{J}_\alpha \cdot \mathbf{n}_\alpha] \right) da = 0 \quad (2.23)$$

The different conservation equation used for describing two-phase flow can now be obtained by substituting the mass-weighted and volume averaged field quantity $\psi_\alpha$ by the variable of interest. However, some additional simplifications may need to be introduced in description of individual terms. In this work only laminar, steady-state flow is considered. Hence, turbulence and deviations from microscopic behavior are neglected in the following.

## 2.3.2   Mass Conservation

The mass conservation equation is simply obtained by setting $\psi_\alpha = 1$, $\mathbf{J}_\alpha = 0$ and $\phi_c = 0$ in the general transport theorem, equation 2.22:

$$\nabla \cdot \varepsilon s_\alpha \rho_\alpha \mathbf{U}_\alpha = S_\alpha + \sum_{\beta=1}^{N_p} (\dot{m}_{\alpha\beta} - \dot{m}_{\beta\alpha}) \tag{2.24}$$

where $S_\alpha$ denotes a mass sink or source. In DMFC modeling this could be due to electrochemical reactions or sorption/desorption to and from the electrolyte phase.

## 2.3.3   Component Conservation

The component conservation equation is obtained by substituting $\psi_\alpha = Y_{\alpha A}$, $\mathbf{J}_\alpha = J_\alpha$ and $\phi_c = S_\alpha/\rho_c$ into the general transport theorem, equation 2.22:

$$\nabla \cdot (\varepsilon s_\alpha \rho_\alpha \mathbf{U}_\alpha Y_{A\alpha} - \varepsilon s_\alpha J_\alpha) = \varepsilon s_\alpha S_\alpha + \sum_{\beta=1}^{N_p} (\dot{m}_{\alpha\beta} Y_{A\beta} - \dot{m}_{\beta\alpha} Y_{A\alpha}) \tag{2.25}$$

where $Y_{A\alpha}$ denotes mass fraction of species $A$ in phase $\alpha$. If the number of species is $N$, then the number of independent mass fractions is $N-1$ according to:

$$\sum_{i=A}^{N} Y_i = 1 \tag{2.26}$$

For binary mixtures the diffusive flux can be described using Fick's law, whereas for multicomponent mixtures it can be described using a generalized Fick's law description based on Maxwell-Stefan diffusion, respectively:

$$J_\alpha = \rho_\alpha D_{A\alpha}^{eff} \nabla Y_{A\alpha} \tag{2.27}$$

$$J_\alpha = \sum_{i=\alpha}^{N-1} \rho_i D_{Ai}^{eff} \nabla Y_{Ai} \tag{2.28}$$

where $D_{A\alpha}^{eff}$ is the effective mass diffusivity that is corrected for dispersion effects and Knudsen diffusion in porous media. The build-in diffusive flux in CFX is described using Fick's law, thus it neglects interaction between species in multi-component flow. In this model this is to some extent circumvented by using Wilkes formula to obtain an effective diffusivity, similarly as Berning et al. [12].

## 2.3.4 Momentum Conservation

The momentum conservation equation for dispersed flow is obtained by substituting $\psi_\alpha = Y_{\alpha A}$, $\mathbf{J}_\alpha = \tau$ and $\phi_c = g_c$ into the general transport theorem, equation 2.22, and simplifying the interfacial momentum stresses by neglecting variations in surface tension and pressure difference at the interfaces:

$$\nabla \cdot (\varepsilon s_\alpha \rho_\alpha \mathbf{U}_\alpha \mathbf{U}_\alpha - \varepsilon s_\alpha \boldsymbol{\tau}) = \varepsilon s_\alpha (\mathbf{S}_\alpha - \nabla p_\alpha) + \varepsilon s_\alpha \rho_\alpha g + \mathbf{F}_\alpha + ...$$
$$\sum_{\beta=1}^{N_p} (\dot{m}_{\alpha\beta} \mathbf{U}_\beta - \dot{m}_{\beta\alpha} \mathbf{U}_\alpha) \tag{2.29}$$

where $\boldsymbol{\tau} = \mu_\alpha \left[ \nabla \mathbf{U}_\alpha + (\nabla \mathbf{U}_\alpha)^T - \frac{2}{3} \nabla \cdot \mathbf{U}_\alpha \right]$ is viscous stress, $g$ is gravity and $\mathbf{F}_\alpha$ is the generalized interfacial drag term. For dilute mixtures the generalized drag term accounts for drag, lift, virtual mass and Basset history:

$$\mathbf{F}_\alpha = N_d \left( \mathbf{f}_D + \mathbf{f}_L + \mathbf{f}_V + \mathbf{f}_B \right) \tag{2.30}$$

where $N_d$ accounts for the number of particles per unit volume and $\mathbf{f}_D$, $\mathbf{f}_L$, $\mathbf{f}_V$ and $\mathbf{f}_B$ are the drag force, lift force, virtual mass force and Basset history force. For two-phase flow inside porous media of a fuel cell the generalized interfacial drag term can solely be described by Darcy's law [96]:

$$\mathbf{F}_\alpha = \frac{\varepsilon^2 s_\alpha^2 \mu}{k_{rel}} \overline{\mathbf{K}}^{-1} \mathbf{U}_\alpha \tag{2.31}$$

where $\overline{\mathbf{K}}$ is the hydraulic permeability matrix and $k_{rel}$ is relative permeability of phase $\alpha$. Darcy's law is an empirical correlation valid for low velocities. At higher velocities the Darcy-Forchheimer equation is recommended, as it has a second term accounting for inertial forces. Further,

for porous media, the earlier mentioned assumption of negligible interfacial pressure difference

$$p_\alpha = p_\beta = p \tag{2.32}$$

is invalid. Inside porous media, when two immiscible fluids are present, a pressure difference forms at any point along a curved interface. This pressure difference is known as capillary pressure and is defined as follows:

$$p_c = p_\alpha - p_\beta \tag{2.33}$$

where $p_c$ is capillary pressure, $p_\alpha$ is the non-wetting phase and $p_\beta$ is the wetting phase. A convenient way to describe the capillary pressure of a porous medium is by means of the dimensionless Leverett J function. This expression describes the relationship between capillary pressure, the characteristic pore radius $\sqrt{K/\varepsilon}$, surface tension $\sigma$ and the contact angle $\theta$, as a function of volume fraction. In its original form the Leverett J function is meant only to account for either hydrophilic or hydrophobic non-connected capillary tubes, and not the simultaneous presence of both. Hence, a modified Leverett J function is used based on an effective volume fraction, as depicted in the following:

$$p_c = \sigma \cos\theta \left(\frac{\varepsilon}{K}\right)^{\frac{1}{2}} J\left(S\right) \tag{2.34}$$

$$J\left(S\right) = 1.417\left(1 - S\right) - 2.120\left(1 - S\right)^2 + 1.263\left(1 - S\right)^3 \tag{2.35}$$

$$S = \begin{cases} \frac{s - f_{Hi}}{1 - f_{Hi}}, & s > f_{Hi} \\ \frac{f_{Hi} - s}{f_{Hi}}, & s < f_{Hi} \end{cases} \tag{2.36}$$

where $S$ denotes the effective volume fraction, $f_{Hi}$ is the hydrophilic pore fraction, $\theta$ is a contact angle switch function where $\theta > 90°$ for $s > f_{Hi}$ and $\theta < 90°$ for $s < f_{Hi}$, and $\sigma$ is the mixture surface tension, which is a non-linear function of methanol concentration [94]. It should be noted that in porous media modeling the term saturation is used synonymous for volume fraction.

The resulting Leverett J function for a typical GDL and MPL is shown in figure 2.4a. The effect of including the hydrophilic pore fraction can be seen from the intersection with the y-axis. From comparing the resulting
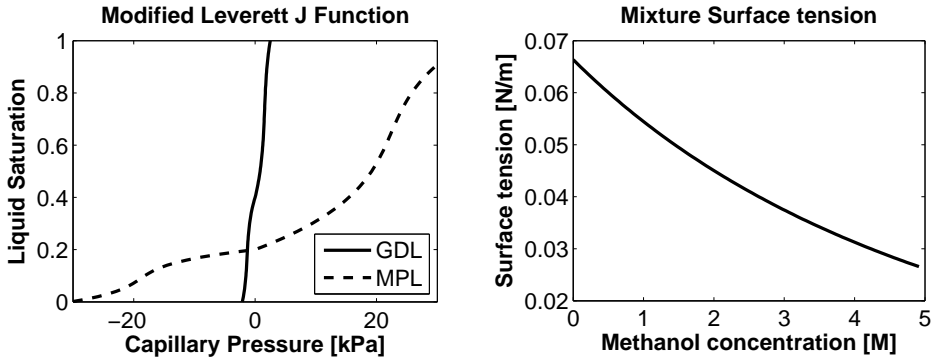
**(a)** Modified Leverett J function for a GDL and MPL at $60°$C and methanol concentration of 1 M

**(b)** Surface tension as a function of methanol concentration at $60°$C

**Figure 2.4:** Phenomena captured by the capillary pressure model

capillary curves it is clear that significant discontinuities in the liquid saturation can arise at the interface between layers, since the pressure field across the interface has to be continuous.

The dependence of the surface tension on methanol concentration is shown in figure 2.4b. From this figure it can be observed how the surface tension of a methanol solution decreases significantly when slightly increasing the concentration. In the literature this effect is often neglected when modeling capillary pressure effects for DMFC.

### 2.3.5  Energy Conservation

The energy conservation equation can be derived in different ways depending on which phenomena are accounted for when defining energy. The energy of a flowing fluid is usually defined as:

$$E = e + \frac{P}{\rho} + \frac{1}{2}U^2 = H + \frac{1}{2}U^2 \tag{2.37}$$

where $e$, $P$ and $H$ denote internal energy, pressure and enthalpy.

However, at low velocities and for incompressible flow it can be beneficial to neglect mechanical and volumetric expansion energy due to numerical convergence challenges. Hence, in this work only thermal or internal energy is accounted for as follows:

$$e = H - \frac{P}{\rho} \simeq c_p \left( T - T_{ref} \right) \tag{2.38}$$

where $T$ denotes temperature. Thus, the energy conservation equation is simplified to account only for changes in thermal energy. This leads to the following conservation equation:

$$\nabla \cdot \varepsilon s_\alpha \rho_\alpha \mathbf{U}_\alpha e_\alpha = \nabla \cdot \varepsilon s_\alpha \lambda_\alpha \nabla T_\alpha + \varepsilon s_\alpha : \nabla U_\alpha + \nabla \cdot \varepsilon s_\alpha \left( \sum_{i=1}^{N_c} \Gamma_i h_i \nabla Y_i \right) + ...$$

$$\mathrm{S}_\alpha + \sum_{\beta=1}^{N_p} \left( \dot{m}_{\alpha\beta} e_\beta - \dot{m}_{\beta\alpha} e_\alpha \right) \tag{2.39}$$

where $\mathrm{S}_\alpha$ is an energy sink or source term. In DMFC modeling energy source term could either be due to electrochemical reactions or charge transport.

### 2.3.6   Closure Equations

As depicted in table 2.2 a difference can be seen in the number of variables and conservation equations needed to model a DMFC. In order to close the description of the two-fluid model additional constitutive relations are needed. The number of independent variables are in part reduced by pressure, mass fraction and volume fraction constraints (i.e. equation 2.10, 2.26 and 2.32, respectively) and in part by assuming that the liquid phase is incompressible and that the gas phase density can be described using the ideal gas equation:

$$\rho_A = \frac{p_A M_w}{R T_A} \tag{2.40}$$

$$\rho_g = \frac{1}{\sum_{i=A}^{N} \frac{Y_i}{\rho_i}} \tag{2.41}$$

Moreover, additional constitutive relations are needed in algebraic form to close the description of non-equilibrium phase change and the associated thermodynamics, non-equilibrium sorption-desorption from and to the electrolyte phase, electrochemistry, generalized drag term, relative permeability and effective diffusivities. All of these constitutive relations are described in the collection of papers.

| Parameters | Domain | |
|---|---|---|
| | Cathode | Anode |
| Number of phases | 3 | 3 |
| Species in gas phase | $N_2$, $O_2$, $CO_2$, $H_2O$ | $CO_2$, $H_2O$, $CH_3OH$ |
| Species in liquid phase | $H_2O$ | $H_2O$, $CH_3OH$ |
| Species in solid phase | $e^-$ | $e^-$ |
| Independent variables | $s_l$, $p_g$, $U_l$, $V_l$, $W_l$, $U_g$, $V_g$, $W_g$, $T_g$, $T_l$, $Y_{g,O_2}$, $Y_{g,CO_2}$, $Y_{g,H_2O}$ | $s_l$, $p_g$, $U_l$, $V_l$, $W_l$, $U_g$, $V_g$, $W_g$, $T_g$, $T_l$, $Y_{l,CH_3OH}$, $Y_{g,CH_3OH}$, $Y_{g,H_2O}$ |
| Dependent variable | $s_g$, $p_l$, $Y_{g,N_2}$, $\rho_g$ | $s_g$, $p_l$, $Y_{g,CO_2}$, $Y_{l,H_2O}$, $\rho_g$ |
| Number of variables | 17 | 18 |
| Number of independent variables | 13 | 13 |
| Number of conservation equations | 13 | 13 |

**Table 2.2:** Data on the application of a two-fluid model of a DMFC

### 2.3.7 Model Limitations

A clear challenge in applying the two-fluid model to the DMFC modeling applies to assumption of dispersed flow. As seen in section 2.1.1 liquid-gas flow in both channels tend to form slugs or annular flow where interfacial forces become dominant. In the anode it is only at low fractions of gas phase or equivalently at high methanol stoichiometry that dispersed bubbly flow can be assumed. Similarly, for the cathode it is only at low fractions of liquid phase or equivalently high air stoichiometries that dispersed droplet flow or mist flow can be assumed valid. Else, a VOF model needs to be considered for channel flow.

Another issue in modeling two-phase flow using a two-fluid model based on Darcy's law is the ability to capture capillary or viscous fingering in porous media. As such Darcy's equation assumes a uniform pore structure and wettability, and therefore cannot capture these phenomena. Hence, it should more be viewed as an average representation of these phenomena in porous media.

# Chapter 3

# Modeling of Transport Phenomena in PEM

*In this chapter the physics governing dilute water and methanol transport in polymer electrolyte membranes based on Nafion are presented and discussed. As a point of origin the sorption of gas and liquids is taken. Hereafter the kinetics governing sorption-desorption are discussed, along with transport of sorbed species.*

## 3.1  Morphology of Nafion

The morphological description of Nafion is of great importance in the understanding of its transport properties. By better understanding how structural information affects transport properties of perfluorosulfonated ionomers improved electrolyte membranes can be developed. In addition, it can help to improve our understanding of the macroscopic transport phenomena governing fuel cell operation. As pointed out by Mauritz and Moore [56] developing such morphological models is a complicated matter because of the random chemical structure of the co-polymer, the complexity of co-organized crystalline and ionic domains, the large morphological variations with solvent swelling, among others. Thus, many different morphology models have been proposed, however none are believed to give a universal description, yet.

The most popular model has for many years been the Cluster-Network model by Hsu and Gierke [37]. In this model Nafion is described at the nanometer-scale as consisting of ionic clusters that are approximately spherical in shape with an inverted micellar structure. These clusters are hydrophilic due to sulfonic acid groups, whereas the polymer matrix is hy-
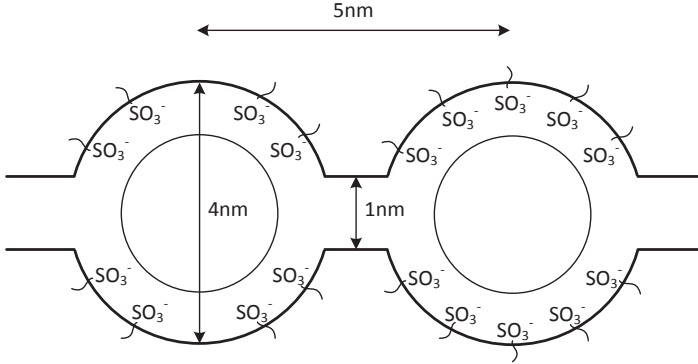
**Figure 3.1:** The Cluster-Network Model by Hsu and Gierke [37]

drophobic due to the PTFE backbone. As polar solvent sorption increases these ionic clusters expand and become interconnected by narrow channels allowing for ionic percolation pathways for ionic and increased water transport. Interestingly, this conceptual recognition by Hsu and Gierke [37] that ionic groups aggregate to form micro phase separated clusters that allow for swelling by polar solvents and facilitate ion transport is a recurring phenomenological concept in all models, as discussed by Mauritz and Moore [56]. Although alternative morphology models of Nafion exists, such as the lameller model or the rodlike model [77], which probably more adequate describe the actually morphology, the Cluster-Network model can still be helpful in interpreting transport phenomena in a PEM.

## 3.2   Gas-Liquid Sorption

The study of sorption of methanol and water in gaseous and liquid form into PEM is of great importance in the understanding of methanol and water crossover in DMFC. Particularly the reported existence of what is known as Schroeder's paradox as well as sorption isotherms and methanol-water-PEM equilibria have a great impact on transport phenomena.

Before addressing these subjects in the context of DMFC modeling it is helpful to define the number of water and methanol molecules sorbed relative to the number of sulfonic acid sites. This dimensionless quantity is named the species content:

$$\lambda_j = \frac{n_j}{n_{SO_3^-}} \tag{3.1}$$

where $n$ is the number of moles.

### 3.2.1   On Schroeder's Paradox and Sorption Kinetics

In short, Schroeder's paradox is the experimental observation that a difference in water sorption occurs when a PEM is equilibrated by a vapor and a liquid having the same chemical potential and hence the same driving force for sorption. In the literature different views exist on this subject. Onishi et al. [71], Jeck et al. [42] believe it to be an experimental artifact either caused by thermal history and treatment of Nafion. Alternatively, Benziger et al. [8], Schneider and Rivin [80], Zhao et al. [118] ascribe it to the dynamics of interfacial water absorption, whereas Choi and Datta [16], Freger [25], Elfring and Struchtrup [23] believe it is due to a difference in the surface energy between the vapor-Nafion and liquid-Nafion interfaces. The puzzling thing about these views are that they often are experimentally substantiated not only for saturated vapors and liquids (i.e. at an activity equal to 1), but over a wide range of activities.

Jeck et al. [42] showed the absence of Schroeder's paradox for a water activity range between 0.7 to 1.0 using a polymeric deswelling agent, while Bass and Freger [6] showed the existence of Schroeder's paradox for a water activity range from 0.3 to 1.0 using polyvinylsulfonic acid salts as an osmotic stressor. From these studies it is not clear who is right or wrong, or whether the measurement techniques have impacted results. Bass et al. [7] argued that the absence of Schroeder's paradox as observed by Onishi et al. [71] over a long equilibration period can be explained by changes in the surface morphology of Nafion. The underlying assumption being two-fold: (1) that the surface of Nafion is hydrophilic in contact with a liquid and hydrophobic in contact with a vapor, and (2) that the Nafion surface is thought to become unstable at saturation and hence gradually changes from a hydrophobic to a hydrophilic surface. Subsequently, vapor begins to condensate onto the hydrophilic surface to form a thin liquid film layer, which enhances the sorption process. This difference in hydrophobicity of vapor and liquid, is also argued by Majsztrik et al. [53] as the cause of a difference in interfacial resistance. This line of reasoning is additionally substantiated by the work of Kusoglu et al. [45]. They concluded that Nafion depicts two time regimes for both liquid and vapor sorption. Whereas the first regime occurs in seconds for both, the second for vapor is much slower then the one by a liquid phase. A difference of $1.0e^4$ is reported. This is similar to a reported factor of $1.0e^3$ measured by Benziger et al. [8]. Hence, it could seem that Schroeder's paradox is a reflection of the interfacial dynamics of water absorption caused

by a difference in surface energy.

From a macroscopic modeling point of view it is unrealistic to account for a long-term equilibration time of a month. It therefore makes sense to assume a short-term equilibrium value for saturated vapor with matching kinetics. In order to couple these observation with a two-phase model a volume fraction weighted non-equilibrium sorption-desorption model is used to represent the difference in exposure to vapor and liquid:

$$\dot{m}_s = \underbrace{s_l A k_l \frac{\rho_{mem}}{EW} \left( \lambda_{eq,l} - \lambda \right)}_{\dot{m}_{s,l}} + \underbrace{s_g A k_g \frac{\rho_{mem}}{EW} \left( \lambda_{eq,g} - \lambda \right)}_{\dot{m}_{s,g}} \qquad (3.2)$$

where $\lambda_{eq,l}$ and $\lambda_{eq,g}$ are the equilibrium species content when exposed to a liquid and a vapor, respectively, $A$ is the specific surface area of Nafion, $k$ is the sorption/desorption kinetic rate, $\rho_M$ is the membrane density, and $EW$ is the equilvalent weight of Nafion. In the following the sorption equilibria for liquid mixtures of methanol and water in Nafion as well as the sorption isotherms for both methanol and water vapor will be discussed.

## 3.2.2   Liquid Methanol-Water Equilibria

From the methanol-water equilibria depicted in figure 3.2 it is evident that the sorption of a liquid methanol-water mixture in Nafion is governed by non-ideal thermodynamics. As the methanol molar fraction increases so does the total uptake. Moreover, as discussed by Geiger et al. [30] this mixed uptake seems to be nearly temperature independent.

Interestingly, for dilute methanol solutions it appears that the uptake of water is almost constant with respect to methanol molar fraction of the equilibrating solution, whereas the uptake of methanol depicts a linear dependence. Hence, for the intended operation range of methanol concentration (i.e. 0 to 5 M) it is reasonable to assume a simplified equilibrium model. For methanol sorption this leads to the following relation between methanol activity and methanol content:

$$\lambda_{eq,\text{CH}_3\text{OH}} = 5.635 a_{\text{CH}_3\text{OH},l} + 30.3259 a_{\text{CH}_3\text{OH},l}^2$$

where $a_{\text{CHOH},l}$ is liquid methanol phase activity.

## 3.2.3   Vapor Sorption Isotherm

Short-term sorption isotherms for methanol and water are depicted in figure 3.3. When comparing the measurements by Zhao et al. [119] and Rivin et al.
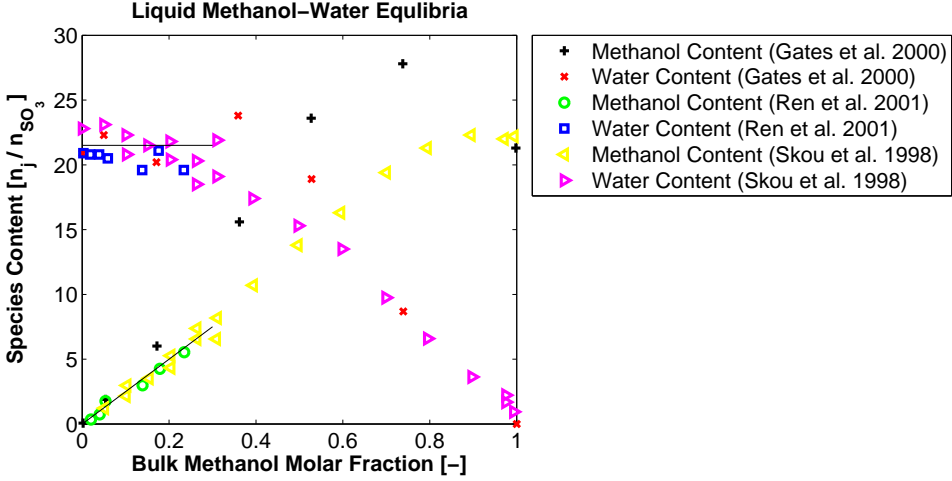
**Figure 3.2:** Methanol-water equilibria as a function of methanol molar fraction [27, 85, 75]

[76] for both methanol and water it cannot unambiguously be concluded that one sorbs easier into Nafion than the other. Moreover, both sorption of methanol and water seem to be independent of temperature change as pointed out by Zhao et al. [119].

Unfortunately, no studies have yet been carried out for the sorption of vapor mixtures of water and methanol. It is therefore difficult to tell how this impacts the uptake. Hence, in this work a similar methanol molar fraction dependence is adapted as seen for liquid methanol-water mixtures normalized by the difference in vapor and liquid uptake for an activity of 1:

$$\lambda_{eq,\mathrm{CH_3OH}} = 5.635 a_{\mathrm{CH_3OH},g} + 30.3259 a_{\mathrm{CH_3OH},g}^2$$

where $a_{\mathrm{CH_3OH,g}}$ is the methanol vapor phase activity.

## 3.3 Transport Phenomena

For mass transport in porous media the following generalized Maxwell-Stefan equation (or often referenced to as binary friction model) can be used [44]:

$$-\frac{c_j}{RT}\nabla_{T,p}\mu_j - \frac{c_j}{RT}V_j\nabla p - \frac{\alpha'_j}{K}\nabla p - c_j z_j \frac{F}{RT}\nabla\phi = \sum_{i\neq j}\frac{x_i N_j - x_j N_i}{D_{ij}^{eff}} + \frac{N_j}{D_{jM}^{eff}} \tag{3.3}$$
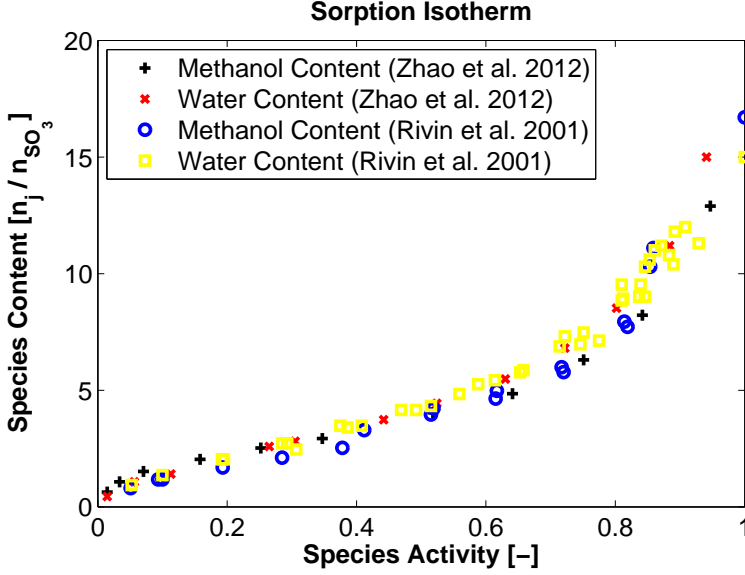
**Figure 3.3:** Adsorption isotherms for methanol and water vapor [76, 119]

Where $\mu$ represents the chemical potential, $c$ concentration, $p$ pressure, $\phi$ electrical potential, $D_{ij}$ effective Maxwell-Stefan binary diffusivities and $N$ species flux. In equation 3.3, the left hand side accounts for the driving forces of species $j$ and the right hand side accounts for the binary friction forces balancing them.

For the purpose of modeling mass transport through a PEM, it is common to neglect the pressure and temperature dependence of the chemical potential due to low compressibility and temperature variations, whereby the chemical potential gradient simplifies to only an activity gradient. Moreover, viscous flow due low permeability and small pressure gradients are neglected. Although a PEM is not fully impermeable to gases like carbon dioxide, oxygen and nitrogen, crossover of these species is typically ignored in PEM modeling as it is significantly less then that of water and methanol. With these simplification the following transport equation is obtained [24, 81]:

$$-\frac{c_j}{RT}\nabla_{T,p}\ln a_j - c_j z_j \frac{F}{RT}\nabla\phi = \sum_{i\neq j}\frac{x_i N_j - x_j N_i}{D_{ij}^{eff}} + \frac{N_j}{D_{jM}^{eff}} \qquad (3.4)$$

where $j =$H$^+$, H$_2$O, CH$_3$OH are the species accounted for and $z_j = 1$, 0, 0 are the species charges.

By solving for species fluxes along with grouping molar fractions and binary frictions terms into new diffusivity groups the following matrix form can be obtained:

$$
\begin{bmatrix} N_{\mathrm{H^+}} \\ N_{\mathrm{H_2O}} \\ N_{\mathrm{CH_3OH}} \end{bmatrix} = \begin{bmatrix} D_{11} & D_{12} & D_{13} \\ D_{21} & D_{22} & D_{23} \\ D_{31} & D_{32} & D_{33} \end{bmatrix} \begin{bmatrix} c_{\mathrm{H^+}} F \nabla \phi + c_{\mathrm{H^+}} \nabla a_{\mathrm{H^+}} \\ c_{\mathrm{H_2O}} \nabla a_{\mathrm{H_2O}} \\ c_{\mathrm{CH_3OH}} \nabla a_{\mathrm{CH_3OH}} \end{bmatrix} \tag{3.5}
$$

A problem with solving this equation is to obtain the individual Maxwell-Stefan binary diffusivities. Moreover, they are often concentration dependent which necessitates a large amount of data-fitting. Hence, a dilute solution theory assumption is therefore usually made in DMFC modeling. This includes neglecting the effect of proton diffusion as well as the species-species interaction between water and methanol. Doing these simplifications and rewriting diffusivities in a more familiar form yields:

$$
\begin{bmatrix} N_{\mathrm{H^+}} \\ N_{\mathrm{H_2O}} \\ N_{\mathrm{CH_3OH}} \end{bmatrix} = \begin{bmatrix} F\sigma & 0 & 0 \\ \frac{n_d}{F}\sigma & D_{\mathrm{H_2O,a}} & 0 \\ \frac{n_d}{F}\sigma & 0 & D_{\mathrm{CH_3OH,a}} \end{bmatrix} \begin{bmatrix} \nabla \phi \\ c_{\mathrm{H_2O}} \nabla a_{\mathrm{H_2O}} \\ c_{\mathrm{CH_3OH}} \nabla a_{\mathrm{CH_3OH}} \end{bmatrix} \tag{3.6}
$$

where $D_{\mathrm{H_2O,a}}$ and $D_{\mathrm{CH_3OH,a}}$ are the self-diffusivities of water and methanol in Nafion, respectively, $\sigma$ is the ion conductivity and $n_d$ is the EOD coefficient and $i = N_{\mathrm{H^+}}/F$ is the ion current density. This transport equation is often referred to as the diffusive model proposed by Springer et al. [88].

The species content driving force can further be related to the species activity driving force as follows through a thermodynamic correction factor often referred to as Darken factor:

$$
\nabla \ln a_j = \frac{d \ln a_j}{d \ln \lambda_j} \nabla \lambda_j \tag{3.7}
$$

Moreover, concentration can be rewritten relative to dry membrane conditions and hence ignoring the effect of swelling:

$$
c_j = \rho_M \lambda_j / EW \tag{3.8}
$$

By inserting equation 3.7 and 3.8 into equation 3.4, and enforcing mass conservation yields the following dilute solution theory model:

$$
\nabla \cdot (-\sigma \nabla \phi) = R \tag{3.9}
$$

$$\nabla \cdot \left( \frac{\rho_M}{EW} D_{\lambda,A} \nabla \lambda_A \right) = \nabla \cdot \left( \frac{n_d}{F} \sigma \nabla \phi \right) + S_A \tag{3.10}$$

$$D_{\lambda,A} = D_{a,A} \lambda_A \frac{d \ln a_A}{d \ln \lambda_A} \tag{3.11}$$

where $S_A$ is a mass sink or source term due sorption/desorption in CL and $R$ is electrochemical reaction rate. In the following relations are given for the ion conductivity, EOD coefficients and diffusivities of methanol and water. Moreover, their dependence on species content, composition and temperature is discussed.

### 3.3.1   Conductivity

The ion conductivity of Nafion is known to depict a strong dependence on water content, as seen in figure 3.4. In accordance with the Cluster-Network model, ion conduction is enabled once the hydrophilic clusters have expanded enough to become interconnected. As discussed by Sone et al. [87], and likewise observed in the figure 3.4, a water content of at least $\lambda = 2$ is required to achieve this. From here on a sudden, non-linear rise in conductivity is seen. Once Nafion reaches a water content of $\lambda = 4$ a transition to a almost linear dependence occurs. Furthermore, ion conductivity depicts an Arrhenius type temperature dependence; the higher the temperature the higher the ion conductivity. This is in accordance with the vehicle mechanism and ion hopping.

Meanwhile, the relationship between conductivity and water content can be shifted dependent on the heat-treatment Nafion receives during preparation. In its expanded form (E-form), i.e. dried in vacuum at room temperature, the highest conductivity is seen as opposed to its shrunken form (S-form), i.e. dried at above 103°C during vacuum. This difference is caused by a collapse of the membrane structure. The closer the temperature comes to the glass-transition point of Nafion, the more Nafion shrinks.

For modeling of an E-form membrane the following conductivity function was found by Springer et al. [88]:

$$\sigma = (0.005139\lambda - 0.00326) \exp \left[ 1268 \left( \frac{1}{303} - \frac{1}{T} \right) \right] \tag{3.12}$$

where $T$ is the polymer temperature. It should be noted that this function only is valid in the linear region above a water content of approximately $\lambda = 4$.
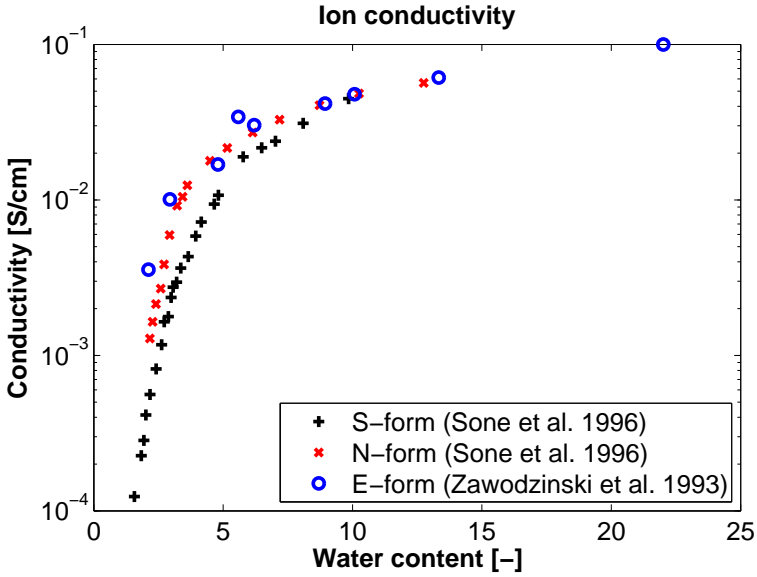
**Figure 3.4:** Ion conductivity of Nafion in various forms [114, 87]

## 3.3.2 Electro-osmotic Drag

For a fully hydrated Nafion membrane the EOD coefficients of methanol and water are a function of methanol molar fraction and temperature [92, 34]. As seen from figure 3.5, the total EOD increases as a function of methanol molar fraction of the equilibrating solution; this is a similar effect as seen for the mass uptake. Moreover, the EOD coefficient of methanol seems to become marginal for low fractions of methanol. It appears that methanol has a higher tendency to stick to the polymer backbone structure than water [34]. The total EOD coefficient also increases with temperature. At lower temperatures a weak temperature dependence is seen. This is ascribed to the Grotthuss mechanism. At higher temperatures the vehicle mechanism becomes more important and a stronger temperature dependence is observed [92]. A similarly temperature dependence has been observed by Ren et al. [75] and Luo et al. [52].

The following equations were fitted to the experimental data from Hallberg et al. [34] for a fully hydrated Nafion and normalized by the EOD coefficient of water at zero methanol molar fraction and corrected for temperature using an Arrhenius type temperature correction:

$$n_{d,H_2O,mix} = n_{d,\mathrm{H_2O}} \left(1.0 - 0.72 X_{C\mathrm{H_3OH}}\right) \exp\left[1268\left(\frac{1}{303} - \frac{1}{T}\right)\right] \quad (3.13)$$

$$n_{d,C\mathrm{H_3OH},mix} = n_{d,\mathrm{H_2O}} \left(X_{C\mathrm{H_3OH}} + 1.058 X^2_{C\mathrm{H_3OH}}\right) \exp\left[1268\left(\frac{1}{303} - \frac{1}{T}\right)\right]$$
$$(3.14)$$

where $X$ is the mole fraction.
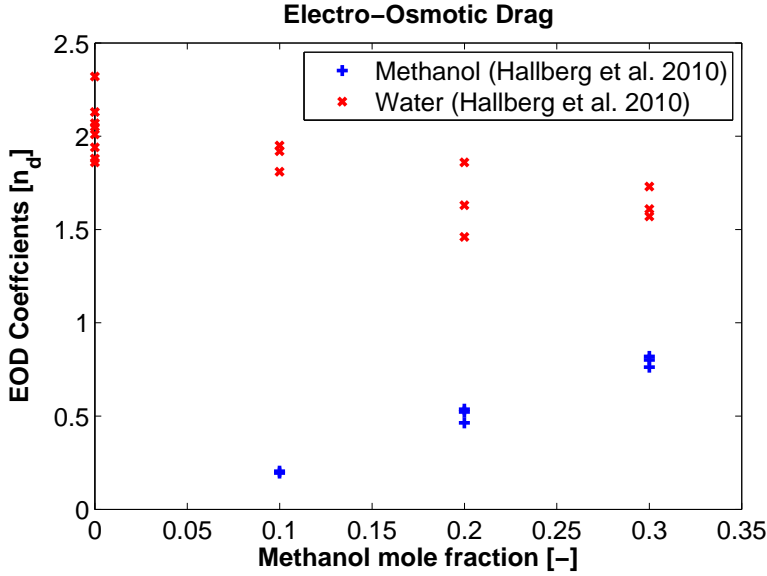


**Figure 3.5:** Electro-osmotic drag coefficient of water, methanol and total species transport measured by Hallberg et al. [34].

Meanwhile, the EOD coefficient of methanol and water are not only a function of species composition but also species content [52]. For vapor-equilibrated and pre-dried Nafion a constant total EOD coefficient of 1 is observed [115]. To account for a transition between an fully and partial hydrated Nafion membrane the following functions is used:

$$n_{d,\mathrm{H_2O}} = \max\left(\frac{2.5\lambda_{\mathrm{H_2O}}}{22}, \ 1.0\right) \qquad (3.15)$$

### 3.3.3 Diffusivity

The diffusivities of water and methanol in Nafion have been subject to intensive research and discussions due to inconsistencies in the reported values and the apparent observation of a local maximum in the dependency on water content. It was not until recently that it was shown by Majsztrik et al. [54] and Satterfield and Benziger [78] that these discrepancies can be attributed to membrane swelling and sorption/desorption phenomena.
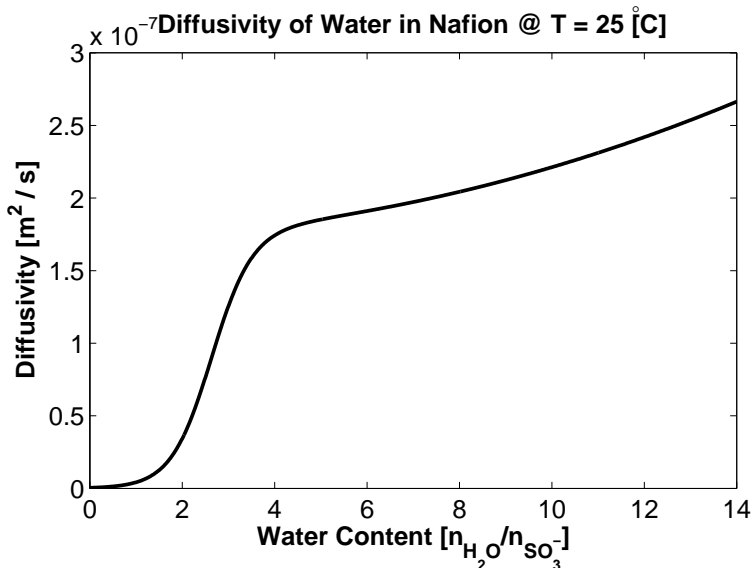


**Figure 3.6:** The diffusivity of water in Nafion as a function water content at 303K

Meanwhile, no satisfactory explanation was found for the predicted local maxima in the diffusivity of water shown by Springer et al. [88] and Zawodzinski et al. [113]. It was therefore in Paper 3 attempted based on the recent self-diffusivity measurements by Zhao et al. [118] to investigate the effect of various combinations of water sorption isotherms to demonstrate that this alleged spike was merely a mathematical artifact of deriving a concentration dependent diffusivity based on the self-diffusivity of water in Nafion. As was shown in the paper, a smooth diffusivity can be obtained if the dependence of water content is carefully modeled in both the description of the sorption isotherm and self-diffusivity. Based on the Brunauer-Emmett-Teller finite layer sorption isotherm fitted by Thampan et al. [91] and the self-diffusivity model by Zhao et al. [118] a new Fickian diffusivity model was derived. To this diffusivity model, the following equation was fitted

using a least-square optimization procedure:

$$D_{H_2O} = 5.39e^{-2}\left(1.0 + 2.7e^{-3}\lambda^2\right)\left[1.0 + \tanh\left(\frac{\lambda - \lambda_{tp}}{\delta_{ti}}\right)\right]\exp\left(\frac{-3343}{T}\right)$$
$$(3.16)$$

where $\lambda_{tp} = 2.6225$ is an transition point and $\delta_{ti} = 0.8758$ denotes the width of the transition interval. Equation 3.16 instead of a peak exhibits a similar trend as seen for the ion conductivity, as it is depicted in figure 3.4. Again, around a water content of 2 a sudden increase is seen, reflecting that the hydrophilic clusters are gradually becoming more and more interconnected. This sudden increase is then followed by a low second order change with water content depending on the extent of membrane swelling. Theoretically, it seems more probable that the diffusivity of water would reflect the same tendency as the ion conductivity rather then exhibiting a local maxima.

In the case that methanol is added to a water hydrated membrane, the diffusivity of water is not significantly affected, as shown by Hallberg et al. [34]. Thus, equation 3.16 can directly be used for DMFC modeling. Moreover, Hallberg et al. [34] showed that the diffusivity of methanol shows a linear increase with methanol molar fraction relative to the diffusivity of water, as expressed with the following equation:

$$D_{\text{CH}_3\text{OH},a} = D_{\text{H}_2\text{O},a}\left(0.45 + X_{\text{CH}_3\text{OH}}\right) \qquad (3.17)$$

It is assumed that equation 3.17 is valid for partially hydrated Nafion membranes as well.

# Chapter 4

# Numerical Implementation and its Challenges

*In this chapter the numerical approach taken in CFX for solving the mathematical model is outlined and discussed in regard to the challenges of DMFC modeling. Emphasis is on the coupling between phase volume fraction, velocity, pressure and the source term formulation. Hereafter, various relaxation methodologies for obtaining convergence are presented particularly in regard to porous media two-phase flow. Finally, the ability of the present model for carrying out performance validation and parameter studies is discussed.*

## 4.1 The CFX Solver

The governing transport equations described in chapter 2 and 3 are solved in CFX by an element based finite volume approach. In this method each equation is dicretized spatially over the volume occupied by the DMFC using a mesh. This mesh consists of nodes around which control volumes are formed, as illustrated in figure 4.1.

By integrating the general transport equation over each of these control volumes and further applying Gauss's Divergence theorem for converting volume integrals of the divergence and gradient term into surface integrals, the following discretized two-fluid transport equation can be derived:

$$\sum_{ip} \left( \varepsilon s_\alpha \rho U_j \Delta n_j \right)_{ip} \psi_{ip} = \sum_{ip} \left( \varepsilon s_\alpha \Gamma_{eff} \frac{\partial \psi}{\partial x_j} \Delta n_j \right)_{ip} + \overline{S} V \qquad (4.1)$$

where *ip* refers to integration point, $\Delta n_j$ is the discrete outward surface
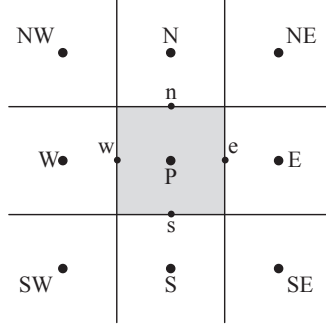
**Figure 4.1:**  Grid point illustration, where capital letters signify nodal points, small letters integration points and the gray area the control volume

vector and $\overline{S}$ represents a generalized source term which may be a non-linear function of the dependent variable $\psi$. This preliminary form of the finite volume approach is not yet applicable for being solved, additional discretization schemes are necessary to rewrite individual terms as a function of nodal points rather then integration points. In CFX field quantities at integration points are evaluated using finite element based shape functions. These shape functions can further be used for expressing gradients. When all terms have been rewritten in terms of a discrete nodal point $P$ and their neighboring nodal points $i$, the following algebraic equation is given:

$$\sum_{nb} a_i \psi_p - \sum_{nb} a_i \psi_i = \overline{S}\Delta V \tag{4.2}$$

In order to solve equation 4.2 as a set of linear algebraic equations, the generalized source term has to be written in linear form [73]:

$$\overline{S} = S_C + S_p \psi_P \tag{4.3}$$

where $S_C$ denotes a constant source term, $S_P$ a linear coefficient and $\psi_P$ the solution variable, respectively. As discussed by Patankar [73], convergence can only be guaranteed if the linear coefficient $\phi_P$ is restricted to being non-positive. A popular approach for enhancing the convergence rate of equation 4.3 is to rewrite it in terms of a truncated first order Taylor series based on the previous iteration step as shown in the following equation [67]:

$$\overline{S} = \underbrace{S^* - \left(\frac{\partial S}{\partial \psi}\right)^* \psi_P^*}_{S_C} + \underbrace{\left(\frac{\partial S}{\partial \psi}\right)^* \psi_P}_{S_P} \tag{4.4}$$

where $*$ marks the previous iteration step. The resulting constant source term $S_C$ and the linear coefficient $S_P$ are now evaluated based on information of the previous iteration step. It should be noted that this approach does not affect the resulting solution, it merely affects the "road" the solver takes towards convergence. The importance of doing a proper linearization cannot be stressed enough. Not doing this can cause immediate divergence or an extremely slow convergence rate. The importance of this in DMFC modeling is discussed in section 4.3.

Upon inserting equation 4.3 into equation 4.2 the following discretized linear algebraic equation can be derived in the general case:

$$\underbrace{\left(\sum_{nb} a_i - S_P \Delta V\right)}_{a_P} \psi_P - \sum_{nb} a_i \psi_i = \underbrace{S_C \Delta V}_{b} \qquad (4.5)$$

However, in the specific case of discretizing the mass and momentum conservation equation an additional coupling is introduced between pressure and velocity. The approach taken in CFX for dealing with this coupling is based on a co-located grid. In a co-located grid, pressures and velocities are evaluated at nodal points, rather than integration points. Unfortunately, this formulation can lead to what is known as a "checkerboard" pressure field where neighboring pressure nodes become decoupled from each other. This then causes an unphysical phenomenon where the pressure field can oscillates spatially. In order to solve this, CFX uses the Rhie-Chow interpolation scheme. In this scheme velocities at integration points are interpolated based on velocities at the nodal points by applying a momentum like equation:

$$U_{ip} = \overline{U}_{ip} + f_{ip} \underbrace{\left[\left(\frac{\partial p}{\partial x_i} - S_i\right)_{ip} - \left(\overline{\frac{\partial p}{\partial x_i}} - \overline{S}_i\right)_{ip}\right]}_{\text{Redistribution term}} - c_{ip} f_{ip} \left(U_{ip}^* - \overline{U}_{ip}^*\right) \quad (4.6)$$

where overbars indicate averages between nodal points. In the presented form of Rhie-Chow's interpolation scheme the momentum source terms have been included in a pressure redistribution term. This is done to reduce a spurious velocity field when the pressure gradient has to balance body forces, such as buoyancy, Darcy's law and the capillary pressure gradient. In DMFC this especially occurs at discontinuous interfaces between porous media or between porous media and an open channel. This subject is discussed in more detail in the section 4.3. A derivation of the Rhie-Chow interpolation

scheme as well as a more thorough discussion is found in Mencinger and Žun [58].

When applying the Rhie-Chow interpolation scheme to the two-fluid approach it leads to a coupled system where mass and momentum are solved together. Meanwhile, for solving some cases of two-phase flow it can be beneficial to include the volume fraction in the coupling. This leads to a 8x8 matrix form of the above linear algebraic equation in the following form for each nodal point and its neighboring nodes:

$$\mathbf{A}\psi = \mathbf{b}$$

where $\psi = \begin{bmatrix} U_\alpha & V_\alpha & W_\alpha & U_\beta & V_\beta & W_\beta & P & s_\beta \end{bmatrix}$.

While momentum and mass are solved in a coupled manner, the remaining transport equations, i.e. component, energy, electron, ion and dissolved species, are solved in a segregated fashion.

## 4.2   Relaxation strategies

When introducing a source term which is a non-linear function of a dependent variable, it is often not enough to linearize source terms to achieve convergence. Furthermore, it may not even be possible to do so within the confinements of the program. In CFX two strategies are used: under relaxation and false time step relaxation.

The use of under relaxation factors is often found in iterative methods for controlling the change of a variable when solving a system of equations. This can often help avoiding instabilities.

$$\psi^c = (1 - f_u)\,\psi^* + f_u\psi \tag{4.7}$$

where the superscript $c$ refers to corrected variable. In CFX under relaxation can be applied to additional variables and in consecutive iterations. However, often under relaxation is not an efficient way of stabilizing convergence. A more efficient way of avoiding divergence is false time step relaxation. The false time step is a relaxation methodology based on modifying the finite-volume equations by adding an additional, pseudo-transient term:

$$\varepsilon s_\alpha \rho \frac{\psi - \psi^*}{\Delta t} \tag{4.8}$$

where $\rho$ is mass per cell volume and $\Delta t$ is the false time step. A large time step is similar to a loose relaxation, and vice versa for a small time step.

The methodology can be physically interpreted as a way of slowing down changes in time. Unfortunately, this time step is dependent on particular phenomena and hence requires experience to be correctly assessed. For example, running a DMFC model at different current densities may require completely different degrees of relaxation time steps since the resulting mass fluxes may vary substantially. Moreover, different processes have different time scales, e.g. convection, reactions and heat transfer.

It should be noted that a local false time step can be introduced within a domain by simply inserting a zero valued source term and then setting its derivative equal to the following:

$$\frac{\partial S}{\partial \psi} = \frac{\varepsilon s_\alpha \rho}{\Delta t_l} \tag{4.9}$$

where $\Delta t_l$ denotes a local false time step. This option can be taken in domains with large property variations.

## 4.3 Sources of Divergence and their Mitigation

In the context of DMFC modeling four sources of divergence have been identified. These are: (1) Darcy's law for two-phase flow, (2) the capillary pressure gradient, (3) large mass sink and sources due to phase change or sorption-desorption in the CL, and (4) the order in which the individual transport equations converge.

### 4.3.1 Darcy's Law and Capillary Pressure Gradient

In porous media Darcy's law and the capillary pressure gradient dominate the momentum equation. In fact equation 2.29 could simply be rewritten in the following form for the liquid phase:

$$\nabla p_g + \nabla p_{cap} = \frac{\varepsilon \mu}{s_l^3} \overline{\mathbf{K}}^{-1} \mathbf{U}_l \tag{4.10}$$

where $k_{rel} = s^4$ is specified. Meanwhile, when introducing Darcy's law and the capillary pressure gradient in CFX it has to be put into the conventional form of the finite volume approach. This leads to the following source term for the liquid phase:

$$\mathbf{S} = \nabla p_c - \frac{\varepsilon \mu}{s_l^3} \overline{\mathbf{K}}^{-1} \mathbf{U}_l \tag{4.11}$$

where $\nabla p_c$ is calculated in CFX by defining the capillary pressure $p_c$ as an additional variable and then calculating its gradient in a post iterative step. Unfortunately, CFX only allows for the linearization of a momentum source term with respect to velocity, hence ignoring the importance of the liquid volume fraction. This turns out to be a critical issue. If equation 4.11 only becomes linearized with respect to velocity the solver diverges immediately. This is rather unfortunate, since it would be fairly easy to linearize it with respect to liquid volume fraction, even though the gradient of the capillary pressure is calculated numerically by the solver. By employing Clairaut's theorem about symmetry of the second order partial derivative of a multi-variable continuous function, the linearized capillary pressure gradient with respect to liquid volume fraction could simply be obtained by differentiating the capillary pressure by the liquid volume fraction before numerically calculating its spatial derivatives.

Meanwhile, it turns out that a significant improvement can still be obtained by adding instead a term based on the derivative of the capillary pressure with respect to liquid volume fraction. This term then works as a local false time step, as shown in the following:

$$\frac{\partial \mathbf{S}}{\partial U} = -\frac{\varepsilon \mu}{s_l^3}\overline{\mathbf{K}}^{-1} - \underbrace{\sqrt{\frac{\varepsilon s_l \rho \left|\nabla\left(\frac{\partial P_c}{\partial s_l}\right)\right|}{l_{P_c}}}}_{\text{local false time step}} \tag{4.12}$$

where $l_{P_c}$ is the characteristic length scale of the capillary pressure relaxation. Unfortunately, this approach is only sufficient in itself at low liquid phase volume fractions and for small discontinuous jumps in material properties at the interfaces between porous media.

The decreasing stability with increasing liquid phase volume fraction is a reflection of the change in relative permeability. At low volume fractions the transport resistance is significantly higher due its power law dependence on volume fraction. The larger the resistance relative to the capillary pressure gradient, the higher the stability. Moreover, the same condition applies in the opposite case where the capillary pressure gradient is added to the momentum equation of the gas phase and the solver calculates the liquid phase pressure directly. Then an increased stability is observed at low gas volume fractions. However, since the viscosity of the liquid phase is ten times larger and equivalently the Darcy resistance, the stability decreases more rapidly. An option for balancing these two cases is to let the solver calculate a mixture pressure based on the mobility of each phase, similarly

as the multiphase mixture model, by expressing the individual pressures relative to the mixture and capillary pressure as follows [97]:

$$\nabla p_m = \lambda_l \nabla p_l + \lambda_g \nabla p_g \tag{4.13}$$

$$\nabla p_g = \nabla p_m - \lambda_l \nabla p_c \tag{4.14}$$

$$\nabla p_l = \nabla p_m + \lambda_g \nabla p_c \tag{4.15}$$

Unfortunately, this formulation only improves stability of the solver slightly at intermediate volume fractions, and it introduces the need for a post processing step for recalculating the original pressures.

The problem of decreasing stability of the solver when the transport resistance decreases is likewise encountered for the build-in drag model. If drag forces become too small relative to other forces, the solver becomes less stable [2]. In the end to counteract this effect, it was found that introducing a local false time step in the continuity equation with respect to volume fraction was most helpful. The following empirical correlation results in stabilization over a wide range of volume fractions:

$$\Delta t_l = \max \left( \exp \left[ -1.535 e^1 s_l \right], \, 5.0 e^{-6} \right) \tag{4.16}$$

Unfortunately, the increased stability by equation 4.16 is obtained at the expense of a significantly reduced convergence rate.

The other instability observed at the interfaces between porous media can be traced back to the change in porous media properties. This partly creates a discontinuous jump in the interfacial drag force and partly in a discontinuous jump in the liquid volume fraction due to the capillary pressure gradient. As pointed out above, a discontinuous body force is an unwanted circumstance, as it can lead to velocity wiggles due to the Rhie-Chow interpolation scheme even though the momentum source term is redistributed. Moreover, as velocities are directly coupled to volume fraction this additionally leads to wiggles in the volume fraction field. This then creates a positive feed back loop where wiggles in both fields enhance each other. For a single domain formulation the simplest and most efficient way to avoid these wiggles is to remove the discontinuity by smearing out the individual components of the capillary pressure gradient and Darcy's law. Moreover, applying a smearing function to the porosity, permeability and hydrophilic pore fraction leads to a continuous volume fraction distribution across the interface as seen from equation 4.17:

$$\nabla p_{cap} \quad = \quad \nabla \left( \sigma \cos \theta \left( \frac{\varepsilon}{K} \right)^{\frac{1}{2}} \right) J\left(S\right) + \frac{dP_{cap}}{dS} \left( \frac{dS}{ds_l} \nabla s_l + \frac{s-1}{\left(1-f_{Hi}\right)^2} \nabla f_{Hi} \right) \quad (4.17)$$

Indeed, making the volume fraction distribution continuous increases solver stability and the quality of the solution. However, it may be appropriate to discuss the physical foundation of the applied smearing technique at the CL-MPL and MPL-GDL interfaces. From a "real-life" point of view, it can be argued whether a completely discontinuous interface actually occurs; more often than not it spans a thickness of up till 10-40 $\mu$m, especially at the MPL-GDL interface. In fact, on an average basis it would more probably exhibit a transitional regime where porosity, tortuosity, permeability and the hydrophilic pore fraction gradually change.

In this work the interface smearing was carried out using a hyperbolic tangent function:

$$f\left(y\right) = \frac{1}{2} \left( 1 + \tanh \left( \frac{y - y_0}{\delta} \right) \right) \tag{4.18}$$

where $\delta$ denotes the width of the smoothing interval and $y_0$ is the position of the interface. The width of the smoothing interval depends on the magnitude of the discontinuity. The smaller it is, the smaller the smoothing interval. However, for thin layers with large discontinuities this approach can become questionable, since the smearing interval may approach the layer thickness. This may become a concern when modeling the interface between the MPL and GDL.

Furthermore, it should be pointed out that CFX possesses different averaging schemes for calculating body forces at integration points, however these were found insufficient in handling the discontinuities imposed.

### 4.3.2   Phase Change and Sorption-Desorption

The introduction of large sink and source terms in the continuity equation due to phase change and sorption-desorption, increases the need of the component equation for false time step relaxation. The extent of this depends on the rate of mass transfer. The higher the rate, the lower the false time step. Moreover, often a distinction has to be made between different porous media because of their individual phase change rates. As the phase change rate is directly coupled to the specific pore surface area and the liquid volume fraction, significant difference may appear within a DMFC. Hence, a local false time steps should be used in the following range $\triangle t \in \left[1.0e^{-4}\,\text{s},\ 1.0e^{-3}\,\text{s}\right]$.

### 4.3.3  The Order in which Equations Converge

A problem with applying a very low local volume fraction time step in a single transport equation is that everything else converges quicker. This can have tremendous impact on the path the solver takes towards the final solution. In fact, it may force the solver to take a long detour. A scenario which was often encountered in this work was that all methanol in the anode CL would become consumed and then afterward refilled, because the volume distribution and velocity distribution would converge much slower. Unfortunately, in order to avoid this it was necessary to lower the false time step of each component equation. This additionally increases convergence time.

## 4.4  Convergence Time

With the implemented strategies for improving stability, a simulation time of 4-6 weeks was found for a three-dimensional, single-channel DMFC model consisting of approximately 50.000 nodes. Convergence was obtained after approximately 80.000 iterations on the Linux-cluster at the Department of Energy Technology. Convergence was defined as the point were mass, momentum and energy imbalances reached zero. Thus, at the present time convergence must be considered to slow practical applications such as a multi-dimensional validation or parameter study. Moreover, often convergence was only obtained while carefully selecting a specific set of local false time steps and capillary pressure length scales. If only a few parameters were changed often new relaxation parameters were needed to avoid divergence.

# Chapter 5

# Results and Discussion

*In this chapter the main contributions of this work are presented and discussed in relation to the stated project objectives. These contributions comprise of the findings made in the parameter assessment, in-situ DMFC measurements as well as the published modeling results from the collection of papers. The chapter content is outlined as follows: After some introductory remarks, the experimental work is presented and discussed. To facilitate an overview of the performed experiments a short description is given of the DMFC used as base case in the experimental work. This section is followed by the obtained modeling parameters used in final DMFC model and in-situ measurements comprising of polarization curves and methanol crossover. The methanol crossover measurements are the ones presented in Paper 5. Subsequently, the modeling results obtained throughout this work are presented and discussed. These are split into three topics: inhomogeneous GDL compression, membrane transport and the complete DMFC model including a partial validation. The first topic is solely based on Paper 1, the second is based on Paper 2 and 3, while the third again solely is based on Paper 2.*

## 5.1   Introductory Remarks

The intended outcome of the experimental work was in part to minimize the number of uncertain parameters in the final DMFC model and in part to enable a complete multi-variable validation of it. However, at the present moment, the latter is not realizable due to slow convergence, as discussed in chapter 4. Thus, model validation is confined to base case conditions. Despite the limited usefulness of the experimental measurements at the present moment, the obtained results are still presented and discussed, as they may

be applicable in future validation studies.

With respect to the obtained modeling results found in the collection of papers, a short explanation may be appropriate for ease of reading in the following sections. Throughout this work different studies have been carried out to elucidate modeling capabilities of the developed model, to investigate the importance of certain transport phenomena encountered during operation or to stress the importance of various modeling assumptions. In the collection of papers this led to three modeling studies. In Paper 1 a preliminary half-cell cathode model was used for investigating the importance of inhomogeneous GDL compression on liquid volume fraction and oxygen transport, while accounting for detailed two-phase phenomena. This work, amongst others, underlined the ability of the code to capture discontinuities in the liquid volume fraction in three dimensions. In Paper 2 a complete DMFC model was presented. In this study emphasis was on the interaction between anode GDL volume porosity and the assumption of the capillary pressure boundary condition at the anode GDL-channel interface. As opposed to Paper 1, inhomogeneous compression was ignored to more clearly stress phenomena due to volume porosity and variations in surface tension. In Paper 3 the impact of water diffusion model on the predicted water flux and distribution across Nafion was investigated. Especially the reported existence of a local maximum in the diffusivity of water was investigated from derivation to application. This was done in conjunction with changing sorption-desorption phenomena and to underline their interaction as well as importance on the transport behavior of water.

## 5.2 Experimental Work

### 5.2.1 DMFC Description

The DMFC used in the experiments covers an active area of 180 cm$^2$. The anode CL is made of 80 wt% catalyst material (i.e. 62 wt% Pt-Ru on Ketjen Black EC600) and 20 wt% electrolyte material (i.e. Nafion DE521). The cathode CL consists of 85 wt% catalyst material (i.e. Cabot 65 wt% Pt on Ketjen Black EC600) and 15 wt% electrolyte material (i.e. Nafion DE521). Both the anode and cathode catalyst inks are sprayed on top of a SGL-35DC gas diffusion layer. This type of GDL contains 20 vol% PTFE and an adjacent MPL. Nafion 115 was used as electrolyte.

As base case, graphite bipolar plates with a combined serpentine and parallel channel configuration were used, as shown in figure 5.1. The number
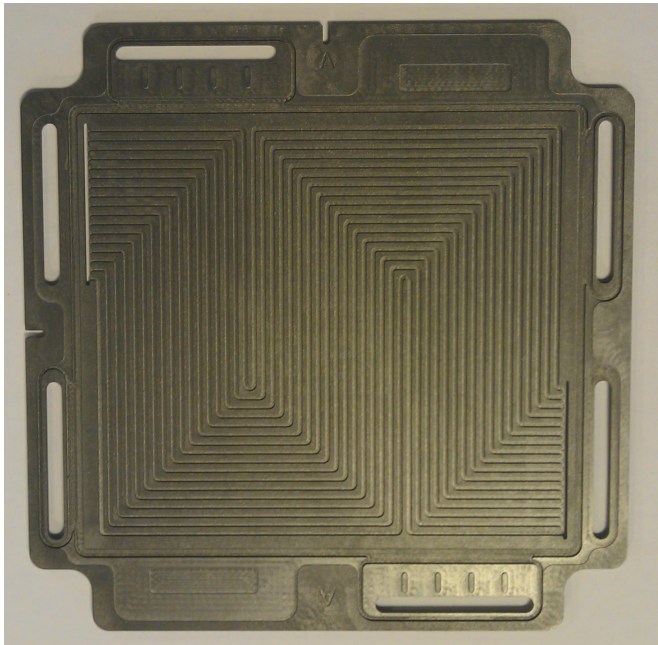
**Figure 5.1:** The bipolar plate used as base case in the experimental measurements

of channels is 25 and the channel length is 14 cm. The channels and ribs have a width of 1.05 mm and 0.85 mm, respectively, which is equivalent to an OR of 0.57. The channel and rib height is 0.65 mm.

### 5.2.2 Parameter Assessment

In regard to modeling capillary pressure forces and Darcy's law, it is important to know the degree of porosity and permeability associated with the different layers. Likewise, it is important to know the exact dimensions of each layer because transport resistances scale with them. Moreover, it is important to know the ionomer content in the CL in order to describe ion conductivity and dissolved species transport. The measured porosities, Nafion volume fractions in the CLs, permeabilities and dimensions are listed in table 5.1. In the following, measured porosities, Nafion volume fractions in the CL and permeabilities are discussed along with brief elaboration on the measurement technique employed.

| Parameter | Region | Symbol | Value | Unit |
|-----------|--------|--------|-------|------|
| Porosity |  |  |  | $m^3/\ m^3$ |
|  | ACL |  | 0.71 (0.76) |  |
|  | CCL |  | 0.83 (0.86) |  |
|  | MPL |  | 0.55 |  |
|  | GDL |  | 0.88 |  |
| Nafion Volume Fraction |  |  |  | $m^3/\ m^3$ |
|  | ACL |  | 0.0877 |  |
|  | CCL |  | 0.0439 |  |
| Permeability |  |  |  | $m^2$ |
|  | ACL |  | 1.32e-14 |  |
|  | CCL |  | 2.66e-14 |  |
|  | MPL |  | 9.65e-14 |  |
|  | GDL |  | 3.1e-11 |  |
| Thickness |  |  |  | $\mu m$ |
|  | ACL |  | 40 |  |
|  | CCL |  | 40 |  |
|  | MPL |  | 70 |  |
|  | GDL |  | 250 |  |

**Table 5.1:** Structural parameters of a commercial DMFC electrode from IRD Fuel Cell A/S

**Porosity**

The porosity of each layer was calculated based on the solid phase density and volume of each layer. The solid phase density was measured using Archimedes principle. This is done by filling the open pore space of a porous medium with a low surface tension liquid and then weighing it under buoyancy. This approach can also be applied to porous layer assemblies that are commercially available. Applying this methodology to the DMFC electrodes from IRD Fuel Cell A/S leads to the porosities shown in table 5.1.

The GDL and MPL porosities are as one would expect. It is high for GDL in order to obtain a good gas distribution, and it is low for the MPL in order to obtain larger capillary forces. Moreover, the porosity obtained for the GDL is in good agreement with the porosity claimed by SGL. With regard to CL a difference is observed for the anode and cathode. This difference is due to the composition of the electro-catalyst and the amount of carbon and Nafion used. The porosities shown in parentheses are estimated values based

on mass loading specifications, i.e. the mass fraction of ionomer, carbon and electro-catalyst.

It should be noted that such a high CL porosity may increase gas flow, but also increase the tortuosity of electron and ion transport as well as dissolved methanol and water transport, and hence leads to an efficiency reduction.

**Nafion Volume Fraction**

Based on the measured CL density, obtained in the porosity experiments, it is possible to calculate the Nafion volume fraction of the CL. As seen from table 5.1, the obtained values for each CL are only a few percentage. This entails a low effective ion conductivity as well as a low methanol and water diffusivity in the CL. This is not necessarily an unfavorable condition. While it implies a high ohmic loss due to poor ion conductivity, it also implies a low methanol crossover rate. As long as it is more important to reduce methanol crossover than achieving a high ion conductivity this may be a favorable condition.

**Viscous permeability**

The through-plane permeability of each layer was determined by fitting a Darcy-Forchheimers equation to pressure losses measured over a series of layer configurations: GDL (SGL 35DA), GDL-MPL assembly (SGL 35DC) and the full electrode assembly (SGL 35DC + CL). The resulting through-plane permeabilities are shown in table 5.1.

Even though the porosity of each CL is higher than that of the MPL, their permeabilities are nearly an order of magnitude greater. This implies that the porous structure of the CL is much more convoluted and subject to much smaller pores. When comparing the MPL and GDL a difference of two orders of magnitude can be seen. As discussed earlier, this has a significant impact on the difference in capillary pressure and thereby resulting saturation jump condition between the MPL and GDL.

## 5.2.3 Polarization Curves

In figure 5.3, 5.4 and 5.5 polarization curves are depicted as function of average cell temperature, methanol inlet concentration and the open ratio of flow channels, respectively. With regard to the latter polarization curves, it must be emphasized that in order to keep the two-phase flow morphology
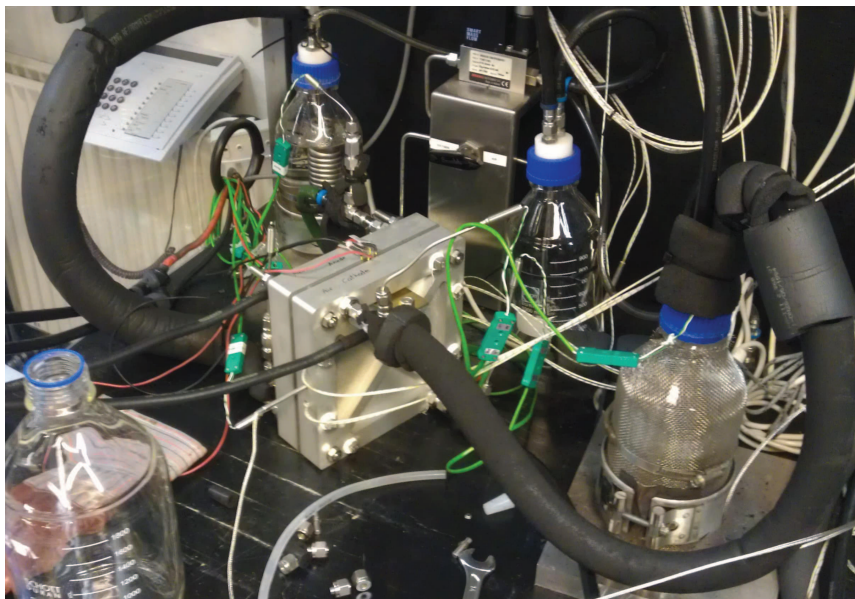
**Figure 5.2:** Fuel cell setup during operation

similar, the Reynolds, Eötvös and Froude number as well as pressure loss are kept nearly constant. This was achieved by fixing the hydraulic diameter and channel length, while balancing channel width and height as well as the number of channels and the number of bends.

In figure 5.2, the experimental setup is shown. During operation a methanol solution based on demineralized water, was pumped into the anode channels using a peristaltic pump. The cathode was operated on atmospheric air, which was pumped in using a flow meter controlled gas pump. Both inlet streams are initially preheated; the methanol solution through a heat exchanger set to an outlet temperature of 60 °C, and the inlet gas through a bubble column set to an outlet temperature of 40 °C. To secure an even and fixed temperature distribution independent of the current drawn, additional heaters are placed in metal plates adjacent to the bipolar plates. These plates are kept at a constant temperature using a switch board. At base conditions the cell is operated at 75 °C .

Each polarization curve was obtained under constant volume flow conditions. This was done as opposed to constant stoichiometry operation to avoid excessive temperature fluctuations and hereby sudden changes in the voltage output. Thus by running at constant flow the reproducibility is improved. It should however be noted that constant volume flow often leads to

increased temperature gradients due to larger variations between the inlet to outlet temperatures. Another effect as discussed in chapter 2 is the effect on two-phase flow patterns. For the anode a constant volume flow results in a higher liquid phase superficial velocity and lower gas volume fraction at lower current densities and hence more bubbly flow. For the cathode this gives rise to a higher superficial gas velocity at low current densities and hence less droplet and slug flow formation and more mist flow. Meanwhile, the highest performance is actually observed when running near an air and methanol stoichiometry of 6 and 3, respectively. The polarization curves should therefore not be seen as indicators of performance, but more as reflections of a given set of operation conditions and their impact on transport phenomena.

When studying figure 5.3 a clear tendency is observed. Increasing methanol concentration decreases cell voltage at low current densities, whereas it increases cell voltage at high current densities. The latter is seen as a significant increase in limiting current density. These observations are in accordance with the notion that increasing the inlet methanol concentration increases methanol crossover, since the driving force for diffusion increases. Moreover, the same concept applies to the limiting current density. From the three measurements it is clear that a trade-off exist between a high efficiency at low current densities and at high current densities. This is clearly depicted as the curves intersect each other at a current density around 0.25 $A/cm^2$.

While the interpretation of the methanol dependence is more straight forward, the dependence on temperature is not. The effect of the operation temperature was investigated for four different temperatures: 55°C, 65°C, 75°C and 85°C. As seen in figure 5.4 the worst performance was obtained at the temperature of 55°C over the entire current density range. At low current densities it is evident that the lower the temperature the slower the electrochemical reactions occur and the higher the overpotential voltage has to be. This is clearly seen as the cell voltage increases with temperature in this range for all cases. Nevertheless, this tendency becomes less important at higher current densities as seen for the operation temperature of 85°C. A sudden drop is observed in cell voltage relative to the operation temperature of 65 or 75°C. This indicates that even though an improved electrochemical reaction rate as well as ion and electron conduction is obtained, performance is lost. Hence, this drop must be associated with a difference in mass transport and/or methanol crossover.

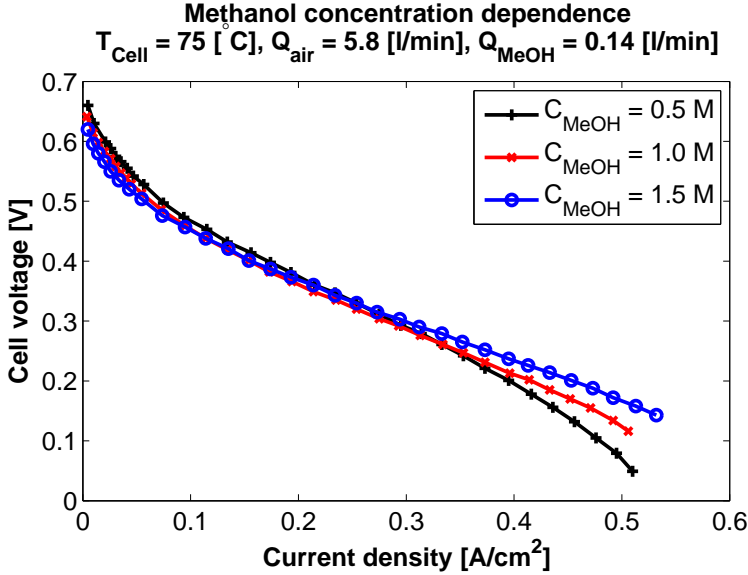With respect to mass transport losses, it can be stated that the extent

**Methanol concentration dependence**

$T_{Cell} = 75 \; [^{\circ}C]$, $Q_{air} = 5.8 \; [l/min]$, $Q_{MeOH} = 0.14 \; [l/min]$



**Figure 5.3:** Polarization curves for various methanol concentrations at constant inlet volume flow

of methanol evaporation and the hereby removal of methanol by gas outflow would have to increase more than the extent of methanol diffusivity towards the CL. However, it is more likely that this decrease in performance is primarily due to an increase in methanol crossover. As shown by Jiang and Chu [43], a significant increase in methanol crossover is observed when increasing the temperature from 55 to 85 °C. This increase is not only due to a change in diffusivity, it is also reflection of an enhancement of the methanol sorption rate and EOD.

The performance dependence on the OR was studied for three ratios: 0.34, 0.57 and 0.8. As depicted in figure 5.5 the best performance was found for a OR of 0.57. Both a smaller and larger OR result in a performance reduction. The same dependence on OR was observed by Yang and Zhao [106] for single channel serpentine flow fields. As discussed by Yang and Zhao [106], the OR can be interpreted as the effective contact area between fluid flow in the channel and the GDL. This implies that an increase in OR leads to an improved methanol distribution across the electrode at the expense of a more severe methanol crossover rate and a higher electrical contact resistance, whereas a decrease in OR causes less methanol crossover and less contact resistance at the expense of a more non-uniform methanol
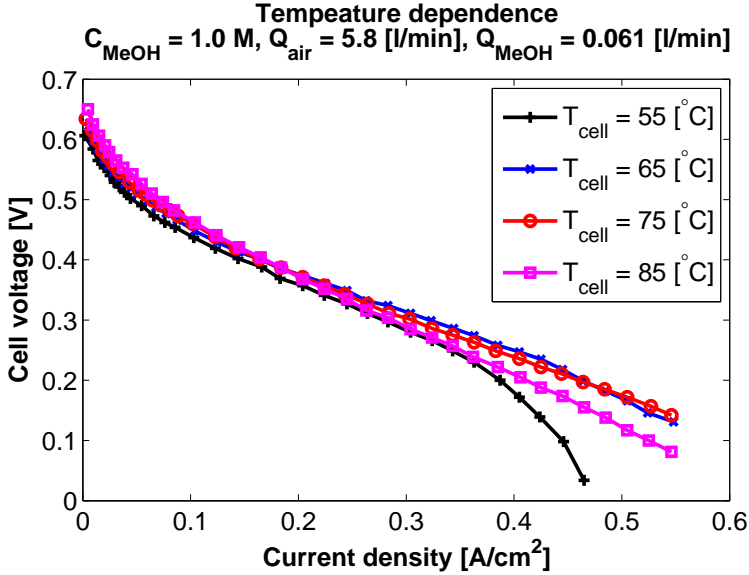
**Figure 5.4:** Polarization curves for various temperatures at constant inlet volume flow

distribution and more pronounced mass transport losses.

Although this line of reasoning explains the observed difference it is a bit too simplified, as it ignores the effect of the applied clamping pressure during preparation and the resulting inhomogeneous compression of the GDL as well as the extent of GDL-channel intrusion. While a low OR leads to an even GDL compression and a small extent of GDL-channel intrusion, a high OR leads to the exact opposite. As discussed in Paper 1, this difference affects two-phase flow and species transport. The higher the OR, the higher the transport resistance becomes under the land and in the channel. Moreover, it further reduces the extent of contact resistance, since the effective pressure becomes higher under the land. Consequently, a counteracting effect is observed from applying the clamping pressure during preparation.

### 5.2.4 Methanol Crossover

In order to measure methanol crossover instantaneously during operation, a simple, yet effective technique was developed in this work. By combining the anode and cathode outflow, condensing out all water and methanol and measuring the combined carbon dioxide mole fraction as well as assuming a nearly complete reaction of reactants to form carbon dioxide and water,
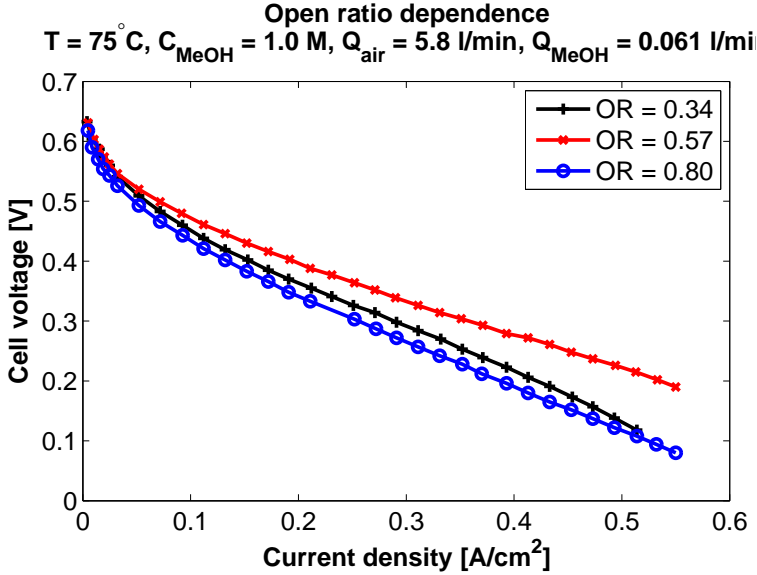
**Open ratio dependence**

T = 75 °C, $C_{MeOH}$ = 1.0 M, $Q_{air}$ = 5.8 l/min, $Q_{MeOH}$ = 0.061 l/mi



**Figure 5.5:** Polarization curves for various open ratios at constant inlet volume flow

methanol crossover could be calculated.

In figure 5.6 and 5.7, the resulting parasitic current density and Faradaic efficiency (i.e. fuel utilization efficiency) are depicted as a function of reactant stoichiometry and cell current density. In both figures a clear trend can be observed; increasing current density decreases methanol crossover and increases the Faradaic efficiency of the cell. This tendency is a reflection of the interaction between membrane transport phenomena and the decreasing methanol concentration in the CL due to mass transport resistances in the GDL and MPL.

In general, the transport of methanol through the membrane depicts two regimes as a function of current density; at low current densities it is primarily dominated by diffusion, whereas at high current densities it is primarily dominated by EOD [112]. However, the extent of this is likewise affected by the sorption/desorption rate and mass transport resistance. The sorption rate determines the available amount of methanol for transport within the electrolyte phase and mass transport resistance the available amount for sorption. Consequently, if the methanol stoichiometry increases in the channel so does the extent of methanol crossover, as seen from the data. Indeed, increasing the methanol stoichiometry for a fixed channel in-
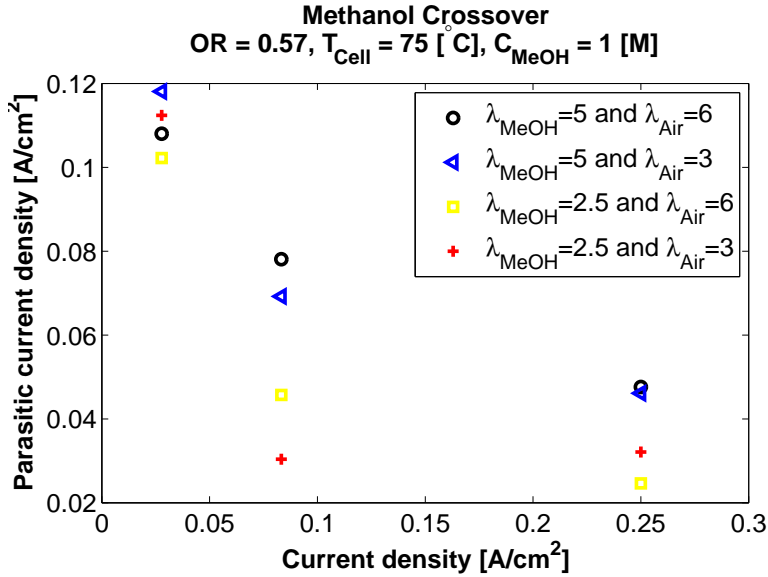
**Figure 5.6:** Parasitic current density as a function of current density and stoichiometry

let methanol concentration has to lead to a higher methanol concentration along the channel and hence a larger driving force for concentration diffusion. Moreover, increasing the stoichiometry also causes a higher liquid phase superficial velocity and accordingly a better component mixing. Likewise, it decreases the gas phase volume fraction in the channel, making gas phase blockage less distinct. Decreasing the gas volume fraction particularly assists in avoiding slug and annular flow. As discussed by Yang et al. [107], avoiding these is of great importance as they lead to a severe increase in the methanol transport resistance.

Explaining the effect of air stoichiometry on the observed methanol crossover is not as straight forward, since it does not directly affect its rate. Increasing air stoichiometry has two clear impacts. First of all, it raises the air concentration in the CL and hence lowers activation losses, whereby the effect of the mixed potential becomes less pronounced. Secondly, it lowers the relative humidity of water in the cathode electrode and hence increases the gradient for water transport across the membrane. This may lower the water content in the membrane and consequently ion conductivity, however it also increases the mass transport in the anode towards the membrane. This then further leads to a higher methanol rate as well and hence an
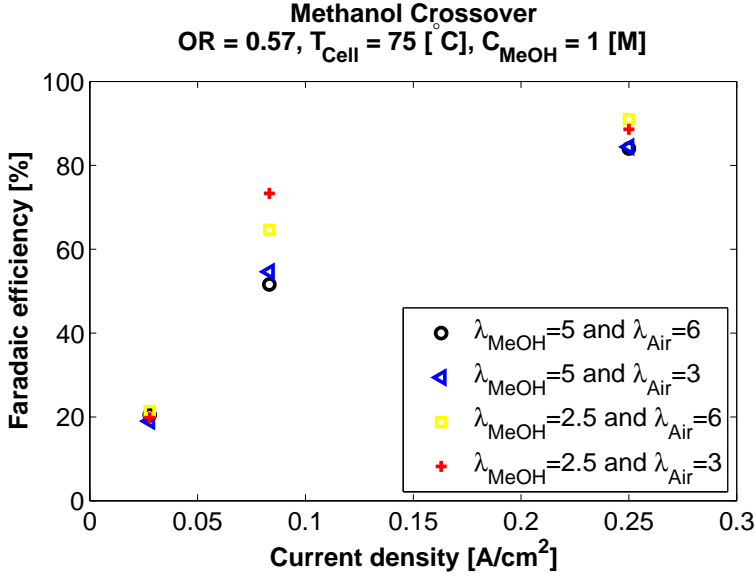
**Figure 5.7:** Faradaic efficiency as a function of current density and stoichiometry

increase in methanol crossover.

## 5.3　Modeling Work

### 5.3.1　Inhomogeneous GDL Compression

When compressing a fuel cell to avoid contact losses, the GDL primarily becomes compressed due to its low mechanical strength. As discussed above, this leads to an excessive compression of the GDL pore structure under-the-land compared to under-the-channel as well as GDL intrusion into the channel. While GDL intrusion alters the transport characteristics of the channel, under-the-land compression affects electron transport, cooling, the level of liquid phase saturation and oxygen transport; not only in the GDL, but likewise in the CL and MPL. For a completely flooded cathode this trend is clearly depicted in figure 5.8 and 5.9, respectively.

The resulted difference in the distribution of liquid phase with and without GDL compression is the result of different phenomena. A reduction in GDL thickness under the land entails a decrease in porosity and permeability and hence an increase in interfacial transport resistance according to Darcy's law. To overcome this increased transport resistance, the level of

liquid volume fraction under the land has to increase, since a higher capillary pressure gradient is required to overcome the increased transport resistance. Meanwhile, this effect on the liquid volume fraction level is to some extent counteracted by a reduction of the characteristic pore radius, since it per se implies an increase in the capillary pressure for a given liquid volume fraction according to the Leverett J function. Actually, it turns out that the predicted interfacial transport resistance always increases more than the predicted capillary pressure. A closer comparison between Darcy's law and the Leverett J function reveals that the predicted interfacial transport resistance increases as a quadratic function of the reciprocal characteristic pore radius, while the capillary pressure only does so linearly.

Altering the pore structure due to inhomogeneous compression has other implications as well. It decreases species transport in the gas phase and it changes the distribution of liquid phase due to evaporation and condensation. The former is clearly observed in figure 5.9, as a significant reduction in oxygen transport under the land. But just as the oxygen transport towards the CL is obstructed, likewise is the removal of water vapor from under the land. This implies a higher molar fraction of water vapor under the land and hence a smaller driving force for liquid phase evaporation. The consequence of this is that liquid phase flooding under the land occurs at lower current densities, since the liquid water produced in the ORR cannot be removed well enough through evaporation. Moreover, the extent of this is further affected by a better cooling under the land than under the channel. A thinner and more dense structure implies better cooling, a lower gas phase temperature and hence a lower capacity for water vapor.

In all of these considerations it is important to realize that the use of a non-equilibrium phase change model is crucial. Whereas an equilibrium model may over-predict the amount of water vapor removed, a non-equilibrium formulation more accurately accounts for the kinetics associated with molecular transport across the vapor-liquid interface. For DMFC this has a significant impact on the predicted performance, as shown by Yang and Zhao [108].

### 5.3.2   Membrane Transport

The effect of sorption-desorption was for many years neglected in PEM modeling, as it was thought that diffusion significantly dominated over interfacial
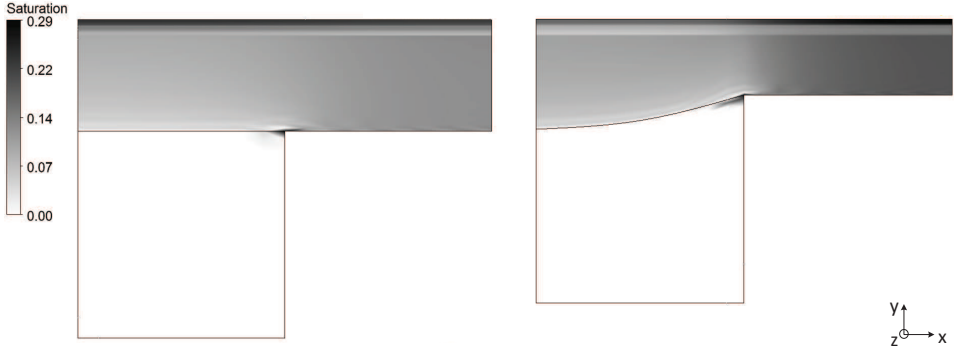
**Figure 5.8:** The liquid volume fraction (i.e. liquid saturation) distribution without compression to the left and with inhomogeneous compression to the right
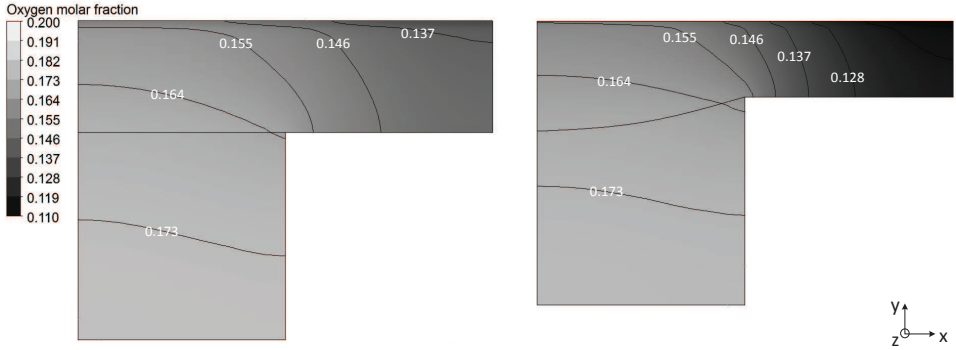


**Figure 5.9:** The oxygen molar fraction distribution without compression to the left and with inhomogeneous compression to the right

transport kinetics. However, for PEM exposed to water vapor, it was found not to be the case, even for fairly thick membranes. Indeed, it was found that interfacial transport kinetics along with membrane swelling were the source of discrepancies in the reported diffusivities in the literature [78, 54, 53]. The importance of accounting for the interaction between diffusion and interfacial transport kinetics can be seen from studying the relation between water flux and the extent of the interfacial transport rate. A way this can be achieved is by scaling the interfacial transport rate as a function of surface roughness, which is the equivalence of changing ionomer loading and hence the vapor-ionomer interfacial surface area in a CL.

In figure 5.10, the predicted water flux as function of surface roughness and diffusivity model is seen. Depending on the applied surface roughness
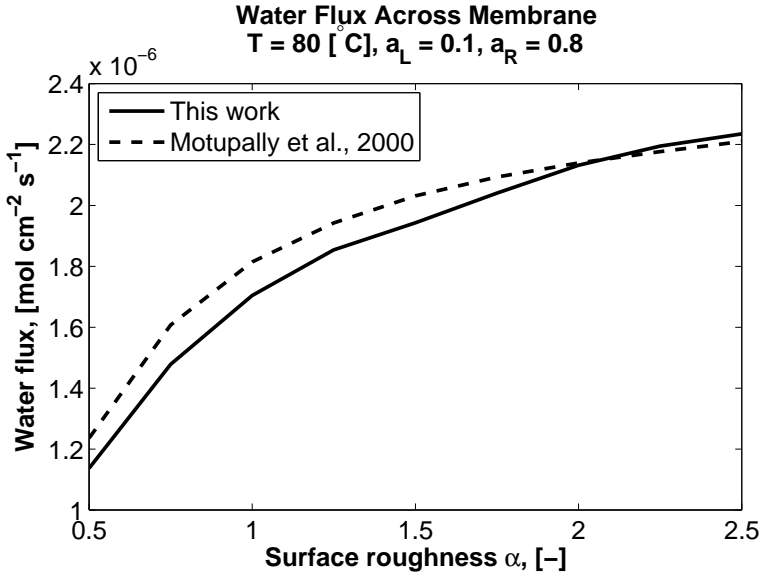
**Figure 5.10:** Membrane water flux as a function of diffusivity model and surface roughness for Nafion 1110. The left side is exposed to a relative humidity of 10 % and the right side to a relative humidity of 80 %.

and diffusivity model, variations in the predicted water flux between a factor of 2 and 4 are observed. This is especially the case for the diffusivity model derived in this work and the one by Motupally et al. [62] based on the measurements by Zawodzinski et al. [113] and the work of Springer et al. [88]. It is further apparent that merely comparing diffusivity models based on their predicted water flux is not useful, as they may overlap depending on the extent of sorption/desorption. This concern is particularly a problem when validating diffusivity models by experimental measurements of water fluxes, as seen in the literature by for example Motupally et al. [62] or Baschuk and Li [5]. Conducting such a validation requires exact knowledge of the interfacial transport characteristics of the PEM material and the experimental setup, else it is meaningless.

Moreover, the alleged observation of a spike in the Fickian diffusivity of water in Nafion cannot be verified in this manner; as it is simply not revealed. The best course of action for exposing it is to study the distribution of water across the membrane. In figure 5.11a and 5.11b, the effect of diffusivity model and surface roughness on the water content distribution and transport resistances can be seen, respectively. When comparing the
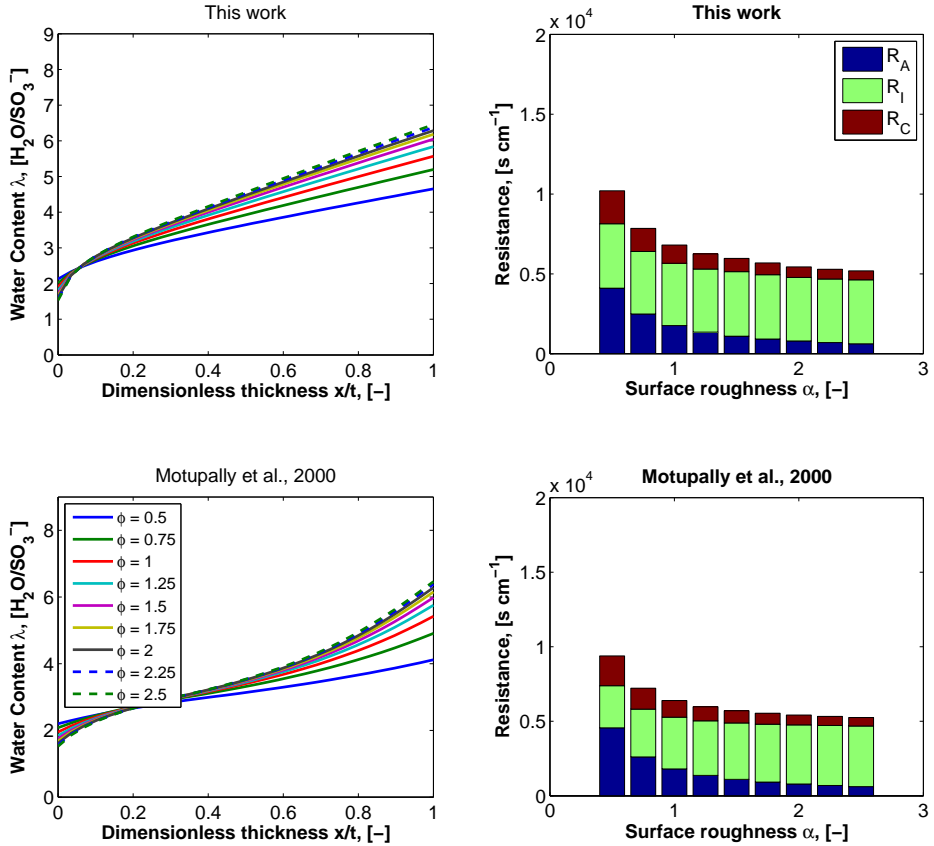
**(a)** The water content distribution in Nafion 1110 at 80°C as a function of surface roughness and diffusivity model. The anode humidity is 80 % and the cathode 0 %.

**(b)** Transport resistances for Nafion 1110 as a function of surface roughness and diffusivity model at 80°C. The anode humidity is 80 % and the cathode 0 %.

**Figure 5.11:** The effect on diffusivity model on water transport

employed diffusivity models a significant impact on water content distribution is observed. For the diffusivity model by Motupally et al. [62], a local maximum in the diffusivity is revealed as a flat water content profile around a water content of 3. This is in contrary to the diffusivity model derived in this work, which depicts a sharp round-off near the low humidity interface and an almost linear profile across the membrane. It is apparent that the characteristic shape of the water content distribution, becomes more pronounced at a higher surface roughness, since it reflects a decrease in the interfacial resistances. Indeed, the explanation for the nearly identical water fluxes, despite notable differences in water content profiles, lies in the coupling between diffusion and interfacial transport kinetics.

In comparison, the resulting water content distribution in an operating DMFC is significantly different. In part since the PEM is exposed to a two-phase mixture at the anode and in part because water transport not only occurs by diffusion, but by EOD. In figure 5.11a, an example of a resulting water content distribution is seen. Clearly, for DMFC operation the existence of a local maximum in the diffusivity of water is unimportant, as its occurrence is thought to happen around a water content of 3. Thus, the previous discussion is only relevant in the context of low humidity operation.

For DMFC operation, the correction of water transport within the CL is nearly more important than the actual diffusivity of water. Within the PEM the water content is evenly distributed, whereas a steeper gradient is observed in the CL. The latter is caused by a significantly lower effective diffusivity of water due to a more porous and convoluted structure. This is clearly seen from the low electrolyte volume fraction depicted in table 5.1. The same importance is found for the methanol diffusion, ion conductivity and EOD.

An important factor in the resulting water content profile is also the predicted liquid volume fraction in the CL. The higher the liquid volume fraction, the higher the uptake of water becomes. Because water vapor sorbs slower than liquid water, the electrolyte phase exposed to vapor works as hindrance for water sorption.
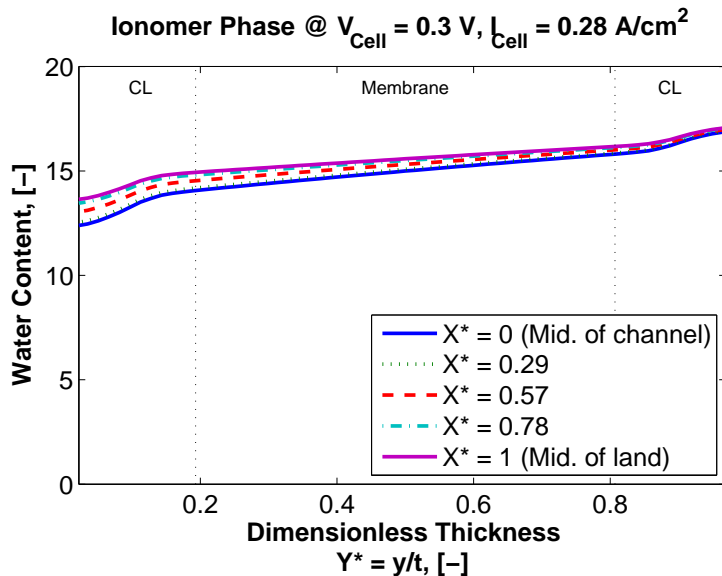
**Figure 5.12:** Membrane water content in an operation DMFC governed by two-phase sorption/desorption

### 5.3.3   Direct Methanol Fuel Cell Model

**Performance Comparison**

In figure 5.13 a partial validation of the developed DMFC model is depicted. The predicted polarization curve is in good agreement with the experimental data. At low current densities the developed model is able to capture the change in voltage overpotential loss and mixed potential caused by methanol crossover. This initial voltage gradient is dominated by a change in anode overpotential, whereas the low open circuit voltage is a reflection of the decrease in cathode overpotential due to methanol crossover. As the current density drawn increases and the ohmic region is entered, the change in voltage becomes linear. The predicted curve falls steeper than the experimental measured, thus indicating a slightly higher ohmic resistance most likely due to either contact resistance or ionic transport. While correctly estimating the contact resistance is a matter of knowing the applied force used for compressing the cell during preparation, the ionic transport loss is bounded by the water content level in Nafion. Thus, to adjust the extent of ionic losses the degree of water uptake has to be corrected. This can be accomplished by increasing the hydrophilic pore fraction in CL and consequently the frac-
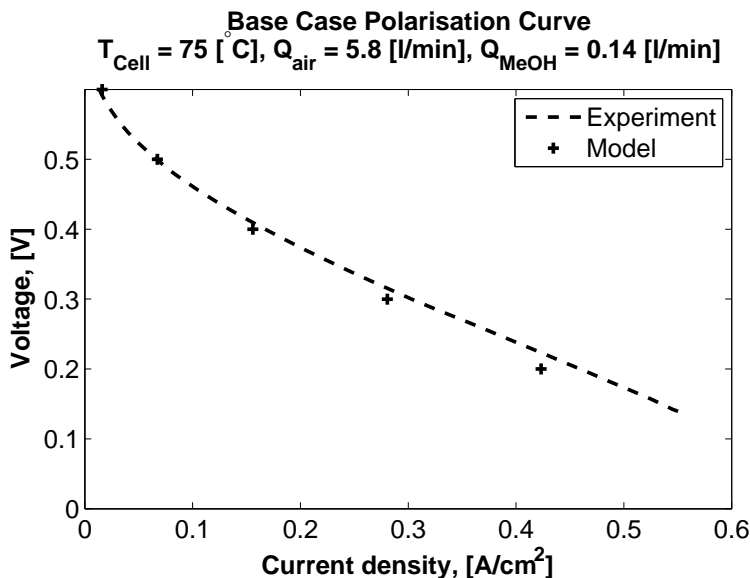
**Figure 5.13:** Polarization curve under base case conditions

tion of Nafion exposed to the liquid phase. Meanwhile, another possibility could be that the observed difference in the ohmic region instead is caused by an overestimation of the overpotential losses associated with either mass transport or the specified parameters used in the electrochemical model.

**Phase Transport**

In figure 5.14, the liquid volume fraction distribution within the anode electrode is depicted for two cases of GDL volume porosity for an average channel overpressure of 2500 Pa. When comparing the liquid volume fraction distributions in the GDL it is clear how sensitive it is to the coupling between the GDL volume porosity and the applied capillary pressure boundary condition at the GDL-channel interface. While imposing a constant liquid volume fraction of nearly one at the GDL-channel interface only allows for minor variations in liquid volume fraction distribution of the GDL, no matter the selected material properties, a constant pressure condition gives rise to a significant difference in the predicted mass transport losses. Not to mention, it gives the freedom to relate intrusion to an overpressure in the channel, rather than presuming an excessive force, which fills nearly all the hydrophobic pores.

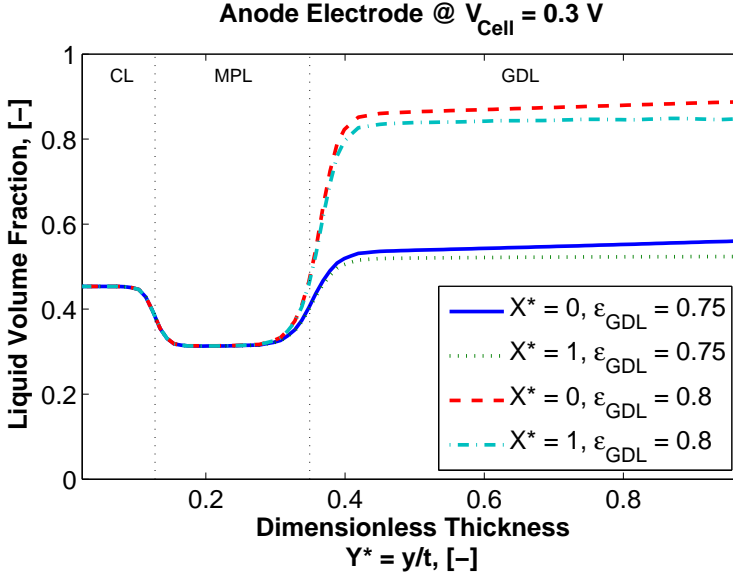In a highly flooded environment such as the anode of a DMFC it is

**Figure 5.14:** Liquid volume fraction distribution in the anode electrode for a GDL-channel capillary pressure boundary condition. A dimensionless distance of $X^* = 0$ and $X^* = 1$ are equivalent to under the channel and land, respectively.

important to realize that the distribution of a liquid to a high extent is controlled by the fraction of hydrophilic pores and the characteristic pore size. Particularly, for the CL and MPL, where micropores are found. As can be seen for both cases, the liquid volume fraction level is forced nearly equal to the hydrophilic pore fraction in the CL and MPL. This macroscopic transport phenomenon arises because the characteristic pores of the CL and MPL are nearly 100 times smaller than those found in the GDL. While the liquid volume fraction in the GDL may vary significantly depending on the pressure applied to the GDL-channel interface, the level in the CL and MPL will appear nearly constant. This further implies that the observed jump condition in liquid volume fraction at the CL-MPL interface is primarily induced by a difference in hydrophobicity, rather than a difference in characteristic pore size. A further implication is that the liquid volume fraction level will remain nearly unaffected by current density.

In DMFC modeling variations in surface tension as a function of methanol molar fraction are often neglected, as pointed out in section 2.3.4. However, by accounting for it a difference is imposed in the surface tension under the land and under the channel, since the methanol concentration is bound to
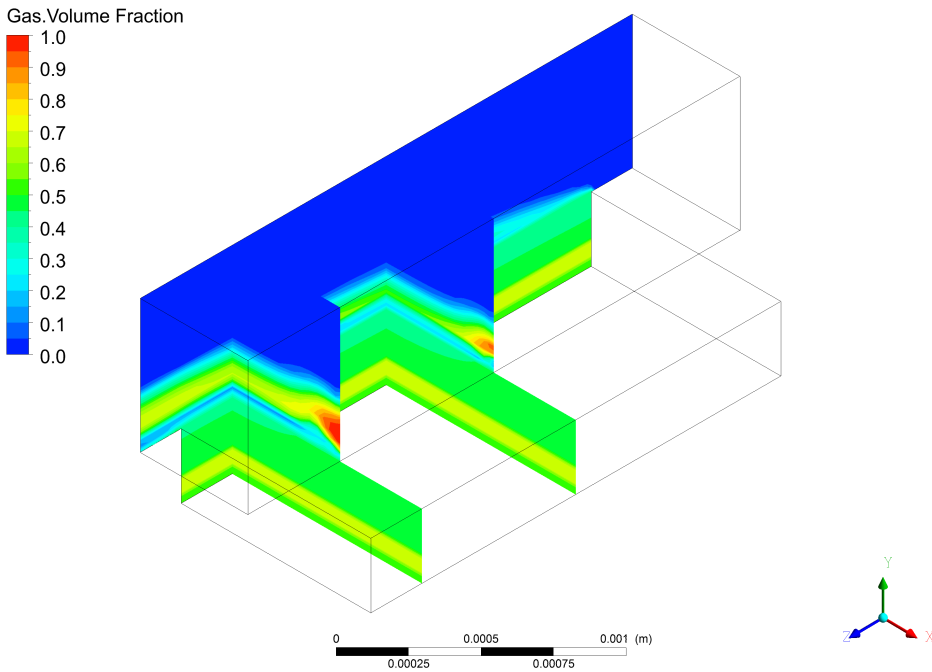
**Figure 5.15:** A three-dimensional gas volume fraction distribution in the anode channel and electrode at a GDL porosity of 0.75, cell voltage of 0.3 V and a current density of 0.17 A/cm$^2$

be higher under the channel. Moreover, this means for a continuous and flat capillary pressure distribution in the GDL, a difference is observed in the predicted liquid volume fraction under the land compared to under the channel. Indeed, since the surface tension increases with decreasing methanol concentration, the liquid volume fraction under the land decreases. Accounting for these distribution changes leads to an increase in methanol transport resistance under the land and degraded performance in the mass transport loss regime, which especially is pronounced for large characteristic pore radii and diluted methanol solutions. The former since the liquid volume fraction level is pushed away from the hydrophilic pore fraction and the latter since the surface tension is particularly non-linear in this regime.

An important reason for expanding the CFD modeling framework of DMFC to three dimensions and including channel flow is the prediction of the phase distribution in the channel and its impact on fuel transport. In figure 5.15, the gas volume fraction distribution in the anode channel and

electrode is depicted.  Along the channel length, it can be seen how the gas volume fraction gradually increases adjacent to the electrode surface. This gas layer creates an additional resistance for methanol transport in the liquid phase by obstructing it.  Because the thickness of the gas layer increases along the length of the channel, the rate of species transport in the liquid phase decreases equivalently along it.  This is especially seen in the corner of the channel, since gas produced underneath the land area has to pass this corner to enter the channel. The size and shape of the observed gas layer depends on the amount of gas outflow from the electrode and the balance between interfacial forces, as discussed in section 2.1.1. At the present moment, only dispersed gas bubble flow is assumed, hence adhesion or bubble coalescence is not accounted for.  Accounting for these effects could decrease the gas phase flow and hence increase the thickness of the layer or alter the amount of gas in the channel corner.  Besides, these phenomena are likewise dependent of the capillary pressure boundary condition.   In fact, if the interface condition was based on the actual channel overpressure, rather than an average channel overpressure as accounted for in the present moment, this would impose a change along the channel length.

**Methanol Transport**

In continuation of the previous discussion on the phase distribution it is suitable to discuss in more detail its impact on methanol distribution. In figure 5.16, the methanol concentration distributions matching the liquid volume fraction distributions previously shown in figure 5.14, are found.  For the highest porosity, where the liquid phase easier intrudes the hydrophobic pores of the GDL, a substantial higher methanol concentration is observed in the CL. The explanation for this difference lies in a decrease in the effective diffusivity of methanol in the GDL, as seen from the increased methanol concentration gradient in the through-plane and in-plane direction.  While the high porosity case leads to a current density of 0.28 A/cm$^2$, the low porosity case only results in a current density of 0.17 A/cm$^2$.  Clearly, this significant difference occurs, because the latter case nearly has reached its limiting current density and a more uneven distribution of methanol is observed across the CL.

An important factor in the resulting limiting current density is the MPL, as seen from the steep methanol concentration gradient. By default, the liquid mass transport resistance of the MPL is much higher than the one of the GDL. In part due to its lower porosity and higher tortuosity, and in part due its lower liquid volume fraction.  It is apparent that the MPL serves
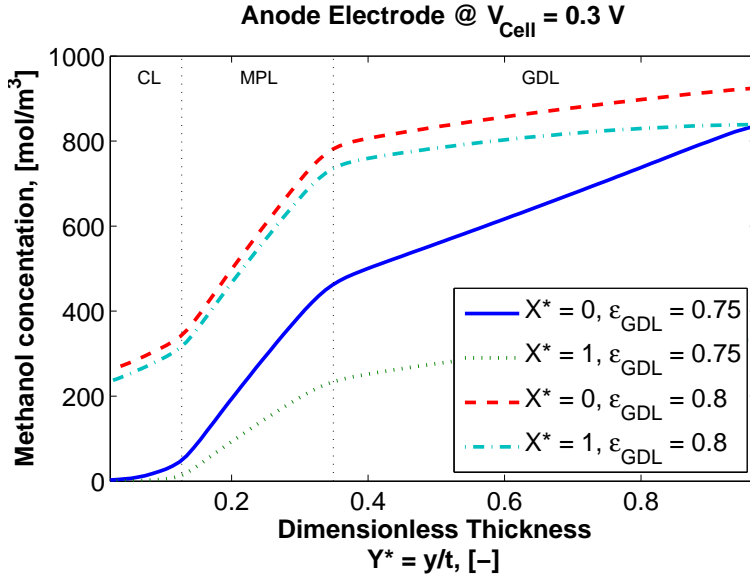
**Figure 5.16:** Methanol concentration distribution in the anode electrode for two cases of GDL porosity at cell voltage 0.3 V. A dimensionless distance of X* = 0 and X* = 1 are equivalent to under the channel and land, respectively.

one major purpose, which is to assist in decreasing the methanol crossover. However, this also has the disadvantage that it leads to a significant reduction in the limiting current density, depending on the applied capillary pressure boundary condition. Indeed, to balance methanol crossover and methanol mass transport losses is of great importance in DMFC design. As exemplified in this comparison, increasing porosity entails a higher power output, but it likewise results in a higher parasitic current density. In the case with the higher volume porosity, a parasitic current density of 0.02 A/cm$^2$ is seen, as opposed to nearly zero for the low porosity case. Actually, this implies from a Faradaic efficiency point of view that the low porosity case is the best scenario, since a higher extent of fuel is converted into electricity. Nevertheless, this does not outweigh the observed reduction in the electrical efficiency.

Interestingly, the decrease in limiting current density is also, to some extent, a reflection of an increased evaporation rate. This is clearly seen from the lower methanol concentration at the GDL-channel interface. The higher the liquid volume fraction, the lower the evaporation rate of methanol and water becomes. Consequently, the rate of methanol removal via gas outflow
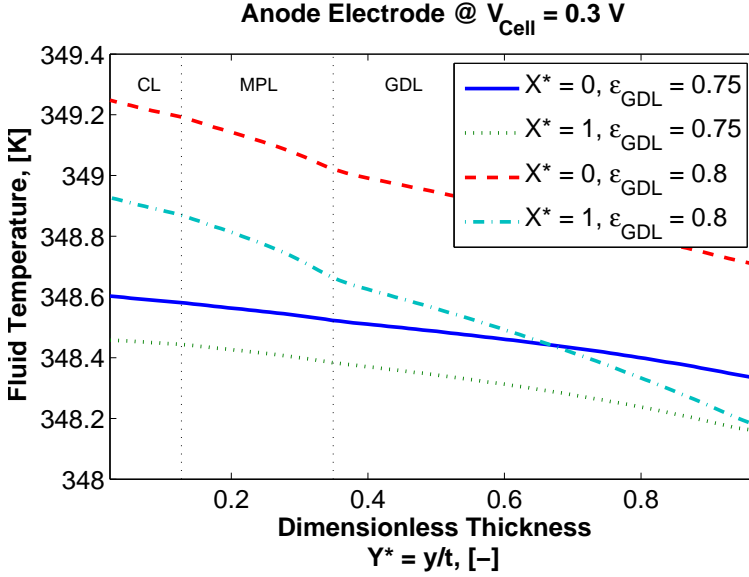
**Figure 5.17:** Fluid Temperature concentration distribution in the anode electrode for two cases of GDL porosity at cell voltage 0.3 V. A dimensionless distance of $X^*$ = 0 and $X^*$ = 1 are equivalent to under the channel and land, respectively.

from the anode electrode increases for the low porosity case. Furthermore, a difference in phase change is also imposed due to a difference in the temperature and hence a difference in saturation pressure. The higher the current density and the higher the methanol crossover, the higher the extent of irreversible heat production due electrochemical reactions as well as ion and electron transport. This means that the temperature rises, unless an efficient cooling is applied. In this case a minor temperature increase is observed as shown in figure 5.17. Thus, only a slight increase in evaporation rate is caused by it.

In figure 5.18, the resulting methanol concentration distribution along the channel length can be seen. In accordance with the increasing gas volume fraction along the channel, a decrease is observed in the methanol concentration. This occurs although a significant higher extent of convective species mixing happens within the channel. Because the methanol concentration decreases along the channel length at the GDL-channel interface an equivalent decrease in electrochemical performance occurs. This is bound to happen since the possible gradient for methanol diffusion towards the CL decreases.

A concern with present two-fluid model could be that it does not fully
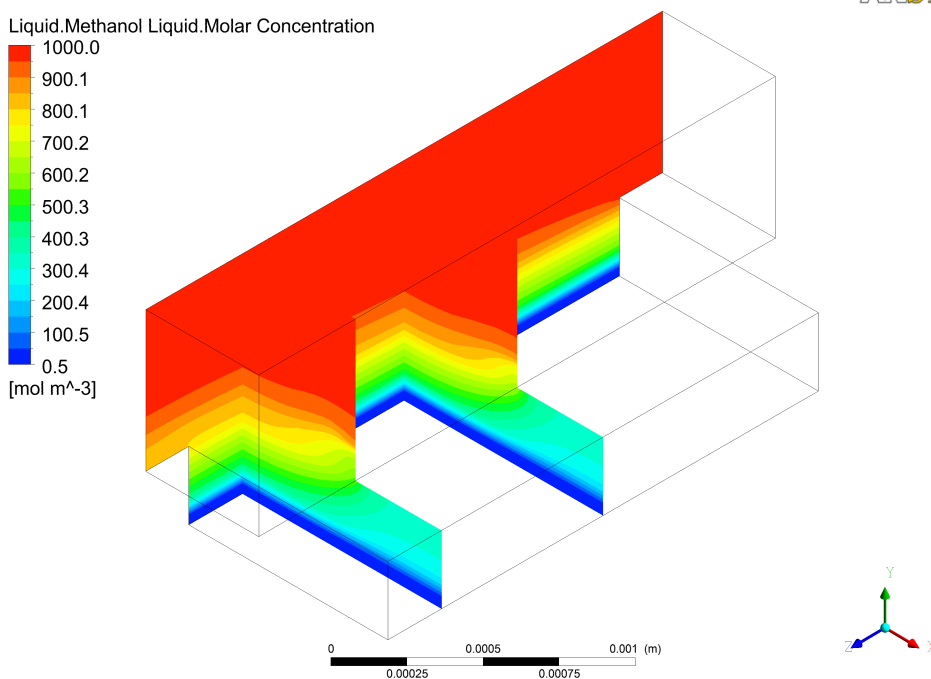
**Figure 5.18:** A three-dimensional liquid phase methanol concentration distribution in the anode channel and electrode at a GDL porosity of 0.75, cell voltage of 0.3 V and a current density of 0.17 A/cm$^2$

account for two-phase flow mixing in the channel associated with microscopic deviations. A higher extent of two-phase flow mixing across the channel height would increase the methanol concentration near the GDL-channel, whereby a larger gradient for methanol diffusion would be possible.

The great challenge with increasing DMFC performance without directly decreasing the diffusivity of methanol in Nafion lies in not doing so at the expense of a decreased limiting current density or an increased ohmic loss. Unfortunately, what decreases methanol transport towards the CL, decreases the limiting current density, and what decreases methanol transport from the anode CL to the cathode CL often decreases ion transport. This dilemma is difficult to come around. One option could be to decrease the fraction of hydrophilic pores of the CL by increasing the PTFE loading and hereby lower the liquid phase volume fraction. This then lowers methanol and water uptake, since less liquid is in contact with Nafion. Another option would be to optimize the Nafion volume fraction in the CL, such that a balance is

obtained between decreased methanol transport and decreased ion conductivity.

# Chapter 6

# Conclusion and Outlook

*In the beginning of this chapter a summary is given of accomplishments made in this work in accordance with the initial problem definition. Afterward, recommendations for future work are given with reference to the applied research methodology.*

## 6.1   Final remarks

In this dissertation a three-dimensional, two-phase, multicomponent, non-isothermal mathematical model of a DMFC was presented and partially validated. In the development of this model, the fundamental macroscopic transport of methanol and water was of particular importance. To improve model predictions, modeling parameters were assessed experimentally, as well as experimental data of DMFC performance and methanol crossover under various operation conditions were provided for future validation studies.

The current body of knowledge within DMFC modeling was incrementally expanded in this work by accounting for detailed two-phase phenomena governing porous media assemblies in a three-dimensional framework using the two-fluid approach and by adding the influence of non-equilibrium and non-ideal thermodynamics governing the phase change and sorption/desorption of water and methanol in porous media and polymer electrolyte membranes, respectively. Furthermore, throughout this work different modeling studies were carried out to elucidate modeling capabilities, to investigate certain transport phenomena or to stress the importance of various modeling assumptions in relation to boundary conditions.

In the first study a preliminary half-cell cathode model was used for in-

vestigating the importance of inhomogeneous GDL compression on liquid phase and oxygen transport. It was found that inhomogeneous compression causes an appreciable difference between the predicted liquid volume fraction under the land and under the channel. Correspondingly, a significant difference in oxygen transport was found. Moreover, in this study the ability of the model to capture the complex coupling between capillary pressure transport and phase change was underlined and discussed.

In the second study it was made probable that the alleged existence of a local maximum in the Fickian diffusivity of water in Nafion around a water content of $\lambda = 3$, merely is a mathematical artifact due to its derivation. By carefully accounting for the relation between water activity and water content, a spikeless expression was found. Moreover, it was shown that its existence cannot be verified by water flux measurements unless detailed interfacial transport processes are accounted for. Similarly, it was shown that permeation experiments falsely can predict a spike in the diffusivity of water, by again not carefully accounting for the relation between water activity and water content.

In the third study the importance and sensitivity of the coupling between volume porosity and the capillary pressure boundary condition was underlined. It was shown, how a pressure based boundary condition predicts considerable differences in the phase distribution of the GDL when changing its volume porosity. In contrast, a constant liquid volume fraction boundary condition, commonly found in the literature, would merely predict minor differences, since this approach inherently assumes that the liquid phase pressure in the channel is high enough to intrude nearly all hydrophobic pores regardless of the applied operation conditions. Moreover, it was shown how this imposed difference in phase distribution can cause substantial differences in the limiting current density due to methanol mass transport losses.

Meanwhile, the devised mathematical model suffers from some shortcomings. For a mesh consisting of around 50.000 nodes, the computational time associated with solving it in CFX is in the order of several weeks to months on a Linux-cluster at the Department of Energy Technology. Consequently, it is not suitable for a full-scale validation study nor a multi-variable parameter variation. Nonetheless, as shown in the present work, it can still be used for studying particular phenomena and their impact on DMFC performance. Moreover, since the developed model inherently behaves more stable at low liquid volume fractions, it can with advantage be used for studying PEMFC, which are less prone to complete flooding.

In summary it can be stated that the two-fluid DMFC model presented here has made substantial contributions and enhanced the fundamental knowledge in the field. The development of CFD models per se cannot solve the issue of methanol crossover and the thereby following fuel loss and mixed potential. However, they can be used for optimizing performance by obtaining a compromise between often conflicting requirements.

## 6.2 Future work

Although a comprehensive DMFC model has been developed, a number of issues still remain to be addressed. These include the applied research methodology used for modeling macroscopic transport phenomena and the numerical challenges associated with solving the mass and momentum equations. In particular, the latter remains the single most important challenge in making the devised model suitable for full-scale validations and parameter studies.

As demonstrated in the above analysis, the developed model permits for detailed studies of macroscopic phenomena, however at the present moment the long computational time prevents this from being realizable within the confinements of this project. Therefore, it is essential that the stability of the capillary pressure model becomes improved with attention to the interface between porous media and appropriate relaxation techniques for the coupling between volume fraction and velocity. In doing so, a significant improvement in the computational time can be obtained, since the remaining transport equations are much less prone to divergence. In fact, a solution time of few days, rather than months would be realistic. Meanwhile, in the CFD framework of CFX 14, this seems unrealistic, since it does not allow for a proper formulation of the governing capillary pressure model. Moreover, the present implementation of the velocity-pressure coupling by Rhie-Chow interpolations is the cause of excessive wiggles and divergence. In future work, it is therefore recommended to pursue other software's than CFX for the modeling of DMFC, despite its clear advantages in the modeling of other two-phase flow phenomena using the two-fluid approach.

In addition to the before mentioned numerical challenges, the following list of modeling improvements are recommended:

- Transport in the anode is highly sensitive to the capillary pressure boundary condition used, as it determines the amount of liquid present. Including variations in channel overpressure along the channel would

significantly improve the predicted liquid phase and hence mass transport losses, which often are the most difficult part of the polarization curve to match.

- An important task which remains to be addressed, in accordance with the research definition, is the verification of the use of dilute solution theory models for transport of water, methanol and ions in PEM. Although, experimental data of methanol crossover are available, a verification study has not yet been possible. Aside from this, species-species interaction could easily be incorporate in the current model. The greatest restriction in doing so lies in the availability of transport properties in the literature. It could therefore be beneficial to devise a series of experiments to which an one-dimensional membrane model could be fitted.

- The employed modified Leverett J function is more qualitative, than quantitative. An improved predictability could be gained by incorporating either a bundle-of-capillary model fitted to the exact pore size distribution used in the CL, MPL and GDL. However, the implementation in a CFD framework, may require a complete restructuring of the solved transport equations, which is not possible in CFX.

- A topic which was not covered in detail in this study is detailed species transport in the vicinity of the electro-catalyst surface area and detailed multicomponent transport in the porous layers. The former could for example be accounted for by using appropriate agglomerate transport models and the latter using a detailed Maxwell-Stefan model.

# Bibliography

[1] Ryan Anderson, Lifeng Zhang, Yulong Ding, Mauricio Blanco, Xiaotao Bi, and David P. Wilkinson. A critical review of two-phase flow in gas flow channels of proton exchange membrane fuel cells. *Journal of Power Sources*, 195(15):4531–4553, August 2010. ISSN 03787753. doi: 10.1016/j.jpowsour.2009.12.123. URL `http://linkinghub.elsevier.com/retrieve/pii/S0378775310000510`.

[2] ANSYS. ANSYS CFX-Solver Modeling Guide. Technical report, ANSYS, Canonsburg, 2011.

[3] F Barbir. *PEM Fuel Cells: Theory and Practice*. Academic Press. Elsevier/Academic Press, 2012. ISBN 9780123877109. URL `http://books.google.dk/books?id=elO7n4Z6uLoC`.

[4] L Barelli, G Bidini, F Gallorini, and A Ottaviano. An energetic-exergetic comparison between PEMFC and SOFC-based micro-CHP systems. *International Journal of Hydrogen Energy*, 36(4):3206–3214, February 2011. ISSN 0360-3199. doi: http://dx.doi.org/10.1016/j.ijhydene.2010.11.079. URL `http://www.sciencedirect.com/science/article/pii/S0360319910022949`.

[5] J.J. Baschuk and Xianguo Li. Modeling of ion and water transport in the polymer electrolyte membrane of PEM fuel cells. *International Journal of Hydrogen Energy*, 35(10):5095–5103, May 2010. ISSN 03603199. doi: 10.1016/j.ijhydene.2009.10.032. URL `http://linkinghub.elsevier.com/retrieve/pii/S0360319909016036`.

[6] Maria Bass and Viatcheslav Freger. Hydration of Nafion and Dowex in liquid and vapor environment: Schroeder's paradox and microstructure. *Polymer*, 49(2):497–506, January 2008. ISSN 0032-3861. URL `http://www.sciencedirect.com/science/article/pii/S0032386107011159`.

[7] Maria Bass, Amir Berman, Amarjeet Singh, Oleg Konovalov, and Viatcheslav Freger. Surface Structure of Nafion in Vapor and Liquid. *The Journal of Physical Chemistry B*, 114(11):3784–3790, March 2010. ISSN 1520-6106. doi: 10.1021/jp9113128. URL `http://dx.doi.org/10.1021/jp9113128`.

[8] Jay Benziger, Andrew Bocarsly, May Cheah, Paul Majsztrik, Barclay Satterfield, and Qiao Zhao. Mechanical and Transport Properties of Nafion: Effects of Temperature and Water Activity. In Andrew Bocarsly and David Michael P Mingos, editors, *Fuel Cells and Hydrogen Storage*, volume 141 of *Structure & Bonding*, pages 85–113. Springer Berlin / Heidelberg, 2011. ISBN 978-3-642-21779-1. URL `http://dx.doi.org/10.1007/430_2011_41`.

[9] Dawn M Bernardi and Mark W Verbrugge. A Mathematical Model of the Solid-Polymer-Electrolyte Fuel Cell. *Journal of The Electrochemical Society*, 139(9):2477–2491, January 1992. doi: 10.1149/1.2221251. URL `http://jes.ecsdl.org/content/139/9/2477.abstract`.

[10] T Berning and N Djilali. A 3D, Multiphase, Multicomponent Model of the Cathode and Anode of a PEM Fuel Cell. *Journal of the Electrochemical Society*, 150:A1589–A1598, 2003.

[11] T Berning and S K Kæ r. Low stoichiometry operation of a proton exchange membrane fuel cell employing the interdigitated flow field - A modeling study. *International Journal of Hydrogen Energy*, 37(10):8477–8489, May 2012. ISSN 0360-3199. URL `http://www.sciencedirect.com/science/article/pii/S0360319912005010`.

[12] T Berning, M Odgaard, and S K Kæ r. A Computational Analysis of Multiphase Flow Through PEMFC Cathode Porous Media Using the Multifluid Approach. *Journal of the Electrochemical Society*, 156: B1301–B1311, 2009.

[13] T Berning, M Odgaard, and S K Kæ r. Water balance simulations of a polymer-electrolyte membrane fuel cell using a two-fluid model. *Journal of Power Sources*, 196(15):6305–6317, 2011. ISSN 0378-7753. doi: DOI:10.1016/j.jpowsour.2011.03.068. URL `http://www.sciencedirect.com/science/article/pii/S0378775311006835`.

[14] Torsten Berning, Madeleine Odgaard, and Søren Knudsen Kæ r. A study of multi-phase flow through the cathode side of an interdigitated flow field using a multi-fluid model. *Journal of*

*Power Sources*, 195(15):4842–4852, August 2010. ISSN 0378-7753. URL `http://www.sciencedirect.com/science/article/B6TH1-4YCS015-1/2/adf6164a54fc905d326d1e9d74dfbc25`.

[15] B Carnes and N Djilali. Analysis of coupled proton and water transport in a PEM fuel cell using the binary friction membrane model. 52: 1038–1052, 2006. doi: 10.1016/j.electacta.2006.07.006.

[16] Pyoungho Choi and Ravindra Datta. Sorption in Proton-Exchange Membranes . *Journal of The Electrochemical Society*, 150(12):E601–E607, January 2003. doi: 10.1149/1.1623495. URL `http://jes.ecsdl.org/content/150/12/E601.abstract`.

[17] Nurettin Demirdöven and John Deutch. Hybrid Cars Now, Fuel Cell Cars Later. *Science*, 305(5686):974–976, August 2004. doi: 10.1126/science.1093965. URL `http://www.sciencemag.org/content/305/5686/974.abstract`.

[18] M Dentice d'Accadia, M Sasso, S Sibilio, and L Vanoli. Micro-combined heat and power in residential and light commercial applications. *Applied Thermal Engineering*, 23(10):1247–1259, July 2003. ISSN 1359-4311. doi: http://dx.doi.org/10.1016/S1359-4311(03)00030-9. URL `http://www.sciencedirect.com/science/article/pii/S1359431103000309`.

[19] Jiri Divisek, Jurgen Fuhrmann, Klaus Gartner, and Rita Jung. Performance Modeling of a Direct Methanol Fuel Cell. *Journal of The Electrochemical Society*, 150(6):A811, 2003. ISSN 00134651. doi: 10.1149/1.1572150. URL `http://jes.ecsdl.org/cgi/doi/10.1149/1.1572150`.

[20] N Djilali. Computational modelling of polymer electrolyte membrane (PEM) fuel cells: Challenges and opportunities. *Eenrgy*, 32:269–280, 2007.

[21] Mingzhe Dong and Francis A. L. Dullien. Porous Media Flows. In *Multiphase Flow Handbook*. Taylor & Francis, CRC, 2005.

[22] Christopher K Dyer. Fuel cells for portable applications. *Fuel Cells Bulletin*, 2002(3):8–9, March 2002. ISSN 1464-2859. doi: http://dx.doi.org/10.1016/S1464-2859(02)80334-0. URL `http://www.sciencedirect.com/science/article/pii/S1464285902803340`.

[23] Gwynn J. Elfring and Henning Struchtrup. Thermodynamic considerations on the stability of water in Nafion. *Journal of Membrane Science*, 297(1-2):190–198, July 2007. ISSN 03767388. doi: 10.1016/j.memsci.2007.03.044. URL `http://linkinghub.elsevier.com/retrieve/pii/S0376738807002104`.

[24] J Fimrite, B Carnes, H Struchtrup, and N Djilali. Transport Phenomena in Polymer Electrolyte Membranes. 2005. doi: 10.1149/1.1952647.

[25] Viatcheslav Freger. Hydration of Ionomers and Schroeders Paradox in Nafion. *The Journal of Physical Chemistry B*, 113(1):24–36, December 2008. ISSN 1520-6106. doi: 10.1021/jp806326a. URL `http://dx.doi.org/10.1021/jp806326a`.

[26] Joshua J. Garvin and Jeremy P. Meyers. Modeling of Coupled Multiphase Transport in Direct Methanol Fuel Cell Diffusion Layers. *Journal of The Electrochemical Society*, 158(9):B1119, 2011. ISSN 00134651. doi: 10.1149/1.3603974. URL `http://jes.ecsdl.org/cgi/doi/10.1149/1.3603974`.

[27] Craig M Gates and John Newman. Equilibrium and diffusion of methanol and water in a nafion 117 membrane. *AIChE Journal*, 46 (10):2076–2085, 2000. ISSN 1547-5905. doi: 10.1002/aic.690461018. URL `http://dx.doi.org/10.1002/aic.690461018`.

[28] Jiabin Ge and Hongtan Liu. A three-dimensional two-phase flow model for a liquid-fed direct methanol fuel cell. *Journal of Power Sources*, 163(2):907–915, January 2007. ISSN 0378-7753. URL `http://www.sciencedirect.com/science/article/pii/S0378775306020453`.

[29] Shanhai Ge, Xuguang Li, Baolian Yi, and I-Ming Hsing. Absorption, Desorption, and Transport of Water in Polymer Electrolyte Membranes for Fuel Cells. *Journal of The Electrochemical Society*, 152(6):A1149–A1157, 2005. doi: 10.1149/1.1899263. URL `http://link.aip.org/link/?JES/152/A1149/1`.

[30] Arne B. Geiger, John Newman, and John M. Prausnitz. Phase equilibria for water-methanol mixtures in perfluorosulfonic-acid membranes. *AIChE Journal*, 47(2):445–452, February 2001. ISSN 00011541. doi: 10.1002/aic.690470221. URL `http://doi.wiley.com/10.1002/aic.690470221`.

[31] Markus Grötsch and Michael Mangold. A two-phase PEMFC model for process control purposes. *Chemical Engineering Science*, 63 (2):434–447, January 2008. ISSN 0009-2509. URL `http://www.sciencedirect.com/science/article/pii/S0009250907007415`.

[32] Markus Grotsch, Richard Hanke-Rauschenbach, and Michael Mangold. Bifurcation Analysis of a Two-Phase PEMFC Model. *Journal of Fuel Cell Science and Technology*, 5(2):21001, 2008. doi: 10.1115/1.2885392. URL `http://link.aip.org/link/?FCT/5/021001/1`.

[33] Vladimir Gurau, Jr. Thomas A. Zawodzinski, and Jr. J. Adin Mann. Two-Phase Transport in PEM Fuel Cell Cathodes. *Journal of Fuel Cell Science and Technology*, 5(2):21009, 2008. doi: 10.1115/1.2821597. URL `http://link.aip.org/link/?FCT/5/021009/1`.

[34] Fredrik Hallberg, Thomas Vernersson, Erik Thyboll Pettersson, Sergey V Dvinskikh, Gï¿œran Lindbergh, and Istvï¿œn Furï¿œe. Electrokinetic transport of water and methanol in Nafion membranes as observed by NMR spectroscopy. *Electrochimica Acta*, 55(10):3542–3549, 2010. ISSN 0013-4686. doi: DOI:10.1016/j.electacta.2010.01.064. URL `http://www.sciencedirect.com/science/article/B6TG0-4Y7P4R6-8/2/29b68062f90aaf8a4c7161e3ec30adb0`.

[35] Daniel T Hallinan and Yossef A Elabd. Diffusion and Sorption of Methanol and Water in Nafion Using Time-Resolved Fourier Transform Infrared Attenuated Total Reflectance Spectroscopy. *The Journal of Physical Chemistry B*, 111(46):13221–13230, 2007. doi: 10.1021/jp075178n. URL `http://pubs.acs.org/doi/abs/10.1021/jp075178n`.

[36] Ya-Ling He, Zheng Miao, Tian-Shou Zhao, and Wei-Wei Yang. Numerical study of the effect of the GDL structure on water crossover in a direct methanol fuel cell. *International Journal of Hydrogen Energy*, 37(5):4422–4438, March 2012. ISSN 0360-3199. URL `http://www.sciencedirect.com/science/article/pii/S0360319911026000`.

[37] William Y Hsu and Timothy D Gierke. Ion transport and clustering in nafion perfluorinated membranes. *Journal of Membrane Science*, 13 (3):307–326, February 1983. ISSN 0376-7388. doi: http://dx.doi.org/10.1016/S0376-7388(00)81563-X. URL `http://www.sciencedirect.com/science/article/pii/S037673880081563X`.

[38] Irfan S. Hussaini and Chao-Yang Wang. Visualization and quantifica-
tion of cathode channel flooding in PEM fuel cells. *Journal of Power
Sources*, 187(2):444–451, February 2009. ISSN 03787753. doi: 10.
1016/j.jpowsour.2008.11.030. URL `http://linkinghub.elsevier.
com/retrieve/pii/S0378775308021630`.

[39] IPCC. Summary for Policymakers. In: Climate Change 2007: The
Physical Science Basis. Contribution of Working Group I to the
Fourth Assessment Report of the Intergovernmental Panel on Climate
Change. Technical report, 2007.

[40] HugoA. Jakobsen. Multiphase Flow. In *Chemical Reactor Modeling
SE - 3*, pages 335–501. Springer Berlin Heidelberg, 2008. ISBN 978-3-
540-25197-2. doi: 10.1007/978-3-540-68622-4\_3. URL `http://dx.
doi.org/10.1007/978-3-540-68622-4_3`.

[41] G. J. M. Janssen. A Phenomenological Model of Water Transport in a
Proton Exchange Membrane Fuel Cell. *Journal of The Electrochemical
Society*, 148(12):A1313, 2001. ISSN 00134651. doi: 10.1149/1.1415031.
URL `http://jes.ecsdl.org/cgi/doi/10.1149/1.1415031`.

[42] Sandra Jeck, Philip Scharfer, and Matthias Kind. Absence of Schroed-
ers paradox: Experimental evidence for water-swollen Nafion mem-
branes. *Journal of Membrane Science*, 373(1-2):74–79, May 2011.
ISSN 03767388. doi: 10.1016/j.memsci.2011.02.036. URL `http:
//linkinghub.elsevier.com/retrieve/pii/S0376738811001566`.

[43] Rongzhong Jiang and Deryn Chu. Comparative Studies of Methanol
Crossover and Cell Performance for a DMFC. *Journal of The Elec-
trochemical Society*, 151(1):A69–A76, 2004. doi: 10.1149/1.1629093.
URL `http://link.aip.org/link/?JES/151/A69/1`.

[44] R Krishna and J A Wesselingh. The Maxwell-Stefan approach to mass
transfer. *Chemical Engineering Science*, 52(6):861–911, March 1997.
ISSN 0009-2509. doi: http://dx.doi.org/10.1016/S0009-2509(96)
00458-7. URL `http://www.sciencedirect.com/science/article/
pii/S0009250996004587`.

[45] Ahmet Kusoglu, Miguel A Modestino, Alexander Hexemer, Rachel A
Segalman, and Adam Z Weber. Subsecond Morphological Changes in
Nafion during Water Uptake Detected by Small-Angle X-ray Scatter-
ing. *ACS Macro Letters*, 1(1):33–36, November 2011. doi: 10.1021/
mz200015c. URL `http://dx.doi.org/10.1021/mz200015c`.

[46] Roberto Lemoine-Nava, Richard Hanke-Rauschenbach, Michael Mangold, and Kai Sundmacher. The gas diffusion layer in polymer electrolyte membrane fuel cells: A process model of the two-phase flow. *International Journal of Hydrogen Energy*, 36(2):1637–1653, January 2011. ISSN 0360-3199. URL `http://www.sciencedirect.com/science/article/pii/S0360319910021166`.

[47] R Lenormand, E Toubol, and C Zarcone. Numerical models and experiments on immisible displacement in porous media. *Journal of Fluid Mechanics*, 189:165, 1988.

[48] S. Litster and G. McLean. PEM fuel cell electrodes. *Journal of Power Sources*, 130(1-2):61–76, May 2004. ISSN 03787753. doi: 10.1016/j.jpowsour.2003.12.055. URL `http://linkinghub.elsevier.com/retrieve/pii/S0378775304000631`.

[49] Hansan Liu, Chaojie Song, Lei Zhang, Jiujun Zhang, Haijiang Wang, and David P Wilkinson. A review of anode catalysis in the direct methanol fuel cell. *Journal of Power Sources*, 155(2): 95–110, April 2006. ISSN 0378-7753. doi: http://dx.doi.org/10.1016/j.jpowsour.2006.01.030. URL `http://www.sciencedirect.com/science/article/pii/S0378775306000772`.

[50] Wenpeng Liu and Chao-Yang Wang. Modeling water transport in liquid feed direct methanol fuel cells. *Journal of Power Sources*, 164 (1):189–195, January 2007. ISSN 0378-7753. doi: http://dx.doi.org/10.1016/j.jpowsour.2006.10.047. URL `http://www.sciencedirect.com/science/article/pii/S0378775306021458`.

[51] G Q Lu and C Y Wang. Electrochemical and flow characterization of a direct methanol fuel cell. *Journal of Power Sources*, 134(1):33–40, July 2004. ISSN 0378-7753. URL `http://www.sciencedirect.com/science/article/pii/S037877530400271X`.

[52] Zhiping Luo, Zhangyong Chang, Yuxia Zhang, Zhen Liu, and Jing Li. Electro-osmotic drag coefficient and proton conductivity in Nafion membrane for PEMFC. *International Journal of Hydrogen Energy*, 35 (7):3120–3124, April 2010. ISSN 03603199. doi: 10.1016/j.ijhydene.2009.09.013. URL `http://linkinghub.elsevier.com/retrieve/pii/S0360319909013846`.

[53] Paul Majsztrik, Andrew Bocarsly, and Jay Benziger. Water Perme-
ation through Nafion Membranes: The Role of Water Activity. *The
Journal of Physical Chemistry B*, 112(51):16280–16289, 2008. doi:
10.1021/jp804197x. URL `http://pubs.acs.org/doi/abs/10.1021/
jp804197x`.

[54] Paul W Majsztrik, M Barclay Satterfield, Andrew B Bocarsly, and
Jay B Benziger. Water sorption, desorption and transport in Nafion
membranes. *Journal of Membrane Science*, 301:93–106, 2007. ISSN
0376-7388. doi: 10.1016/j.memsci.2007.06.022. URL `http://www.
sciencedirect.com/science/article/pii/S0376738807003882`.

[55] Pedro Mateo-villanueva and Marc Secanell. Analysis of Two-Phase
Transport In Utra-Thin Catalyst Layer Based Electrodes using a
Mixed Wettability MPL Model. In *Proceedings of the ASME 2012
10th Fuel Cell Science, Engineering and Technology Conference*, pages
1–14. ASME, 2012.

[56] Kenneth a Mauritz and Robert B Moore. State of understanding of
nafion. *Chemical reviews*, 104(10):4535–85, October 2004. ISSN 0009-
2665. URL `http://www.ncbi.nlm.nih.gov/pubmed/15669162`.

[57] Sandip Mazunder and James Vernon Cole. Rigorous 3-D Mathematical
Modelling of PEM Fuel Cells:. *Journal of The Electrochemical Society*,
150:A1510–A1517, 2003.

[58] Jure Mencinger and Iztok Žun. On the finite volume discretization of
discontinuous body force field on collocated grid: Application to VOF
method. *Journal of Computational Physics*, 221(2):524–538, February
2007. ISSN 00219991. doi: 10.1016/j.jcp.2006.06.021. URL `http:
//linkinghub.elsevier.com/retrieve/pii/S0021999106003019`.

[59] P J Meyers and J Newman. Simulation of the Direct Methanol Fuel
Cell - II. Modeling and Data Analysis of Transport and Kinetic Phe-
nomena. *Journal of The Electrochemical Society*, 149:A718–A728,
2002.

[60] Z Miao, Y He, X Li, and J Zou. A two-dimensional two-phase
mass transport model for direct methanol fuel cells adopting a modi-
fied agglomerate approach. *Journal of Power Sources*, 185(2):1233–
1246, December 2008. ISSN 03787753. doi: 10.1016/j.jpowsour.
2008.06.007. URL `http://linkinghub.elsevier.com/retrieve/
pii/S037877530801207X`.

[61] Zheng Miao, Ya-Ling He, and Jin-Qiang Zou. Modeling the effect of anisotropy of gas diffusion layer on transport phenomena in a direct methanol fuel cell. *Journal of Power Sources*, 195(11): 3693–3708, June 2010. ISSN 03787753. doi: 10.1016/j.jpowsour. 2009.12.048. URL `http://linkinghub.elsevier.com/retrieve/pii/S0378775309023106`.

[62] Sathya Motupally, Aaron J Becker, and John W Weidner. Diffusion of Water in Nafion 115 Membranes. *Journal of The Electrochemical Society*, 147(9):3171–3177, September 2000. URL `http://dx.doi.org/10.1149/1.1393879`.

[63] Bruce R. Munson, Donald F. Young, and Theodore H. Okiishi. *Fundamentals of Fluid Mechanics*. John Wiley & Sons, Inc., fifth edition, 2006. ISBN 978-0-471-67582-2.

[64] Jin Hyun Nam and Massoud Kaviany. Effective diffusivity and water-saturation distribution in single- and two-layer PEMFC diffusion medium. *International Journal of Heat and Mass Transfer*, 46(24): 4595–4611, 2003. ISSN 0017-9310. doi: DOI:10.1016/S0017-9310(03) 00305-3. URL `http://www.sciencedirect.com/science/article/B6V3H-497R77K-2/2/a5f5fd77d0216aa2f2e6b671d44c49c3`.

[65] SR Narayan and TI Valdez. High-energy portable fuel cell power sources. *Electrochemical Society Interface*, 2008. URL `http://electrochem.org/dl/interface/wtr/wtr08/wtr08_p40-45.pdf`.

[66] Vladimir Neburchilov, Jonathan Martin, Haijiang Wang, and Jiujun Zhang. A review of polymer electrolyte membranes for direct methanol fuel cells. *Journal of Power Sources*, 169(2):221–238, June 2007. ISSN 0378-7753. URL `http://www.sciencedirect.com/science/article/pii/S0378775307005897`.

[67] P A Nikrityuk. *Computational Thermo-Fluid Dynamics: In Materials Science and Engineering*. Wiley, 2011. ISBN 9783527636082. URL `http://books.google.dk/books?id=NAxwuvAjfZkC`.

[68] Ryan O'Hayre, Suk Won Cha, Whitney Colella, and Fritz B. Prinz. *Fuel Cell Fundamentals*. John Wiley & Sons, Inc., 2nd edition, 2009. ISBN 978-0-470-25843-9.

[69] George A Olah. Beyond Oil and Gas: The Methanol Economy. *Angewandte Chemie International Edition*, 44(18):2636–2639, April

2005. ISSN 1521-3773. doi: 10.1002/anie.200462121. URL `http://dx.doi.org/10.1002/anie.200462121`.

[70] V B Oliveira, D S Falcão, C M Rangel, and A M F R Pinto. A comparative study of approaches to direct methanol fuel cells modelling. 32:415–424, 2007. doi: 10.1016/j.ijhydene.2006.06.049.

[71] Lisa M Onishi, John M Prausnitz, and John Newman. Water and Nafion Equilibria. Absence of Schroeder's Paradox. *The Journal of Physical Chemistry B*, 111(34):10166–10173, 2007. doi: 10.1021/jp073242v. URL `http://pubs.acs.org/doi/abs/10.1021/jp073242v`.

[72] Ugur Pasaogullari and Chao-Yang Wang. Two-phase transport and the role of micro-porous layer in polymer electrolyte fuel cells. *Electrochimica Acta*, 49(25):4359–4369, October 2004. ISSN 0013-4686. doi: http://dx.doi.org/10.1016/j.electacta.2004.04.027. URL `http://www.sciencedirect.com/science/article/pii/S0013468604003846`.

[73] S V Patankar. Numerical heat transfer and fluid flow. *Washington, DC, Hemisphere Publishing Corp., 1980. 210 p.*, 1, 1980.

[74] Zhigang Qi and Arthur Kaufman. Improvement of water management by a microporous sublayer for PEM fuel cells. *Journal of Power Sources*, 109(1):38–46, June 2002. ISSN 0378-7753. doi: http://dx.doi.org/10.1016/S0378-7753(02)00058-7. URL `http://www.sciencedirect.com/science/article/pii/S0378775302000587`.

[75] Xiaoming Ren, Thomas E Springer, Thomas A Zawodzinski, and Shimshon Gottesfeld. Methanol Transport Through Nation Membranes. Electro-osmotic Drag Effects on Potential Step Measurements. *Journal of The Electrochemical Society*, 147(2):466–474, January 2000. doi: 10.1149/1.1393219. URL `http://jes.ecsdl.org/content/147/2/466.abstract`.

[76] D Rivin, CE Kendrick, PW Gibson, and NS Schneider. Solubility and transport behavior of water and alcohols in Nafion. *Polymer*, 42:623–635, 2001. URL `http://www.sciencedirect.com/science/article/pii/S0032386100003505`.

[77] Laurent Rubatat, Anne Laure Rollet, Gérard Gebel, and Olivier Diat. Evidence of Elongated Polymeric Aggregates in Nafion. *Macro-*

*molecules*, 35(10):4050–4055, April 2002. ISSN 0024-9297. doi: 10.1021/ma011578b. URL `http://dx.doi.org/10.1021/ma011578b`.

[78] M Barclay Satterfield and J B Benziger. Non-Fickian Water Vapor Sorption Dynamics by Nafion Membranes. *The Journal of Physical Chemistry B*, 112(12):3693–3704, 2008. ISSN 1520-6106. URL `http://dx.doi.org/10.1021/jp7103243`.

[79] Andreas Schäfer, John B Heywood, and Malcolm A Weiss. Future fuel cell and internal combustion engine automobile technologies: A 25-year life cycle and fleet impact assessment. *Energy*, 31(12):2064–2087, September 2006. ISSN 0360-5442. doi: http://dx.doi.org/10.1016/j.energy.2005.09.011. URL `http://www.sciencedirect.com/science/article/pii/S0360544205001854`.

[80] N S Schneider and D Rivin. Steady state analysis of water vapor transport in ionomers. *Polymer*, 51(3):671–678, 2010. ISSN 0032-3861. doi: DOI:10.1016/j.polymer.2009.12.005. URL `http://www.sciencedirect.com/science/article/pii/S0032386109010702`.

[81] Thorsten Schultz and Kai Sundmacher. Mass, charge and energy transport phenomena in a polymer electrolyte membrane (PEM) used in a direct methanol fuel cell (DMFC): Modelling and experimental validation of fluxes. *Journal of Membrane Science*, 276(1-2):272–285, 2006. ISSN 0376-7388. doi: DOI:10.1016/j.memsci.2005.10.001. URL `http://www.sciencedirect.com/science/article/pii/S0376738805007155`.

[82] Akimi Serizawa, Ziping Feng, and Zensaku Kawara. Two-phase flow in microchannels. *Experimental Thermal and Fluid Science*, 26(6-7):703–714, August 2002. ISSN 0894-1777. doi: http://dx.doi.org/10.1016/S0894-1777(02)00175-9. URL `http://www.sciencedirect.com/science/article/pii/S0894177702001759`.

[83] N Shao, A Gavriilidis, and P Angeli. Flow regimes for adiabatic gas-liquid flow in microchannels. *Chemical Engineering Science*, 64 (11):2749–2761, June 2009. ISSN 0009-2509. doi: http://dx.doi.org/10.1016/j.ces.2009.01.067. URL `http://www.sciencedirect.com/science/article/pii/S0009250909000827`.

[84] Puneet K Sinha and Chao-Yang Wang. Pore-network modeling of liquid water transport in gas diffusion layer of a

polymer electrolyte fuel cell. *Electrochimica Acta*, 52(28): 7936–7945, November 2007. ISSN 0013-4686. URL `http://www.sciencedirect.com/science/article/B6TG0-4P2J0BK-4/2/38d48c3729e608542fb651fff2389523`.

[85] E Skou, P Kauranen, and J Hentschel. Water and methanol uptake in proton conducting Nafion membranes. *Solid State Ionics*, 97:333–337, 1997. ISSN 0167-2738. doi: 10.1016/S0167-2738(97)00033-7. URL `http://www.sciencedirect.com/science/article/pii/S0167273897000337`.

[86] John C Slattery. Single-phase flow through porous media. *AIChE Journal*, 15(6):866–872, November 1969. ISSN 1547-5905. doi: 10.1002/aic.690150613. URL `http://dx.doi.org/10.1002/aic.690150613`.

[87] Yoshitsugu Sone, Per Ekdunge, and Daniel Simonsson. Proton Conductivity of Nafion 117 as Measured by a Four Electrode AC Impedance Method. *Journal of The Electrochemical Society*, 143 (4):1254–1259, January 1996. doi: 10.1149/1.1836625. URL `http://jes.ecsdl.org/content/143/4/1254.abstract`.

[88] T E Springer, T A Zawodzinski, and S Gottesfeld. Polymer Electrolyte Fuel Cell Model. *Journal of The Electrochemical Society*, 138:1991, 1991.

[89] Iain Staffell. *Fuel Cells for Domestic Heat and Power: Are they worth it?* Doctor of philosophy, University of Birmingham, 2009.

[90] H Tawfik, Y Hung, and D Mahajan. Metal bipolar plates for PEM fuel cell - A review. *Journal of Power Sources*, 163(2): 755–767, January 2007. ISSN 0378-7753. doi: http://dx.doi.org/10.1016/j.jpowsour.2006.09.088. URL `http://www.sciencedirect.com/science/article/pii/S0378775306020507`.

[91] Tony Thampan, Sanjiv Malhotra, Hao Tang, and Ravindra Datta. Modeling of Conductive Transport in Proton-Exchange Membranes for Fuel Cells. *Journal of The Electrochemical Society*, 147(9):3242, 2000. ISSN 00134651. doi: 10.1149/1.1393890. URL `http://jes.ecsdl.org/cgi/doi/10.1149/1.1393890`.

[92] T Tschinder, T Schaffer, S Fraser, and V Hacker. Electro-osmotic drag of methanol in proton exchange membranes. *Journal of Applied*

*Electrochemistry*, 37(6):711–716, 2007. ISSN 0021-891X. URL `http://dx.doi.org/10.1007/s10800-007-9304-6`.

[93] Peter Van den Bossche, Frédéric Vergels, Joeri Van Mierlo, Julien Matheys, and Wout Van Autenboer. SUBAT: An assessment of sustainable battery technology. *Journal of Power Sources*, 162(2): 913–919, November 2006. ISSN 0378-7753. doi: http://dx.doi.org/ 10.1016/j.jpowsour.2005.07.039. URL `http://www.sciencedirect.com/science/article/pii/S0378775305008761`.

[94] Gonzalo Vazquez, Estrella Alvarez, and Jose M Navaza. Surface Tension of Alcohol Water + Water from 20 to 50 .degree.C. *Journal of Chemical & Engineering Data*, 40(3):611–614, 1995. doi: 10.1021/je00019a016. URL `http://pubs.acs.org/doi/abs/10.1021/je00019a016`.

[95] Rittmar von Helmolt and Ulrich Eberle. Fuel cell vehicles: Status 2007. *Journal of Power Sources*, 165(2):833–843, March 2007. ISSN 0378-7753. doi: http://dx.doi.org/10.1016/j.jpowsour.2006.12.073. URL `http://www.sciencedirect.com/science/article/pii/S0378775307000651`.

[96] C Y Wang and W B Gu. Micro-Macroscopic Coupled Modeling of Batteries and Fuel Cells Part 1 . Model Development. pages 1–25, 1998.

[97] CY Wang and P Cheng. A multiphase mixture model for multiphase, multicomponent transport in capillary porous media - I. Model development. *International journal of heat and mass transfer*, 9310(17): 3607–3618, 1996. URL `http://www.sciencedirect.com/science/article/pii/0017931096000361`.

[98] X L Wang, H M Zhang, J L Zhang, H F Xu, Z Q Tian, J Chen, H X Zhong, Y M Liang, and B L Yi. Micro-porous layer with composite carbon black for PEM fuel cells. *Electrochimica Acta*, 51(23): 4909–4915, June 2006. ISSN 0013-4686. doi: http://dx.doi.org/ 10.1016/j.electacta.2006.01.048. URL `http://www.sciencedirect.com/science/article/pii/S001346860600082X`.

[99] Z H Wang and C Y Wang. Mathematical Modeling of Liquid-Feed Direct Methanol Fuel Cells. *Journal of The Electrochemical Society*, 150(4):A508–A519, 2003. doi: 10.1149/1.1559061. URL `http://link.aip.org/link/?JES/150/A508/1`.

[100] Adam Z. Weber. Improved modeling and understanding of diffusion-media wettability on polymer-electrolyte-fuel-cell performance. *Journal of Power Sources*, 195(16):5292–5304, August 2010. ISSN 03787753. doi: 10.1016/j.jpowsour.2010.03.011. URL `http://linkinghub.elsevier.com/retrieve/pii/S0378775310004003`.

[101] Adam Z Weber and John Newman. Modeling Transport in Polymer-Electrolyte Fuel Cells. *Chemical Reviews*, 104(10):4679–4726, 2004. doi: 10.1021/cr020729l. URL `http://pubs.acs.org/doi/abs/10.1021/cr020729l`.

[102] Adam Z Weber and John Newman. Effects of Microporous Layers in Polymer Electrolyte Fuel Cells. *Journal of The Electrochemical Society*, 152(4):A677–A688, January 2005. doi: 10.1149/1.1861194. URL `http://jes.ecsdl.org/content/152/4/A677.abstract`.

[103] Adam Z Weber, Robert M Darling, and John Newman. Modeling Two-Phase Behavior in PEFCs. *Journal of The Electrochemical Society*, 151(10):A1715–A1727, 2004. doi: 10.1149/1.1792891. URL `http://link.aip.org/link/?JES/151/A1715/1`.

[104] Stephen. Whitaker. ADVANCES IN THEORY OF FLUID MOTION IN POROUS MEDIA. *Industrial & Engineering Chemistry*, 61(12):14–28, December 1969. ISSN 0019-7866. doi: 10.1021/ie50720a004. URL `http://dx.doi.org/10.1021/ie50720a004`.

[105] C. Xu, T.S. Zhao, and W.W. Yang. Modeling of water transport through the membrane electrode assembly for direct methanol fuel cells. *Journal of Power Sources*, 178(1):291–308, March 2008. ISSN 03787753. doi: 10.1016/j.jpowsour.2007.11.098. URL `http://linkinghub.elsevier.com/retrieve/pii/S0378775307026432`.

[106] H. Yang and T.S. Zhao. Effect of anode flow field design on the performance of liquid feed direct methanol fuel cells. *Electrochimica Acta*, 50(16-17):3243–3252, May 2005. ISSN 00134686. doi: 10.1016/j.electacta.2004.11.060. URL `http://linkinghub.elsevier.com/retrieve/pii/S0013468604011910`.

[107] H. Yang, T.S. Zhao, and P. Cheng. Gas-liquid two-phase flow patterns in a miniature square channel with a gas permeable sidewall. *International Journal of Heat and Mass Transfer*, 47(26):5725–5739, December 2004. ISSN 00179310. doi: 10.1016/j.ijheatmasstransfer.

2004.07.025. URL `http://linkinghub.elsevier.com/retrieve/pii/S0017931004003308`.

[108] W W Yang and T S Zhao. Two-phase, mass-transport model for direct methanol fuel cells with effect of non-equilibrium evaporation and condensation. *Journal of Power Sources*, 174(1):136–147, November 2007. ISSN 0378-7753. URL `http://www.sciencedirect.com/science/article/pii/S0378775307016461`.

[109] W W Yang, T S Zhao, and C Xu. Three-dimensional two-phase mass transport model for direct methanol fuel cells. *Electrochimica Acta*, 53 (2):853–862, 2007. ISSN 0013-4686. doi: 10.1016/j.electacta.2007.07. 070. URL `http://www.sciencedirect.com/science/article/pii/S0013468607009516`.

[110] W W Yang, T S Zhao, R Chen, and C Xu. An approach for determining the liquid water distribution in a liquid-feed direct methanol fuel cell. *Journal of Power Sources*, 190(2):216–222, May 2009. ISSN 0378-7753. URL `http://www.sciencedirect.com/science/article/pii/S0378775309001608`.

[111] Yuming Yang and Yung C Liang. Modelling and analysis of a direct methanol fuel cell with under-rib mass transport and two-phase flow at the anode. *Journal of Power Sources*, 194(2):712–729, 2009. ISSN 0378-7753. doi: 10.1016/j.jpowsour.2009.06.023. URL `http://www.sciencedirect.com/science/article/pii/S0378775309010374`.

[112] Dingding Ye, Xun Zhu, Qiang Liao, Jun Li, and Qian Fu. Two-dimensional two-phase mass transport model for methanol and water crossover in air-breathing direct methanol fuel cells. *Journal of Power Sources*, 192(2):502–514, July 2009. ISSN 03787753. doi: 10. 1016/j.jpowsour.2009.03.008. URL `http://linkinghub.elsevier.com/retrieve/pii/S0378775309004832`.

[113] Thomas A Zawodzinski, Charles Derouin, Susan Radzinski, Ruth J Sherman, Van T Smith, Thomas E Springer, and Shimshon Gottesfeld. Water Uptake by and Transport Through Nation | 117 Membranes. 140(4), 1993.

[114] Thomas A Zawodzinski, Charles Derouin, Susan Radzinski, Ruth J Sherman, Van T Smith, Thomas E Springer, and Shimshon Gottesfeld. Water Uptake by and Transport Through Nation | 117 Membranes. 140(4), 1993.

[115] Thomas A Zawodzinski, John Davey, Judith Valerio, and Shimshon Gottesfeld. The water content dependence of electro-osmotic drag in proton-conducting polymer electrolytes. *Electrochimica Acta*, 40 (3):297–302, 1995. ISSN 0013-4686. doi: 10.1016/0013-4686(94) 00277-8. URL `http://www.sciencedirect.com/science/article/pii/0013468694002778`.

[116] Thomas A Zawodzinski Jr., Thomas E Springer, Francisco Uribe, and Shimshon Gottesfeld. Characterization of polymer electrolytes for fuel cell applications. *Solid State Ionics*, 60(1-3):199–211, 1993. ISSN 0167-2738. URL `http://www.sciencedirect.com/science/article/B6TY4-46RVY5K-134/2/535b2378f052368ee170f1dc7a0a89c7`.

[117] Lifeng Zhang, Hsiaotao T. Bi, David P. Wilkinson, Jürgen Stumper, and Haijiang Wang. Gas-liquid two-phase flow patterns in parallel channels for fuel cells. *Journal of Power Sources*, 183(2):643–650, September 2008. ISSN 03787753. doi: 10.1016/j.jpowsour. 2008.05.080. URL `http://linkinghub.elsevier.com/retrieve/pii/S0378775308011348`.

[118] Qiao Zhao, Paul Majsztrik, and Jay Benziger. Diffusion and Interfacial Transport of Water in Nafion. *The Journal of Physical Chemistry B*, 115(12):2717–2727, 2011. doi: 10.1021/jp1112125. URL `http://pubs.acs.org/doi/abs/10.1021/jp1112125`.

[119] Qiao Zhao, Nicole Carro, Ho Youn Ryu, Jay Benziger, and Nicole Caro. Sorption and transport of methanol and ethanol in H+-nafion. *Polymer*, 53(6):–, March 2012. ISSN 0032-3861. doi: 10.1016/j.polymer.2012.01.050. URL `http://www.sciencedirect.com/science/article/pii/S0032386112000778?v=s5http://www.sciencedirect.com/science/article/pii/S0032386112000778`.